MICROPLASMA CHEMICAL REACTION ENHANCEMENT BY LASER MODIFICATION OF DIELECTRIC SURFACE TOPOGRAPHY

BY

CHARLES SHIN

DISSERTATION

Submitted in partial fulfillment of the requirements
for the degree of Doctor of Philosophy in Electrical and Computer Engineering
in the Graduate College of the
University of Illinois at Urbana-Champaign, 2018

Urbana, Illinois

Doctoral Committee:

Professor J. Gary Eden, Chair
Associate Professor Minjoo Lawrence Lee
Professor Xiuling Li
Professor David N. Ruzic

ABSTRACT

A newly developed etching technique, infrared laser ablation, for microplasma device fabrication is introduced. The ablated surface provides a topography that is distinct from the surface created by conventional techniques. Chemical, optical, and electrical experiments have been conducted to observe the difference in performance between devices fabricated with the conventional and with the new technique. Carbon dioxide (CO_2) dissociation and ozone (O_3) generation have been observed to verify the difference. Using the new laser ablation technique, CO_2 dissociation energy efficiency has been increased from 13.5 ± 3.1% to 17.4 ± 5.7%. Furthermore, introducing 10% H_2 (by vol.) into CO_2 with the laser-ablated device has increased the energy efficiency to 23.5 ± 4.6%. In short, total energy efficiency increase of ~75% has been achieved by combining microplasmas with the new ablation technique and the H_2 mixing. Optical emission spectroscopy observation shows that the CO_2^+ Fox-Duffendack-Barker system is dominant at low H_2 flow rates, but the CO Angstrom bands start to dominate as H_2 in the reactant mixture composition is increased. Using the residual gas analyzer (RGA), mass 30 (ethane or formaldehyde) and mass 46 (ethanol or formic acid) have been observed when H_2 is mixed into the CO_2 microplasmas. Calculated from the RGA signal, the maximum amount of ethanol generated is ~0.4 sccm when 100 sccm (80% CO_2 and 20% H_2 by vol.) is flowed into a single microplasma device ("chip"). Using the laser-ablated device, the efficiency of generating O_3 has been increased by 7-11% depending on the flow rate.

Microcavities within the microchannel generated by laser ablation have been observed, and the average cavity diameter has been calculated to be ~33 μm, with cavity density of ~300 mm^{-2}. Intensified charge coupled device (ICCD) images of these cavities indicate that they discharge at lower applied voltage, while the observed optical emission intensity has been measured at ~2 times

higher than typical microplasma regions at any given voltage. Furthermore, the laser-ablated device that contains cavities has higher electrical conductivities. Stark broadening has been measured, and the electron density has been calculated to be $1.2\times10^{16} \pm 0.8\times10^{15}$ cm^{-3} and $1.1\times10^{16} \pm 0.8\times10^{15}$ cm^{-3} for the laser-ablated and powder-ablated chips, respectively. Current-voltage (i.e. I-V) characteristics of laser-ablated chips show ~6% lower breakdown voltage. Also, higher current, compared to that of powder-ablated chips, at any given voltage has been observed for the laser-ablated chips. Owing to the higher surface area of laser-ablated chips, these electrical observations agree with increased field emission effect. As the dimensions of individual cavities will play an important role in further optimizing the plasma-surface interaction, production of uniform cavities has been attempted. Uniform truncated upside-down conical shapes with bottom and top diameters of ~150 μm and ~300 μm, respectively, have been fabricated.

The laser ablation technique also has shown procedural advantages over the conventional technique. From a new microchannel design to a complete microplasma chip, micropowder ablation takes ~150 hours, whereas laser ablation technique requires only ~27 hours. Furthermore, no need for consumable chemicals, such as photoresist or silicone molds, makes the laser ablation technique a safer and more economical option as a surface ablation tool for microplasma production.

To My Family

ACKNOWLEDGMENTS

Over the past six years, my graduate school life has not always been easy. Indeed, I have gone through many personal and academic struggles in this period. Without any doubt, I would not have finished my graduate school without support of people around me. Although I am indebted to many (so many) people in this regard, I would like to specifically address people whose guidance and support were priceless and unconditional.

I would like to express my gratitude to my family. They have always been supportive of my education. Without them, I would not have 'survived' graduate school. The fact that they will always be there for me gives me strength to go through all the hardships in my life. Graduate school life lets me learn how important their support is.

I am extremely grateful for my adviser, Professor J. Gary Eden, and Professor Sung-jin Park for their consistent support. I deeply appreciate their insightful advice and support for my personal and research life. I was taught and trained as an independent researcher, which could not have been achieved without their consistent support and guidance. It is hard to list all the lessons I learned from them (both academic and personal), and I hope they know how grateful I am. It was my honor and privilege to be under their guidance.

I would also like to express my thanks to the LOPE members. As colleagues who were going down the same pathways with me, they made me feel I was not alone. Having so many memories together, I would like to thank them for being the LOPE members. I decided not to list all their names, as they already know who they are.

TABLE OF CONTENTS

CHAPTER 1: INTRODUCTION

As the name implies, *microcavity plasma* devices are those in which low temperature plasma is generated within one or more cavities having at least one spatial dimension less than 1.0 mm. Because all plasmas require a sheath to serve as an interface between the plasma and a material boundary, the electron density must be sufficient to accommodate twice the sheath thickness. Consequently, as the diameter of a cylindrical microcavity is reduced, both the electron density required for the microplasma and the magnitude of the electric field in the sheath rise. Reduced electric field strength (E/N) in the sheath typically reaches values of tens of Td (1Td ≡ 10^{-17} V-cm^2), thus improving a severe constraint on the dielectric surrounding a microplasma. Since the adaptation of microfabrication techniques in the late 1990s, microplasmas have been developed and demonstrated in various material platforms. Their applications include, but are not limited to, optical emitters, photodetectors, and electron and ion sources.[1] Schoenbach and Becker[2] and Eden *et al.*[3] report in depth on various aspects of microplasmas studied over the past two decades. One of the characteristics of microcavity plasma devices is that performance parameters are closely tied to microstructure within the layers as well as at surfaces; i.e. controlling the microstructure is a major factor to take into account when considering the overall performance. In ac microplasma devices, for example, regardless of the device design, the dielectric material plays an important role.[4] In the Laboratory for Optical Physics and Engineering (LOPE), a wet electrochemical anodization process has been intensively studied and developed to produce nanoporous aluminum oxide (Al_2O_3) grown from aluminum (Al).[5,6] As the dc dielectric breakdown strength of a 20 μm thick nanoporous Al_2O_3 film (in air) is ~2,000 V or >60% larger than the corresponding value for

a bulk alumina film of twice the thickness (40 μm),[5] nanoporous Al_2O_3 is a good candidate for a dielectric material.

The extraordinary field strengths present in microplasmas are responsible for electron temperature (T_e) higher than those typical of macroscopic plasmas. Consequently, inelastic collision rates, including those for ionization and molecular dissociation, can be achieved under the assumption that the device is robust enough to endure high electric field and chemical reactions occurring inside the device. This dissertation is concerned primarily with the dissociation of CO_2, one of the most stable molecules because of its linear molecular structure and stability. Furthermore, adding other gas such as hydrogen (H_2) is discussed in an attempt to (1) further enhance the CO_2 dissociation in the plasma, and (2) generate more valuable chemicals such as methane, ethane, and ethanol.

For approximately the past 15 years, a class of microplasma devices has involved the fabrication of microcavities and microchannels by powder ablation of nanoporous alumina layers. This technique has been studied exhaustively and steadily improved. It is now ready for commercialization in the form of manufacturing ozone generators.[7] However, its use of micropowder and lengthy processing time are the bottlenecks of the manufacturing process, especially when mass production and environmental aspects are considered. Compared to the micropowder ablation method, a newly developed laser ablation method can produce similar but distinct structure on, but not limited to, Al/Al_2O_3 plate surface. Also, its maskless ablation with high raster speed and high-power infrared laser eliminate the concerns about micropowder ablation mentioned above.

This dissertation reports and focuses on two aspects: introduction of a newly developed etching technique for microchannel and cavity production called laser ablation technique, and

optimization of microplasma as a chemical reactor. By changing the morphology of microstructures on a robust Al/Al_2O_3 plate, the enhancement of individual microplasma chip performance as a chemical reactor is achieved. In chapter 2, in-depth background on material selection and microstructural control of Al/Al_2O_3 plate surface using laser ablation method is discussed. In chapter 3, the experiments with, and analysis of, microplasma devices are described in detail. In-depth study of control of the calculations of laser ablation is also carried out to verify the capability of the new technique. In chapter 4, the chemical reaction performance as well as various aspects (chemical/optical/electrical) of devices made with the new technique are observed and discussed. In chapter 5, a summary of this dissertation as well as future suggestions are given.

1.1 FUNDAMENTALS OF MICROPLASMAS

Chemical reaction using conventional plasma system is considered to be an expensive method of producing chemicals. First of all, high power is required to sustain the plasma in the reactor, and a large inter-electrode gap to reduce the recombination (reverse reaction or unfavorable reaction) by collision near the wall has to be considered.[8,9] Also, most plasma systems require lower than the atmospheric pressure to achieve lower potential operation, reducing their attractiveness as chemical reactors.

Microplasma is a plasma confined to dimensions of 1 mm or less,[10] and it can solve the shortcomings of conventional plasmas mentioned above. First of all, owing to its small inter-electrode gap that ranges in the vicinity of ~100-500 μm, microplasma can satisfy Paschen's law with higher operating pressure, say atmospheric pressure or super-atmospheric pressure. One of the critical parameters used in the field of plasmas, Paschen curve can be described as

$$V = \frac{B(pd)}{C+\ln(pd)} \tag{1.1}$$

where B is a gas-species-dependent parameter, and

$$C = \ln(A) - \ln\left(\ln\left(\frac{1}{\gamma}+1\right)\right). \tag{1.2}$$

A is also a gas-species-dependent parameter, γ is a Townsend coefficient and its value is usually 0.01-0.1.[11] In short, the breakdown voltage V is a function of p and d, which represent pressure and inter-electrode distance, respectively. Thus, by reducing the distance d, operation pressure exceeding 1 atm is achieved.

Another difference is that the conventional plasma systems have bulk plasma volume that is usually higher than thousands of cm^3, whereas microplasma has volume less than a unity cm^3 to as low as nano- to picoliters. Having significantly smaller volume, microplasma can achieve high surface-area-to-volume ratio (i.e. higher surface-plasma chemistry interaction). The surface of conventional plasma systems is considered as something to be avoided in order to sustain the plasma. In fact, a significant portion of conventional plasma development is in the plasma confinement and sustenance by delicately designing the magnetic field via, for example, tokamak or stellarator.[12] In the case of microplasmas, surface-area-to-volume ratio is significantly higher, and the reaction is dominated by the activity in the sheath region generating higher energy electron population with plasmas at low gas temperatures.[10] Thus, unlike with conventional plasma systems, controlling and utilizing the surface of the microplasma is a key to its optimization as a chemical reactor.

Compared to conventional plasma systems, microplasmas can induce chemical reaction at relatively low power. As an example, a conventional ozone generation system requires input power

of ~kW,[13] whereas a microplasma reactor requires only on the order of tens of watts.[14] When the scalability and the conversion efficiency are taken into account for the industrial application, reducing the power consumption per unit reactor becomes an important factor. In summary, microplasmas have several advantages over conventional plasma systems as chemical reactors.

CHAPTER 2: BACKGROUND

Microplasma technology is capable of generating ozone by using either concentrated O_2 or atmospheric air.[15] Compared to conventional ozone generators, microplasma technology provides a reliable ozone source while minimizing power consumption (~15 W/chip). Owing to its small chip size, it should also be emphasized, microplasma can be made modular, which linearly increases the ozone output. Individual microcavity plasma devices (sometimes referred to as 'chips' in this dissertation) can be easily modified depending on applications. Furthermore, the maintenance is easier compared to that of bulk plasma systems; faulty chips can be easily replaced

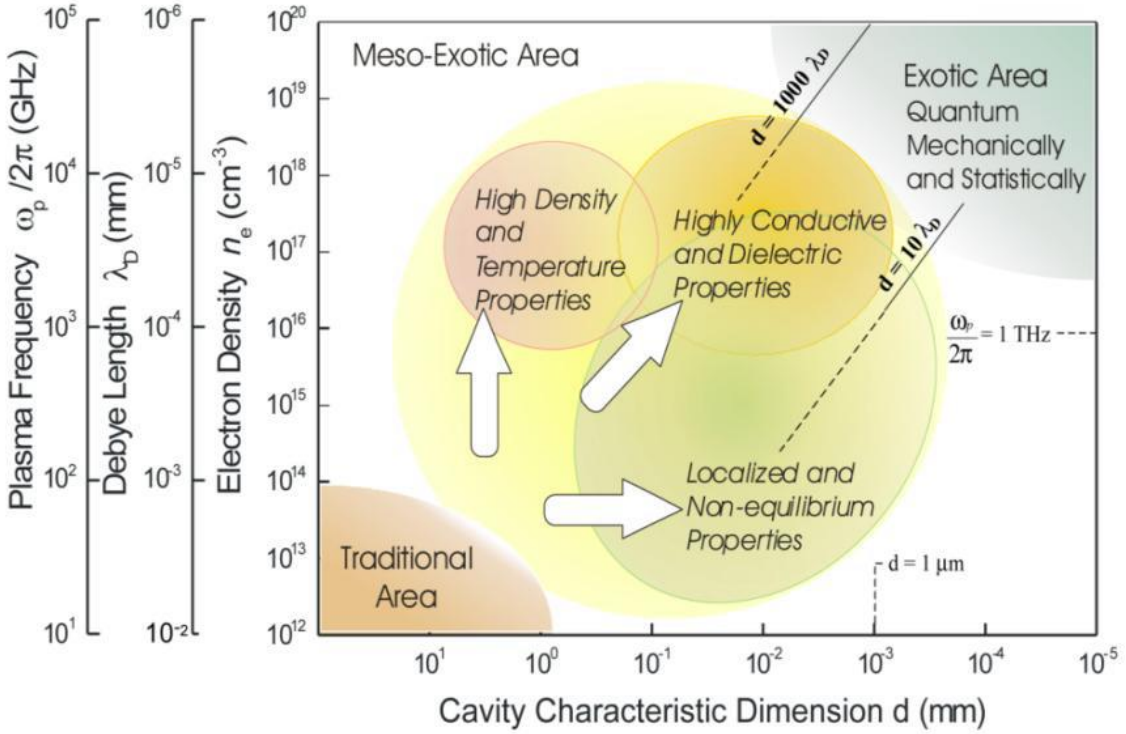

Figure 2.1 Dependence of the plasma frequency, Debye lengths and electron density on the characteristic dimension of a microplasma. (Ref. 16, reprinted by permission of Prof. Kunihide Tachibana, Kyoto University.)

individually, whereas conventional plasma systems usually replace the whole system when the device performance becomes worse than the requirement. Figure 2.1 is a diagram, borrowed with permission of Prof. K. Tachibana, that summarizes the properties of plasmas depending on varied d.[16]

While they are proven to be efficient chemical reactors, microplasma chips can benefit from increased performance, which leads to reduced production cost. This is a practical concern with regard to mass production and profitability. Furthermore, the size of the module (or chip itself) can be reduced when the reaction performance is enhanced, and it further decreases the size of the overall system. When considering mass production, it is also important to consider the throughput of chip production, i.e., how fast chips can be made with relatively uniform performance.

Conventional microplasma chemical reactors are made with nanoporous alumina (Al_2O_3), the growth conditions of which are exhaustively studied in the LOPE here at the University of Illinois. Microchannels or microcavities are generated on the surface of the Al_2O_3 with the ablation technique called micropowder ablation. Although a very effective tool, micropowder ablation is somewhat limited in production speed for various reasons (preparation steps, chemical processing, and the ablation processing time itself). The laser ablation technique promises to increase the device production and decrease the production cost. It is observed that, by using the laser ablation technique, the reaction performance of microplasma devices is enhanced. In this chapter, plasma properties and material perspectives are discussed in order to better understand what causes the enhancement of chemical reaction. In the next chapter, chemical/optical/electrical/topographical properties of laser-ablated chips are compared to the properties of the devices made with micropowder ablation.

2.1 CHARACTERISTICS OF CONVENTIONAL PLASMACHEMICAL REACTORS

A key element of industrialization in the 19th and early 20th centuries was the development of gas phase chemical reactions. However, most such processes suffer from one or more drawbacks. The steam methane reforming (SMR) process, for example, is a method of producing hydrogen (H_2) and carbon monoxide (CO), and both products (known as syngas) are used to make a variety of hydrocarbon fuel sources. The primary chemical reaction of the SMR can be expressed as

$$CH_4 + H_2O \leftrightarrow CO + 3H_2 \quad (\Delta H_f = 228\ \text{kJ/mol}). \tag{2.1}$$

Like many other chemical processes, SMR requires both high temperature and high pressure of 700-1000 °C and 3-25 bar, respectively.[17] These requirements drive up the cost of the associated process and maintenance. Also, a metal-based catalyst (nickel) is used. Packaging and transportation also significantly affect the cost and safety; in order to be used, these products are compressed in cylinders (highly pressurized to reduce the transportation cost) and moved to sites/plants where the they are used. The cost of compression and transportation is about the same as that of producing H_2 itself.[18] After the products are made, these syngases can be employed in another chemical process such as the Fischer-Tropsch process (FTP). Its reaction mechanism is expressed as

$$(2n+1)\ H_2 + n\ CO \leftrightarrow C_nH_{2n+2} + n\ H_2O, \tag{2.2}$$

where n is typically 10-20. Like most other chemical reactors, the production rate for the FTP is dependent on the reactant ratio. In order to avoid compression and transportation, it is necessary to use direct injection of reactants wherever they are used. Thus, the production of reactants with precise mass flow (at high pressures) is required. However, with current technology, as shown in eqn. (2.1), the production ratio is already set such that it requires an additional step in order to

control the injection ratio to acquire a desired reaction. Current H_2/CO generation processes are not well suited to a point-of-use system. In summary, problems to be solved for the conventional chemical reaction are as follows: (1) high temperature/pressure usage, (2) usage of catalyst, (3) compression and transportation of products, and (4) extra steps necessary for the reactant ratio control.

2.2 ADVANTAGES OF MICROPLASMA ARRAYS

Becker *et al.*[10] report several distinguishing features on microplasmas. Owing to the $p \cdot d$ scaling (where p and d are the gas pressure and the plasma characteristic dimension, respectively), increase in pressure is achieved by reducing the device characteristic dimensions. This is an attractive feature for industry applications, as low-pressure plasma operation requires a more complex system. In the LOPE at the University of Illinois, a successful atmospheric pressure operation of CO_2 microplasma is achieved and confirmed experimentally.[18] Among all other characteristics of microplasmas, their electron densities and energies merit mention. Typical microcavity plasmas have densities of 10^{12}-10^{16} cm^{-3}, even though values above 10^{17} cm^{-3} were achieved on a pulsed system; average electron temperature of 1-5 eV is reported using microplasma systems.[10,19,20] Such density and temperature ranges enable the power loadings of the plasma to be as large as MW/cm^3. These characteristic values, different from those of bulk plasmas, can be explained by atmospheric pressure operation (hence, higher electron density) as well as the surface-area-to-volume ratio of microplasmas. Other than properties highlighted in this dissertation, additional aspects regarding characteristics of microplasmas have been observed and studied in the last two decades.[21-25]

Unlike most existing chemical reactors, which are generally based on thermal equilibrium, microplasma does not use temperature and pressure to control the reaction. Instead, microplasma leverages direct electron impact excitation, ionization, and dissociation to induce chemical reactions. As microplasma is a non-equilibrium plasma, the electron temperature, T_e, is high enough to electrically excite atoms and molecules, whereas the background (device and gas) temperature stays near room temperature. Furthermore, in the author's master's thesis work,[26] CO_2 is successfully dissociated with relatively high efficiency. Figure 2.2 summarizes the CO_2 dissociation rate and energy efficiency as a function of flow rate and discharge power.[26] Comparing the results from other methods, figure 2.3 shows that the CO_2 dissociation energy efficiency (using microplasma) is ~2-5 times higher than that for other systems while keeping the flow rate relatively high. Table 2.1 shows the plasma system conditions that correspond to Figure 2.3.[27] Each device employed in ref. 26 is capable of dissociating ~200 mL/hr of CO_2. For the dissociation rate measurement and energy efficiency calculation, this dissertation uses the same experimental method and theoretical calculation described in ref. 26.

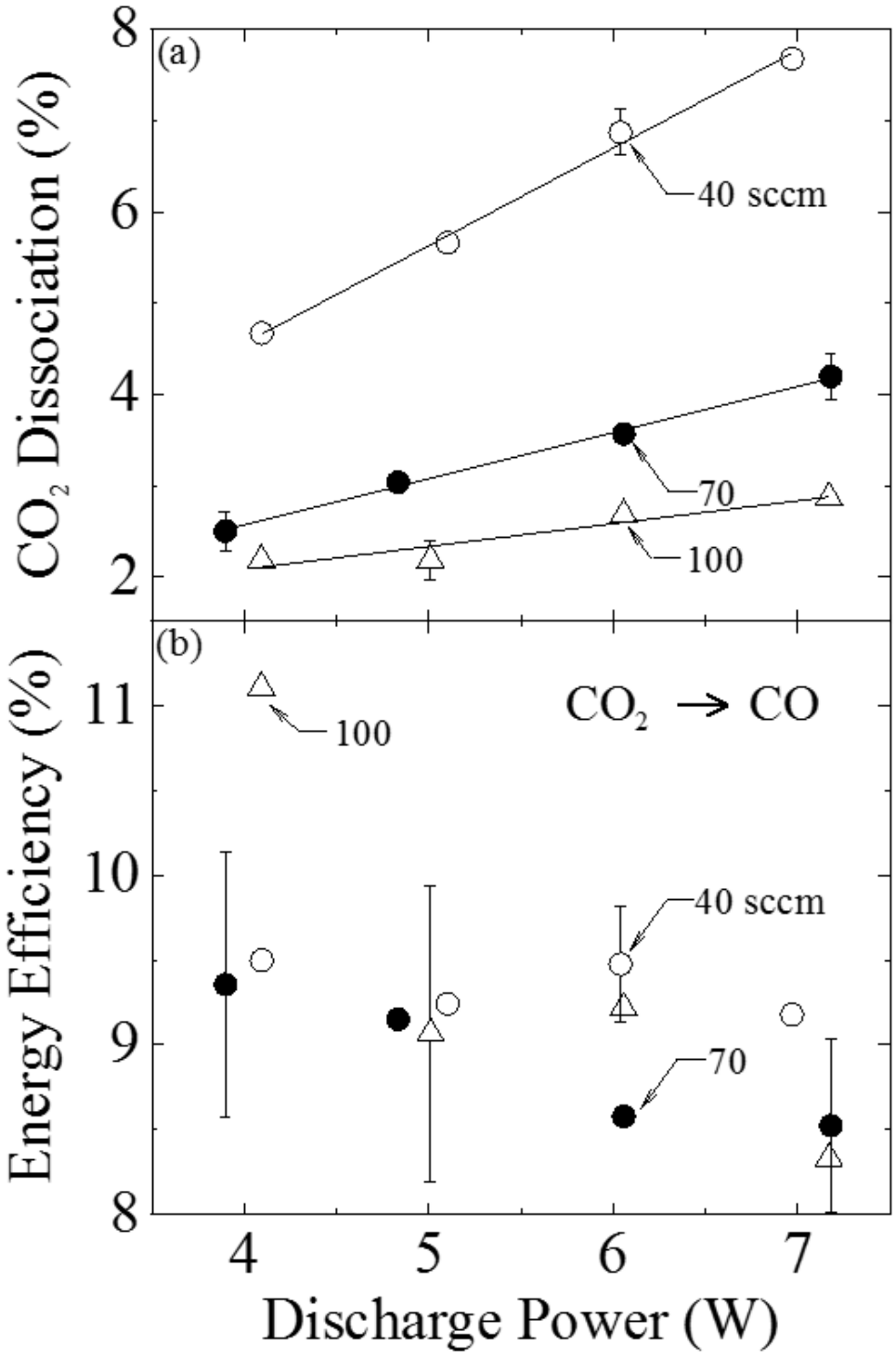

Figure 2.2 Dissociation rate (top) and calculated theoretical energy efficiency (bottom) of CO_2 dissociation using microplasma devices made with micropowder ablation method. 20 kHz sinusoidal waveform was used. Discharge power was calculated by taking the integration of voltage-current data obtained by the oscilloscope. (Reproduced from ref. 26.)

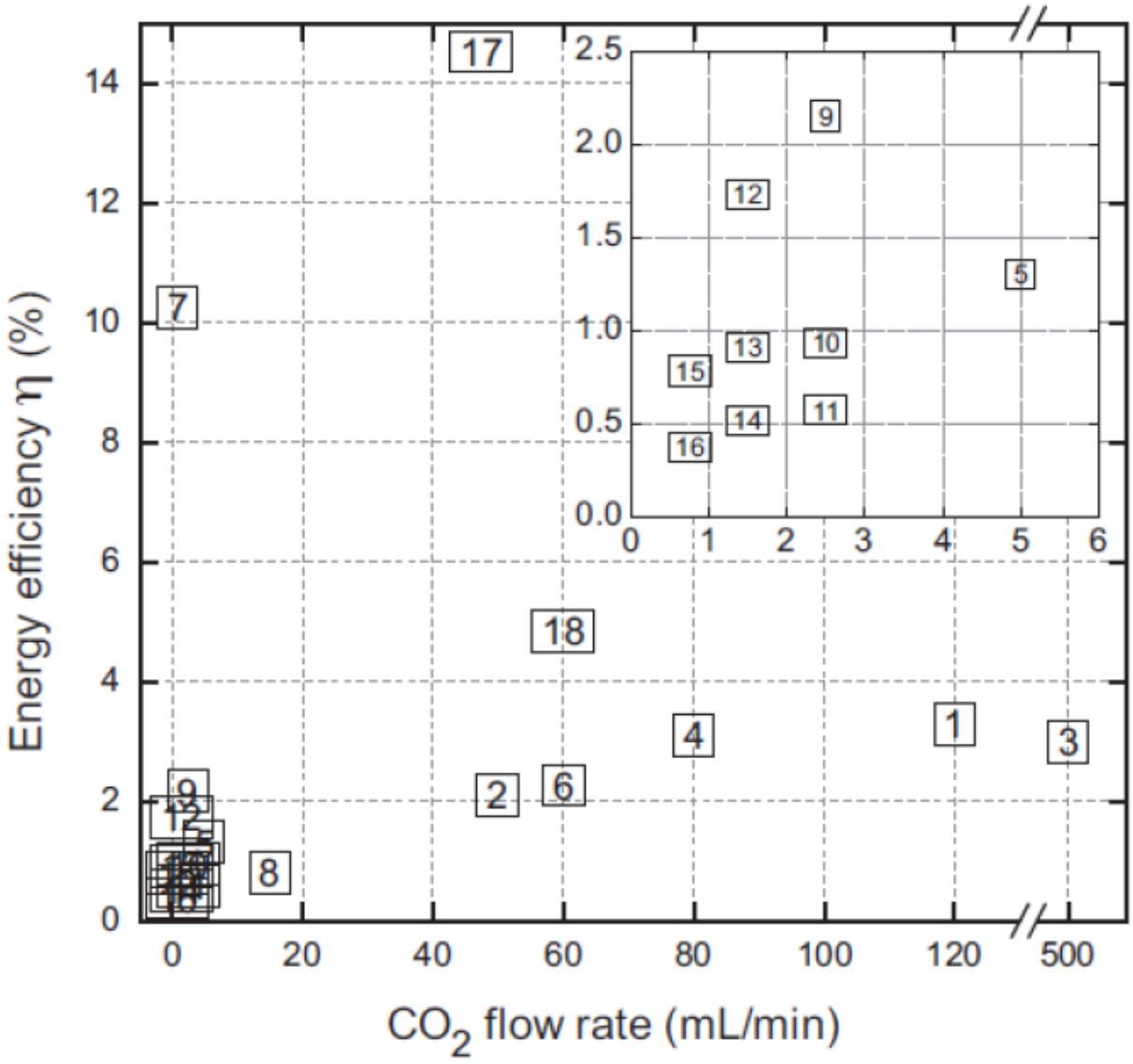

Figure 2.3 Energy efficiency (%) of various atmospheric plasma sources listed in Table 2.1, as a function of the CO_2 flow rates. The area in the left bottom is enlarged as an insert, placed in the right top of the figure. (Reproduced from ref. 27.)

Table 2.1 Plasma system configuration and parameter description for the plasma systems shown in figure 2.3. (Reproduced from ref. 27.)

#	Plasma source		Frequency (kHz)	Power (W)	Carrier or reactive gas	CO_2 flow rate ($mL\,min^{-1}$)
	Type	Geometry				
1	DBD	Tube multi-electrodes	19.5	45	Ar	120
2	DBD	Tube	30	100	/	50
3	DBD	Plane	30	500	CH_4	500
4	DBD	Tube	2.2	45	Ar	80
5	DBD	Plane	25	15	He/CH_4	5
6	DBD	Tube	25	100	CH_4	60
7	DBD	Tube	8.1	0.11	/	0.8
8	DBD	Tube	20	74	CH_4	15
9	AC glow discharge	Tube	8.1	2.78	He	2.5
10			8.1	3.64	Ar	2.5
11			8.1	5.25	N_2	2.5
12			8.1	2.78	He	1.5
13			8.1	3.64	Ar	1.5
14			8.1	5.25	N_2	1.5
15			8.1	3.64	Ar	0.75
16			8.1	5.25	N_2	0.75
17	Pulsed corona	Electrode tip	20–200	9	/	47.5
18	DBD	Tube	30	60	Ar/CH_4	60
19	Gliding arc	"V" shaped electrode	20	225	/	2000

Other than CO_2, ozone (O_3) generation using oxygen (O_2) or ambient air is also of interest. Water treatments including deodorization, decoloration, and disinfection, as well as elongation of food storage lifetime, are the applications of ozone generation systems.[28] EP Purification is a compact ozone generator manufacturing company using microplasma technology. Kim *et al.*[7]report efficient ozone generation (efficiencies surpassing 85 g/kWh) using arrays of low-temperature, linear microplasmas generated within nanoporous Al_2O_3 microchannels.

As mentioned in chapter 1, for the last couple of decades, microchannel generation (etching) within nanoporous Al_2O_3 has been done by the technology called micropowder ablation, also known as powder blasting. Although a very useful technique, micropowder ablation has several drawbacks such as chemical usage, waste disposal, health hazards, and long manufacture time. Laser ablation does not suffer from these drawbacks. Furthermore, within microchannels or cavities, laser ablation creates micro- and nanostructures that are distinct from the topography

created by micropowder ablation. As microplasma benefits, as a chemical reactor, from high surface-area-to-volume ratio, further increasing the surface area via microstructures within microchannels and cavities can benefit the overall reaction.

2.3 LASER ABLATION TECHNIQUE

Microplasma device fabrication using nanoporous alumina has been observed and studied for the last two decades in the LOPE. As a method of etching the alumina surface for microchannel generation, micropowder ablation has been heavily used. The method has been favored for its smooth etched surface as well as its relatively easy-to-use operation process. However, there are several drawbacks of the technique that should be mentioned: cleanroom usage, hazardous micropowder and chemical consumption, and relatively long process time (compared to the laser ablation technique that is introduced in this dissertation). Furthermore, powder blast is an effective tool for etching only brittle materials (such as alumina or glass), not ductile ones. In fact, this limitation is used for making the mask for the etching process; the mask is made with UV curable ink (ductile material), which serves as a surface protecting material for the pattern (similar to photoresist). After the ablation process, the UV curable ink material cannot be completely taken off from the surface no matter how many times the sample is cleaned, so there is always a residue of carbon-based ink on the surface.

Laser ablation does not incur the disadvantages mentioned above. It requires no cleanroom process and thus neither the micropowder nor any cleanroom chemical such as photoresist. Furthermore, it requires no mask, and so leaves no residue on the alumina surface after the process.

Along with the processing advantage, another advantage of laser ablation comes from its distinct topography. Unlike powder blast, which generates a smooth channel topography with surface roughness of ~±5 μm, laser ablation method leaves a surface with roughness of ~±15 μm. The rough surface caused by the pulse laser has many randomly created craters with various diameters ranging 5-150 μm.

2.4 FIELD EMISSION

Field emission is emission of electrons induced by an electrostatic field. Due to an electric field near the surface, a solid surface emits electrons into vacuum and, in this study, into plasma. Figure 2.4 depicts the charged particle fluxes near the surface. The current density created by the field emission, denoted J_{FE}, is also shown in the figure. As the net flux must sum to zero, balancing the charges can be expressed as

$$\Gamma_e^{(-)} = \Gamma_I^{(+)} + \frac{J_{FE}^{(-)}}{q}, \tag{2.3}$$

where Γ_e, Γ_I, and J_{FE} represent electron flux and ion flux from plasma to the surface, and current density from the field emission, respectively. Expanding this equation gives

$$\frac{n_e\{\frac{8\cdot kT_e}{\pi\cdot m_e}\}^{\frac{1}{2}}}{4}\cdot \exp\left(\frac{q\cdot\Phi_s'}{kT_e}\right) = \frac{N_I\{\frac{8\cdot kT_I}{\pi\cdot M_I}\}^{\frac{1}{2}}}{4} + \frac{J_{FE}}{q}, \tag{2.4}$$

where n_e is electron density, T_e is electron temperature, m_e is electron mass, N_I is ion density, M_I is ion mass, and Φ'_s is the sheath potential. Solving this equation in terms of Φ'_s,

$$\Phi_s' = \frac{kT_e}{q} \cdot \ln\{(\frac{T_I \cdot m_e}{T_e \cdot M_I})^{\frac{1}{2}} + \frac{J_{FE}}{q} \frac{4}{n_e\{\frac{8 \cdot kT_e}{\pi \cdot m_e}\}^{\frac{1}{2}}}\}. \quad (2.5)$$

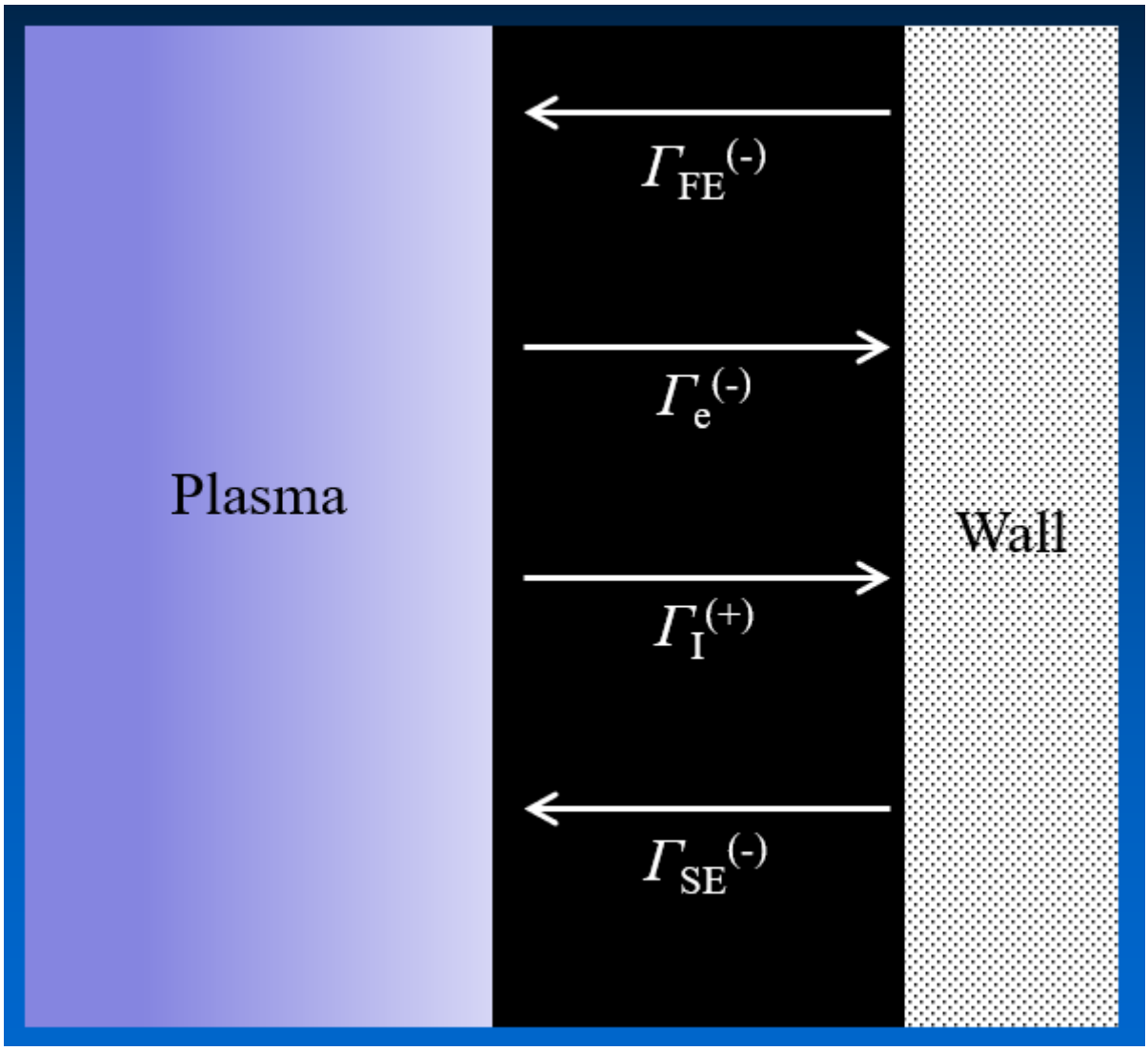

Figure 2.4 Qualitative diagram of a plasma-wall interaction and field emission effect. Black region represents the sheath region, and $\Gamma_I^{(-)}$ represents a current density caused by electron field emission from the surface.

The first terms in the natural log represent the sheath potential when there is no field emission from the surface, and the second term in the natural log (i.e. terms with J_{FE} in it) represents the sheath potential caused by the current density. In short, increasing the field emission effect is beneficial in terms of decreasing the plasma operation potential. Furthermore, considering the fact that microplasma uses electrons to induce the chemical reaction, increased electron population from the field emission is beneficial in terms of inducing higher reaction rates.

As electron field emission is a field-surface interaction, two methods can increase the field emission effect: (1) increased electric field or (2) increased surface area. Using the laser ablation technique, higher surface area (approximately double that of powder ablated) has been achieved. The augmented field emission effect described above can be proven by observing higher charges (i.e., higher current) at the same given voltage. Also, easier discharge condition (i.e., plasma breakdown at lower voltage) should be observed if field emission is augmented.

Current density induced by the field emission can be approximated by using reported parameters of microplasmas (T_e = 2 eV, T_I = 0.1 eV, $M_{I,Ne} = 3.4 \times 10^{-26}$ kg, $m_e = 9.1 \times 10^{-31}$ kg, and $n_e = 10^{16}$ cm^{-3}) and eqn. (2.5). In order to decrease 10% plasma potential, approximately 40 A/cm^2 current density should be induced from the field emission.

CHAPTER 3: EXPERIMENTAL DETAILS

3.1 MATERIAL SELECTION

3.1.1 Nanoporous Alumina (Al_2O_3)

Nanoporous alumina (Al_2O_3) can be grown on aluminum by an inexpensive wet chemical process. The key mechanism of the nanoporous alumina growth has been discovered in detail.[29-32] Compared to bulk alumina, nanoporous alumina is known to have higher dielectric strength; 20 µm nanoporous alumina is measured to have a breakdown voltage of 2000 V, which is more than 60% higher than 40 µm bulk alumina.[5] Also, the dielectric constant is reported to be 19.76, which is about twice that of bulk alumina.[33] This is an attractive feature, as it makes the device electrically more robust without increasing the inter-electrode distance. Furthermore, direct growth on top of aluminum makes no gap between aluminum (electrode) and alumina (dielectric), and it does not require any bonding which can cause detrimental (device killing) aspects such as different thermal expansion coefficient or natural gap. Figure 3.1 shows the scanning electron microscope image of a self-assembled nanoporous structure grown on top of a pure aluminum plate.[34]

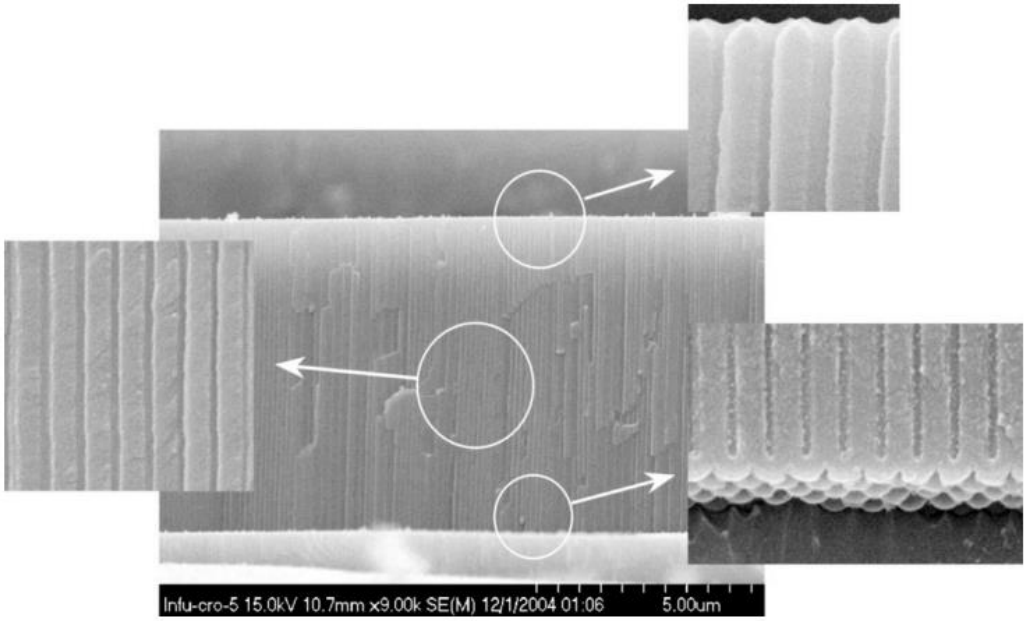

Figure 3.1 Scanning electron micrograph (SEM) of a 6.7 μm thick Al_2O_3 film/Al interface in cross section, in which several regions are magnified to illustrate details of film structure. (Reproduced from ref. 34)

In short, owing to its superior chemical, electrical, and thermal properties as well as its single-material body, nanoporous Al_2O_3 is reported to be one of the superior candidates for a microplasma device with chemical reaction near the wall with various gases and vapors (even with aggressive and attaching gases).[34] Kim *et al.*[14] report the superiority of the nanoporous alumina compared to the devices made of glass materials, and figure 3.2 shows the voltage-current (V-I) characteristics as well as the ozone production rate using several different combinations of materials.

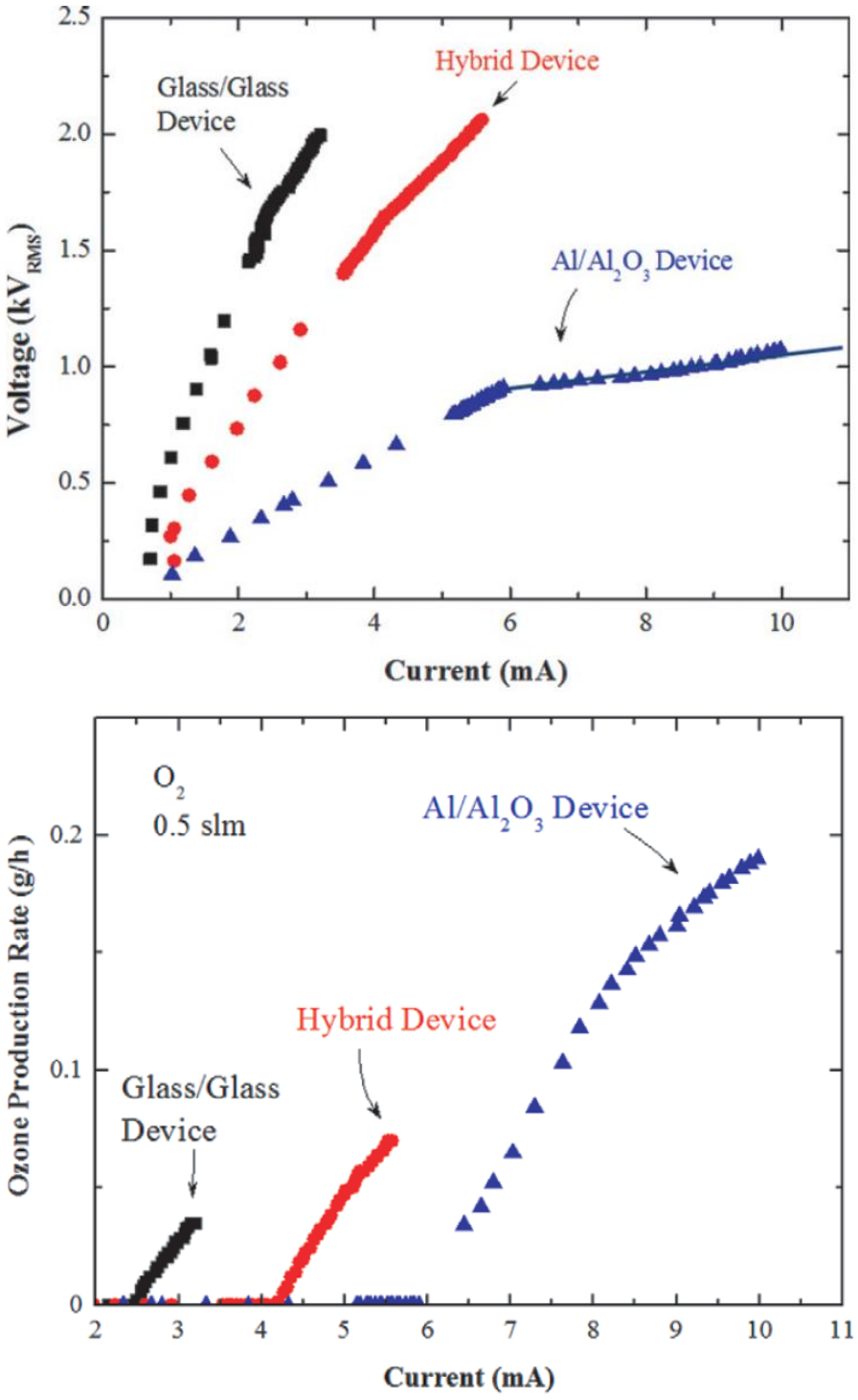

Figure 3.2 (Top)Voltage-current (V-I) characteristics for the three classes of microchannel designs. All data were obtained for an O_2 flow rate of 0.5 slm and the measurements represent RMS values. The solid line associated with the fully Al/alumina structure corresponds to a plasma impedance of ~ 41 kΩ. (Bottom) Dependence of ozone production rate on the current delivered to a 12 channel array. Data are given for glass/glass, glass/alumina, and aluminum/alumina, and the O_2 flow rate for all measurements was 0.5 slm. (Reproduced from ref. 14.)

3.1.2 Carbon Dioxide (CO_2) Dissociation

Carbon dioxide (CO_2) is known as a greenhouse gas. A predicted calculation of CO_2 produced by using fossil fuels with existing infrastructure from 2010 to 2060 is estimated to be ~496 gigatons, and figure 3.3 visualizes regional CO_2 emissions from existing energy and transportation infrastructure.[35] As CO_2 is composed of carbon and oxygen, exhaustive efforts have been made to convert it into fuel or value-added chemicals.[36,37] Thus, effective dissociation of CO_2 serves two purposes: (1) reduction of CO_2 concentration in the atmosphere, and (2) production of more value-added chemicals. Many efforts has been made to electrochemically dissociate CO_2 using various metal catalysts. For example, copper,[38] gold,[39] platinum,[40] silver,[41,42] and composite metals[43] have been studied to reduce CO_2. However, the rising cost of metal catalysts hinders the affordability of catalytic electrochemical methods for the long-term and large volume reduction of CO_2. CO_2 reduction in liquid media also has been studied.[44-46] However, problems such as stability, poor product separation and recovery of the catalyst hinder the use of these methods in the large volume process of CO_2 reduction.[47] Although more recent study using carbon nanofibers (CNFs) can increase the reduction rate by about an order of magnitude compared to the bulk metal systems, the challenge of preparing CNFs, which involves electrospinning temperature of 1,050 ℃ in Ar environment,[48] remains to be solved for this system to be widely used.

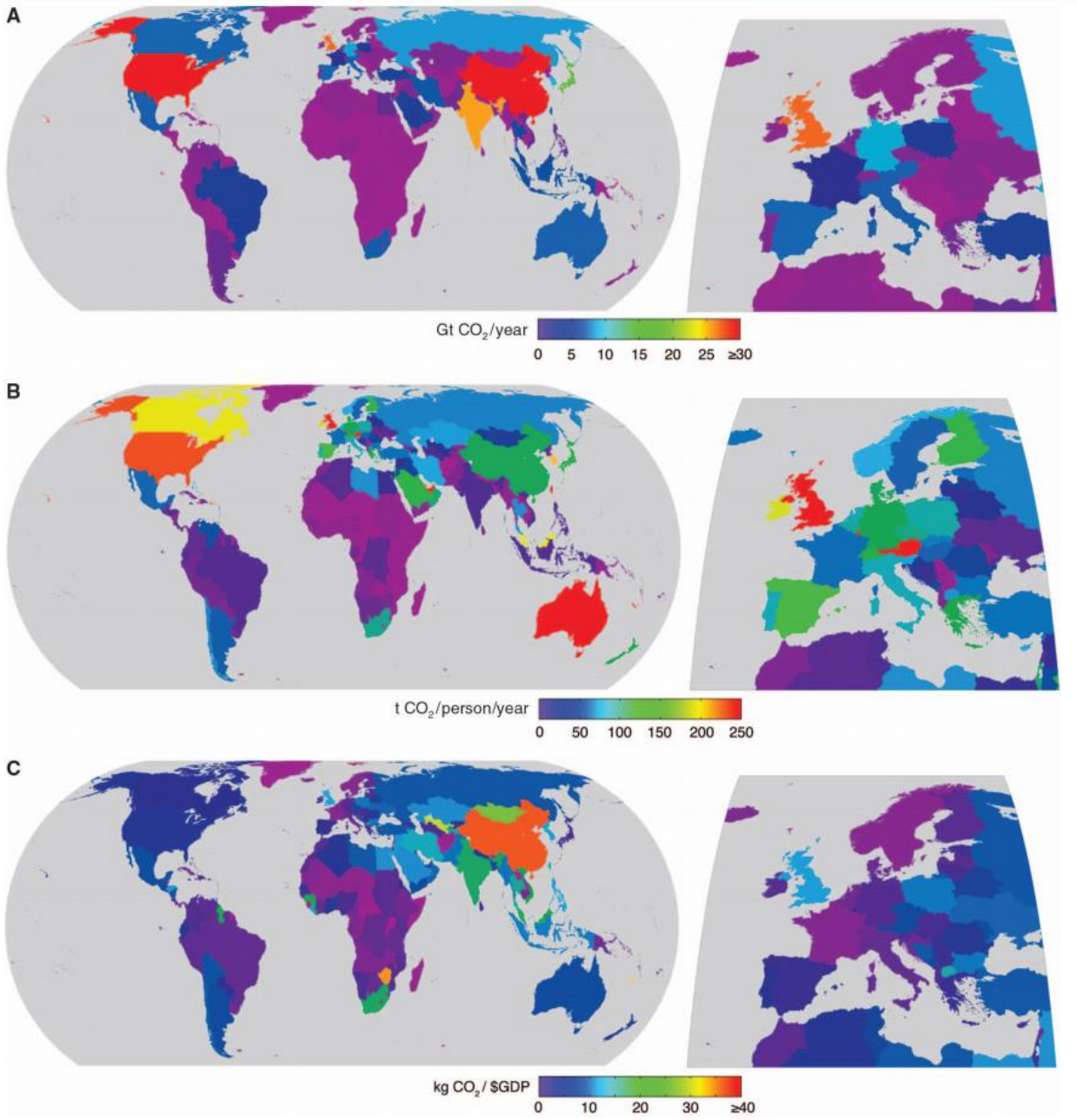

Figure 3.3 Regional CO_2 emissions commitment from existing energy and transportation infrastructure (A), normalized by regional population (B), and normalized by regional GDP (C). (Reproduced from ref. 35.)

Similar to electrochemical methods, plasma systems are also thoroughly studied to enhance the CO_2 reduction (refer to figure 2.3 and table 2.1). Owing to its stability and non-thermal properties, non-thermal plasmas such as dielectric barrier discharge (DBD) have been more

favored when considering a chemical reaction. Various power loadings, carrier gases, device geometry (tubular or planar), and flow rates have been studied in the past.[27,49-56] Some other systems using other plasma types such as pulsed corona or gliding arc have also been studied.[57,58] As shown in figure 2.3, most systems cannot achieve more than 4%, and many systems cannot reach higher than 20 sccm. Either or both of these factors limit the effectiveness of these systems in industry because they cannot meet the high volume (high throughput) and energy efficiency requirements. For the pulsed corona system that reports the highest energy efficiency of >14%, its device lifetime due to its plasma type makes it unattractive to the industry.

In addition its industrial values, observing CO_2 microplasma and its dissociation has great academic value. Putting high electric field in such a small distance between the electrodes induces high reduced electric field (E/N >100 Td) inside the microplasma reactor. In this dissertation, dissociation of CO_2 using microplasma is evaluated and compared to other plasma types and systems. Simulation and study of CO_2 cross-sections and reaction rates show different chemical reaction pathways than when the system is exposed to lower reduced electric fields.[59,60] In other words, electronic excitation, ionization, and dissociation start to dominate. When E/N is lower than 100 Td (the case for most other atmospheric pressure plasma systems), most of the energy is consumed by vibrational excitation. Figure 3.4 shows the different simulated energy allocations as E/N increases.[59] As shown in the figure, it is of great interest to see the reaction change as E/N changes. Owing to its robust and precise manufacturing process, the microplasma device described in this dissertation can take reduced electric field that goes beyond 100 Td, which makes it possible to observe the plasma reaction regime at higher E/N. Thus, it should be intuitively understood that, if high electric field can be achieved as mentioned above, ionized states (CO_2^+) and dissociated

molecules (CO) should be observed in the system, and it can be measured, to a certain extent, chemically (residual gas analyzer) and optically (optical emission spectroscopy).

One more important aspect to recognize is that, as shown by the "dissociation" line in figure 3.4, there is a limitation of dissociation rate by using the electron impact mechanism; in other words, to further increase the dissociation of CO_2, it is inevitable to utilize the ionized or excited states, which are shown as "ionization" and "electronic excitation" in the diagram, respectively. This is where H_2 mixing can be beneficial for the CO_2 dissociation. As will be discussed in chapter 4, H_2 and its products react with the products of discharged CO_2 and cause population reduction on the product side. Also, when higher populations of electron and ionized CO_2 are available, the dissociative recombination ($e^- + CO_2^+ \rightarrow CO + O$) becomes more significant than other reactions, as its rate coefficient is significantly higher than those of other recombination and electron attachment reactions.[59] As a result, higher CO_2 dissociation could be achieved by utilizing the excited/ionized/dissociated CO_2 with the products of H_2. Section 3.1.4 and chapter 4 of this dissertation discuss more in this regard.

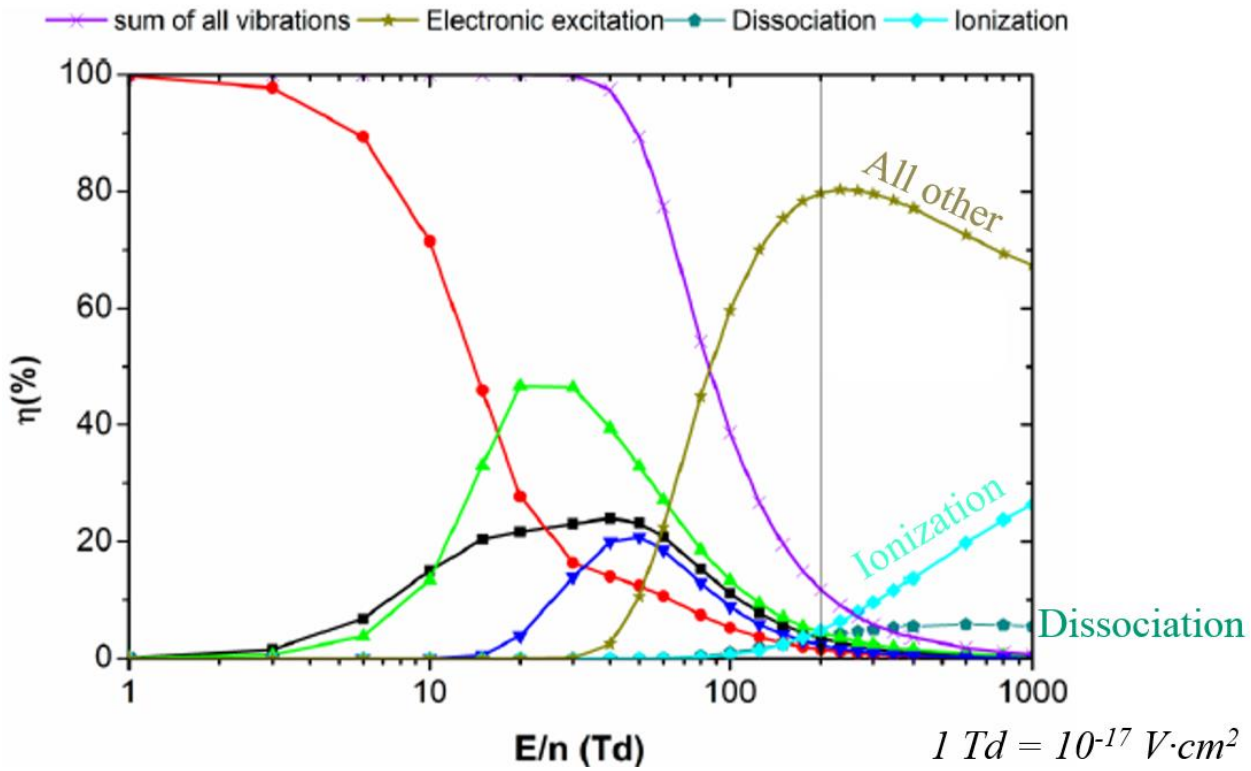

Figure 3.4 Fractions of electron energy transferred to different channels of excitation as well as ionization and dissociation of CO_2, as a function of the reduced electric field (E/n), as calculated from the corresponding cross sections of the electron impact reactions. The electron impact dissociation reaction of CO_2 through electron impact excitation, followed by dissociation, is mentioned in the figure as "dissociation". The sum of electron impact and electronic excitation reactions of CO_2 which form excited levels without dissociation are mentioned as "Electronic excitation". As the dissociation of CO_2 by electron impact has a limitation even at 100-1000 Td, it is inevitable to utilize the ionized or excited species to further dissociate the CO_2 molecules. (Reproduced from ref. 59.)

3.1.3 Ozone (O_3) Generation

Ozone is well known for its antibacterial and disinfection characteristics. Chlorination has long served to disinfect water, but the amount of chlorine used raises environmental concerns. On the other hand, generation of ozone directly from oxygen or the atmospheric air raises no environmental concerns. Also, ozone's superiority over chlorination is demonstrated by its effective killing of bacteria and critical organisms such as *Cryptosporidium* and *Salmonella typhi*.[61] Conventional ozone generation has used a dielectric barrier discharge (DBD) system[62] or

corona discharges, but the short device lifetime as well as spatial and temporal non-uniformity raise reliability concerns.

Unlike the conventional DBD system, microplasma demonstrates reliability as a constant and uniform ozone generation method.[7] Furthermore, modular operation of the microplasma device shows semi-linear increase in ozone generation, showing the capability to control the amount of ozone generated for various applications. It should also be noted that the small device and system size of microplasma is an attractive feature for on-site (*in-situ*) application, as the half-life of ozone in water at room temperature is only in the vicinity of ~10s of minutes.

EP Purification in Champaign, Illinois, uses microplasma technology to produce a commercially available ozone generator. Although the details of characteristic dimensions cannot be discussed in this dissertation, it was possible to compare the performance of laser-ablated and powder-ablated devices in the facility. With all other parameters identical, experiments conducted at EP Purification made it possible to compare 'apples-to-apples' of the performance difference between devices made with different techniques. Experimental configurations and results are discussed in the following sections of this dissertation.

3.1.4 Carbon Dioxide (CO_2) and Hydrogen (H_2) Mixing

Figure 3.4 shows that, even if higher reduced electric field of ~100-1000 Td could be achieved, there is a limit on the CO_2 dissociated by the electron impact. In order to further increase the dissociation rate of CO_2, it is necessary to utilize the ionized species (and excited states induced by direct electron impact). By introducing another gas, such as H_2, excited or ionized CO_2 can be driven to the secondary reactions, rather than going back to CO_2 by relaxation or recombination

reaction. In other words, by constantly removing the product population (e.g. CO_2^+ or CO), higher rate of CO_2 dissociation can be achieved. As of now, the reduced electric field of >100s of Td is achieved, at atmospheric pressure, using microplasmas. Thus, it is necessary, in order to further increase the reaction rate, to find a way to stabilize/reduce the product side of the reaction.

Another reason to introduce H_2 is that the products of H_2 and CO_2 can produce some chemicals that can be used in the industry. Most of the fuel sources and chemicals used in industry are complex hydrocarbons (CHs), and they are mostly coming from refining coarse fossil fuels. The author's master's thesis shows that microplasma devices described in this dissertation are capable of dissociating CO_2 to CO, and an optical emission spectrum in the UV-visible shows traces of CO_2^+, CO, and C_2.[26] With reported electron densities and temperatures of microplasmas, it should be realized that all the radical species and active electrons residing in the microplasma can participate to generate more valuable chemicals such as methanol, ethanol, carboxylic acids, or simple hydrocarbon chains such as methane or ethane. Unlike typical industry-used chemical reactions that involve high pressure and temperature, the chemical reactions in the microplasmas can be induced without increasing the gas temperature and pressure.

3.1.5 Summary

One of the major benefits of increased surface area is higher electron field emission from the surface. Current-voltage (I-V) characteristics comparison of a powder-ablated device to a laser-ablated device shows (1) higher charge density at any given voltage and (2) lower plasma breakdown voltage. If increasing the surface area indeed augments the field emission, both aspects should be observed for the laser-ablated (i.e. higher surface area) device.

Along with modifying the geometry of microchannels, gases can be controlled to modify the products. H_2 is used as a secondary reactant in this dissertation, because of the several benefits of $CO_2 + H_2$ mixture (stated earlier in this chapter). Considering reaction pathways, there are more than 200 reaction pathways for the CO_2 only (and the pathways become more complicated as H_2 is introduced), so it is not practical to track individual reactions. Rather, by macroscopically measuring the products using the RGA, one can approximate which chemicals are produced. However, RGA itself cannot tell the relative population change of ionized states (it cannot distinguish between CO_2 and CO_2^+). Optical emission spectroscopy can be used to observe the ionized CO_2 species in microplasmas. By showing that CO_2^+ excited states diminish (while the overall CO_2 dissociation rate increases), spectroscopy can indicate that CO_2^+ excited states are consumed by making other chemicals (such as hydrocarbons or acid groups) rather than going back to CO_2. Possible products are studied and measured, and the results are compared to that of the simple plasma chemistry simulation done by another group.[63]

3.2 MICROPOWDER ABLATION AND LASER ABLATION TECHNIQUES

Sung *et al.*[64] demonstrate detailed fabrication method, discharge, and the analysis of microplasma fabricated by powder blast method used on glass substrate. Exhaustively developed in the LOPE, powder blast is now a common method of defining and generating microstructures on brittle surfaces, such as Al_2O_3 and glass, for microplasma devices. Laser ablation shows a capability of ablating microchannel/cavity ultimately on any surface. In this section, the two techniques are compared. Only the fabrication method is discussed in this section. The comparison of the device performances is discussed in chapter 4.

Micropowder ablation has been studied and used to create microchannels and cavities. It is an efficient technique for creating arrays of channels or cavities. Owing to its micropowder diameter in the vicinity of 10s of micrometers, it creates regular and smooth ablated surfaces. The ablation process starts by making a master mold using reactive ion etching on a Si wafer. This patterned master mold is then transferred to Al_2O_3 surface by using UV-curable ink and a polymer (stamp), which is made from the master mold. After UV-curable ink is cured under the UV source, the ink now becomes a ductile solid; micropowder ablation is an effective ablation tool for brittle materials, and it does not ablate ductile materials well. Thus, cured ink serves as a protective layer. Al_2O_3 surface is then ablated with the micropowder jet, and dehydrated N_2 gas is used as a carrier. After ablation, the Al_2O_3 plate surface is cleaned with acetone, as UV-curable ink is soluble in it.

Although powder ablation is a very useful and precise technique for generating uniform arrays for microchannels and cavities on Al_2O_3 surface, several drawbacks should be mentioned. First of all, as described above, micropowder ablation requires several pre-ablation processes including (1) lithography for mother mold generation, (2) polymer preparation for the stamp generation, and (3) UV-curable ink process for the mask. These preparation steps require lithography, which can take several days including channel design printing for the photolithography mask generation. Also, in terms of chemical usage, processes involve photoresist, UV-curable ink, and room temperature vulcanization (RTV) material for a stamp. The operation and usage of micropowder can also cause health hazards. Furthermore, the technique involves a direct masking process and, regardless of the cleaning, there is always residual UV-curable ink on the Al_2O_3 surface.

Rapid and direct writing by laser ablation can be a solution to many of the drawbacks of micropowder ablation. First of all, laser ablation requires no mold production process. It involves

no lithography or associated chemicals. Also, the maskless process of laser ablation requires no chemicals or physical adhesion to the Al_2O_3 surface; this eliminates the use of UV-curable ink and the solvents required for stripping the mask. Furthermore, using a laser instead of micropowder makes this technique more operator-friendly, as it does not use any potentially harmful particle such as micropowder. Last but not the least, the process time is only in the vicinity of hours, not days.

In short, compared to micropowder ablation, laser ablation has several advantages: shorter overall process time, no lithography process, maskless process, and no harmful chemicals (photoresist, UV-curable ink, RTV, and micropowder). Figure 3.5 illustrates the process flow chart that compares the two techniques compared in this section.

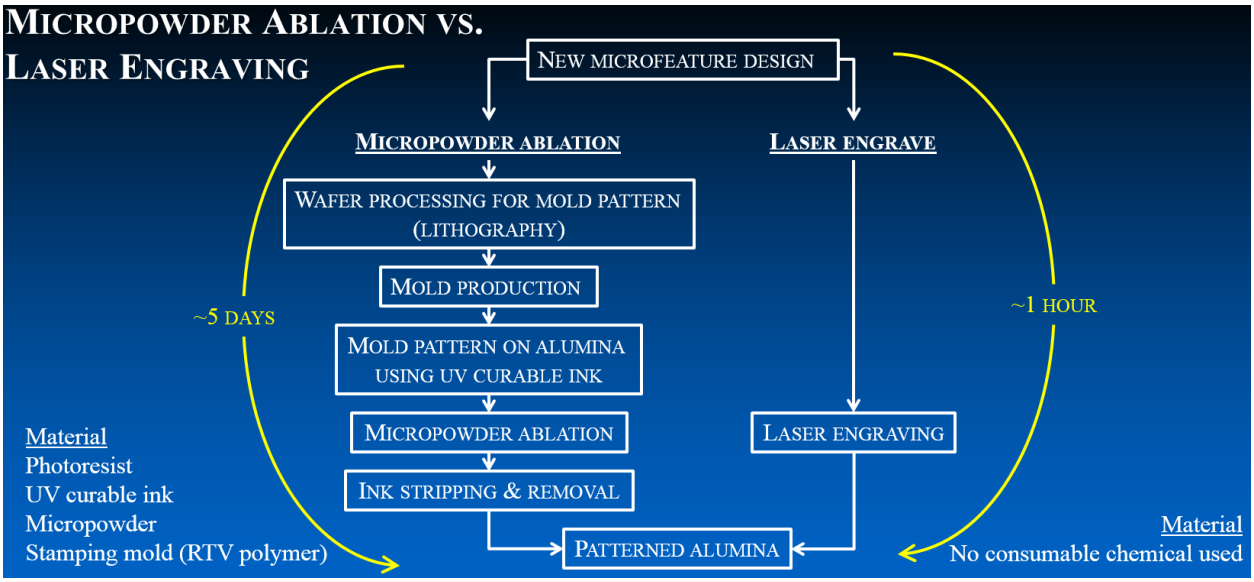

Figure 3.5 Process flow chart graph for two etching methods. Major processes and chemicals used, and approximate time required are depicted in the diagram. Flow on left side shows the processes required for powder ablation, and the right side shows that of laser ablation.

3.3 DEVICE ASSEMBLY

As mentioned above, nanoporous Al_2O_3 is used as a base material. The fabrication of the microplasma device involves two Al embedded Al_2O_3, where Al serve as two electrodes. Al_2O_3 is grown to ~100-200 ± 10 μm for the top Al/Al_2O_3 plate, and 100 μm for the bottom plate. Unless stated otherwise, the Al/Al_2O_3 plates used in this dissertation are 6.8 cm long by 2.9 cm wide for the bottom electrode, and 9 cm long by 2.5 cm wide for the top electrode. Note that the widths of the top and the bottom plates are slightly different in order to minimize any possible electrode-to-electrode short (arc) near the edges. Also, unless stated otherwise, microcavity or channel geometry is ablated/ablated on the bottom plate, i.e. only one side is patterned. Figure 3.6 shows the cross-sectional schematic of a typical device fabrication and operation. Figure 3.6 (a),(b) show the top electrode and bottom electrode, (c) shows the sandwiched structure of top and bottom electrode after the bottom electrode has been ablated/ablated, and (d) shows how the power is applied to the device. For the figure 3.6 (c) and (d), two plates are bonded on the edges with adhesive epoxy, but it is not shown in the figure. Two 0.25 inch outer diameter glass tubes are attached for the gas flow in and out. Furthermore, gas inlet and outlet are shown on the same side (bottom plate) in figure 3.6, but a structure with gas inlet and outlet on each side (one hole/plate) is also fabricated. Average depth of ~60-80 μm is used for chemical reaction testing, unless noted otherwise. The depth and micro-feature control are discussed further in the following section. Top channel width of microchannels ranges 300-1000 μm with 16-25 linear microchannels. Edge-to-edge (the channel spacing) of 500 μm is used. Although the width range stretches up to 1000 μm for observation purposes (i.e. SEM and ICCD observation), the chemical reactor used in this dissertation uses the width of 500 μm.

Optical observation was enabled by replacing the top electrode with indium tin oxide (ITO) coated glass. ITO was patterned to only cover the active area (i.e. microfeature area), then ITO was attached to the wire by silver epoxy. Figure 3.7 shows the top view image of the ITO coated top electrode using 300 Torr Ne. Note that ITO glass shatters if it is too thin. In this dissertation, 500 μm boro-aluminosilicate glass with R_s = 70-100 Ω is used. Compared to a typical thickness of a dielectric of the top Al/Al_2O_3 plate, where the thickness is ~100 μm, this is about 5 times thicker. This decreases the reduced electric field significantly, so it is not suitable for some of the experiments this dissertation pursues. In short, devices made with this method are easy to fabricate and to observe because the whole area of the microchannel/cavity is visible; however, this device was used only for illustration, not for chemical reaction. Figure 3.7 shows microplasma discharge, with uniformly spaced and formed cavities with upside-down truncated cone shape with the bottom diameter of ~150 μm and the top diameter of ~300 μm (using 300 Torr neon).

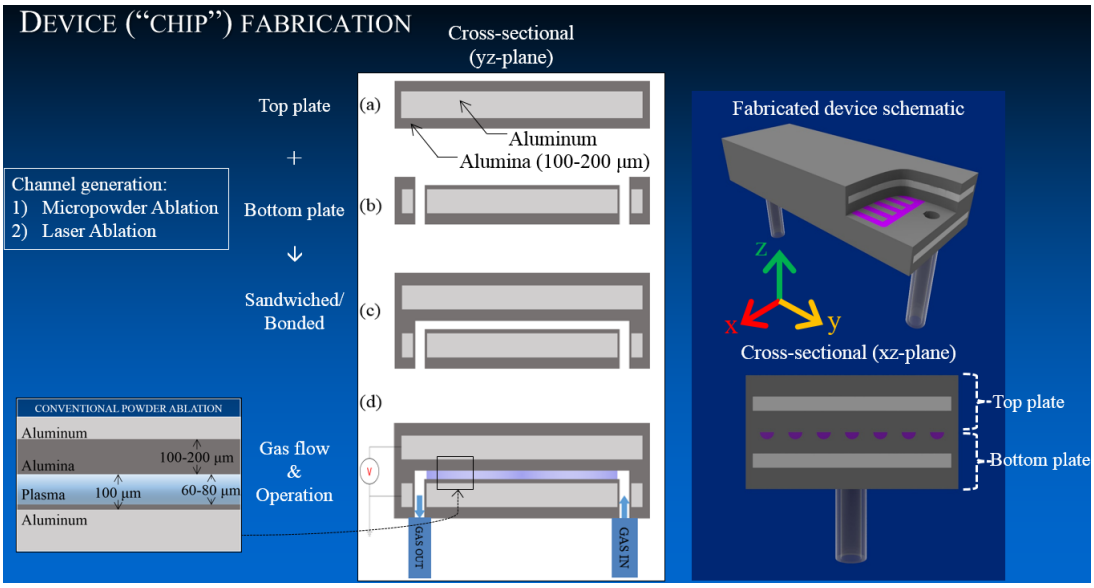

Figure 3.6 Device fabrication illustration using cross-sectional view of materials and processes. (a) represents the top Al/Al_2O_3 plate, (b) represents the bottom Al/Al_2O_3 plate with powder-ablated or laser-ablated surface, (c) represents the bonding of (a) and (b), and (d) is the representation of how the device is connected to the power supply and how the gas is flowed into the system. Images on the right show the qualitative diagram that shows the interior of the discharging device (top) and the cross-sectional view (bottom).

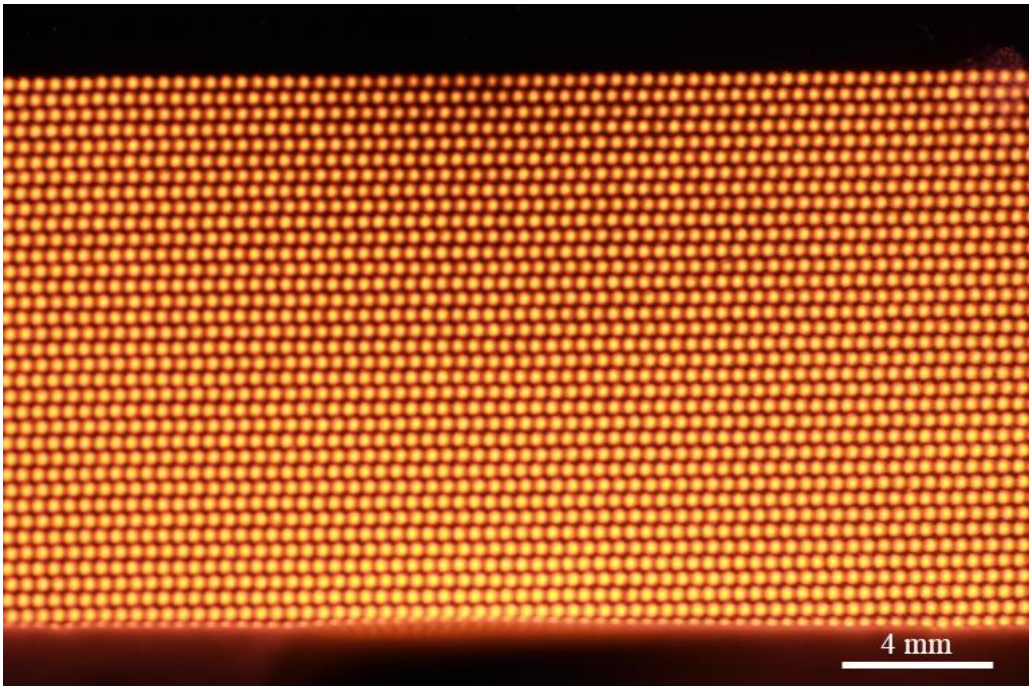

Figure 3.7 Top-view image of microplasma discharge of an optical device made with laser ablation technique. Top side is ITO coated soda lime glass, and the bottom side is nanoporous alumina with cavities generated using the laser ablation technique. Gas pressure of ~300 Torr Ne was used, and ~1.3 kV_{RMS} with 20 kHz sinusoidal driven waveform was used.

In order to observe the benefit of having only a couple of hundreds of μm electrode-to-electrode distance, two Al/Al_2O_3 plates had to be used. This fabrication method is similar to making chemical reaction device (two Al/Al_2O_3) plates, except an emission was observed from the outlet gas glass tube. Thus, it was possible to observe the CO_2 emission coming from the microchannel with the dielectric thickness of ~200 μm.

3.4 EXPERIMENTAL CONFIGURATION

Unless stated otherwise, this dissertation mainly uses pure research grade (99.999%) CO_2 and H_2. For the flowing gas experiment, gas was flowed into the microplasma chip using volumetric flow controller (Aalborg Instruments), and the flow rate ranged 0-100 sccm. The gas leaving the device

was sampled by a leak valve and subsequently analyzed by a residual gas analyzer (RGA, a miniature quadrupole mass spectrometer). The remaining (unsampled) gas was vented out to an exhaust line after passing through a check valve. A 20 kHz sinusoidal driving waveform was applied between the top and bottom electrodes of the microplasma chips, and the current and voltage were measured with a 1 GHz bandwidth oscilloscope (Agilent Technologies). The RGA was maintained at a pressure of ~10^{-9} Torr. For the optical emission measurement, a 0.75 m spectrometer having a CCD array (Princeton Instruments) was used to detect and observe the microplasma emission. The spectrometer resolution is 0.024 nm in first order, and the glass window restricts spectroscopic measurement in the UV to wavelengths above ~330 nm. The discharge power is calculated by integrating the power (V·I) waveform. Figure 3.8 shows a schematic of the experiment as well as the experiment setup. The figure illustrates that the gases flow from the left side, and the measurement (either optical or chemical) was made by sampling from the right side. As the experiment was conducted, the device's electrical characteristics were measured directly by connecting it to the oscilloscope. For the ozone generation experiment, a standardized test conducted at EP Purification is used to compare the performances of the devices made by the conventional and the new ablation methods. More experimental detail is provided in chapter 4.

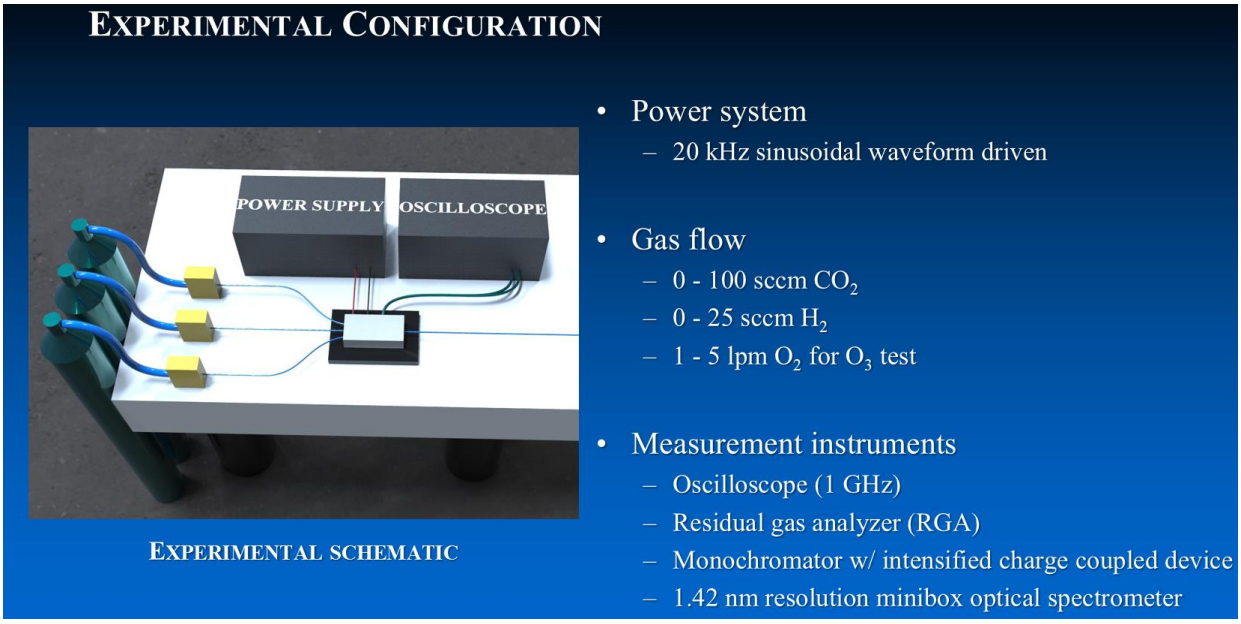

Figure 3.8 Experimental schematic and system parameters.

CHAPTER 4: RESULTS

4.1 MATERIALS ABLATION BY INFRARED LASER

Before discussing the electrical, optical, and chemical performance of the devices made with a newly developed ablation technique, the capability of this new technique should be discussed. The motivation of developing this new technology was to see if it would be more beneficial (in terms of fabrication speed, yield, microplasma performance, etc.) to use the laser ablation method over the conventional technique. The main concern before this technique was developed was whether a sample processed with laser ablation method would discharge or not. In this section, the results on the newly developed laser ablation technique, recipe-wise, are discussed.

First of all, it was determined whether laser ablation can etch the alumina, or any other material, to the depth that the conventional method can etch. Figure 4.1 shows the measured average etched depth of the alumina surface using the laser ablation method. It shows that the etch rate is semi-linear until ~60 J/cm^2, then it starts to plateau after that point. It should be noted that the depth of the alumina used in this experiment was ~200 μm, and the plateau started to happen as the etched depth was getting closer to the aluminum, i.e. the etched depth was starting to plateau when the un-etched alumina was getting thinner and thinner. For example, if ~100 μm alumina was used, the plateau would happen much earlier than the plateau shown in figure 4.1.

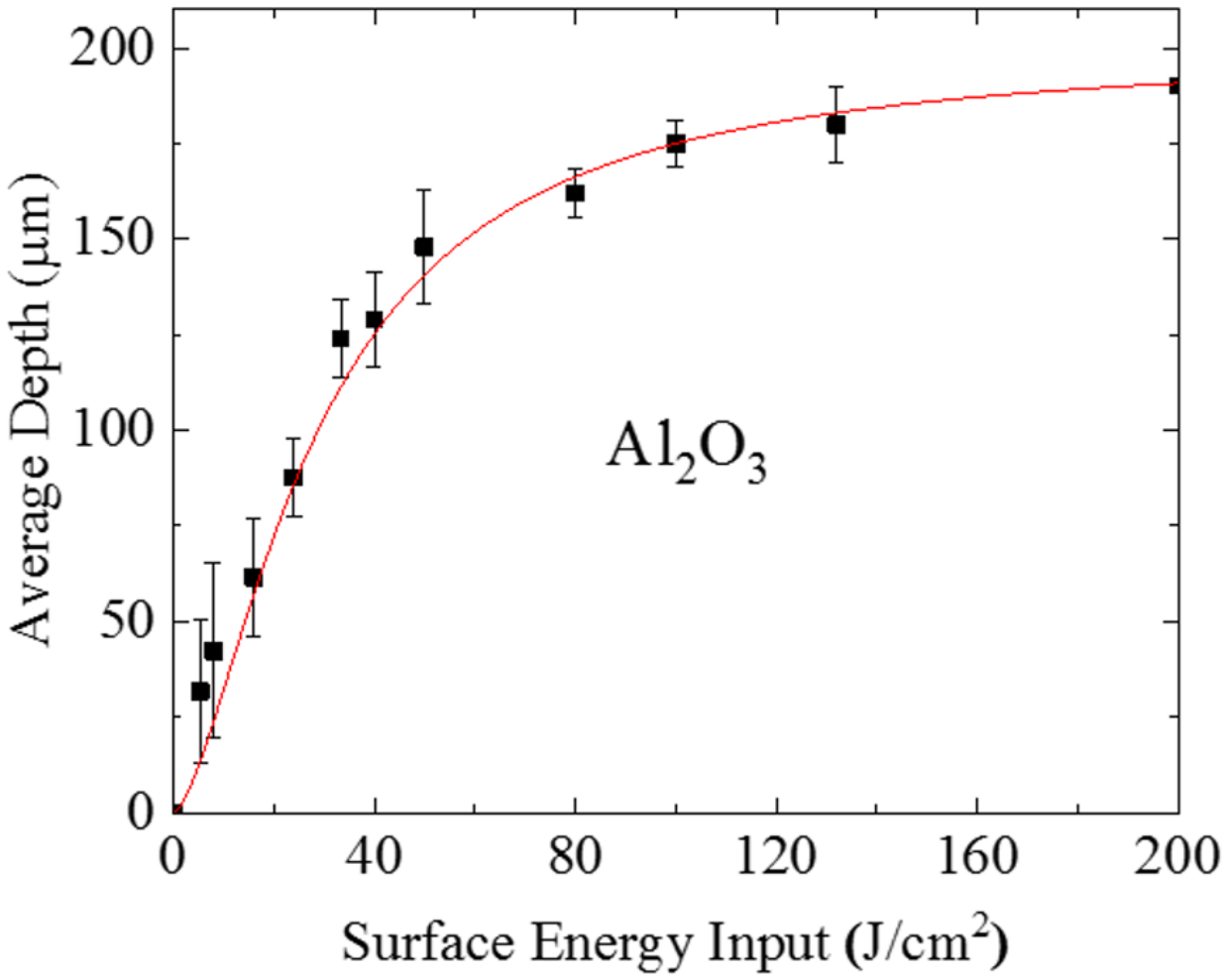

Figure 4.1 Average etched depth using laser ablation technique. 75 W CO_2 laser was used, and the surface energy input was controlled by various parameters such as scanning speed and laser power.

The etch depth of the quartz using the laser engraver was tested as well. Figure 4.2 shows the measured depth of etched quartz. Unlike alumina, quartz does not depict plateau characteristics. Independent of the thickness of the quartz, it always showed linear etch rate; it linearly etched away the quartz until it reached the thickness of the quartz sample, then it punctured the sample. Although figures 4.1 and 4.2 show the experiment result of nanoporous alumina and quartz, several different materials including acrylic, woods, plastic, rubber, and soda lime glass were tested. All

materials were successfully etched except the soda lime glass, as it could not endure the thermal effect of the laser and cracked along the path of the laser.

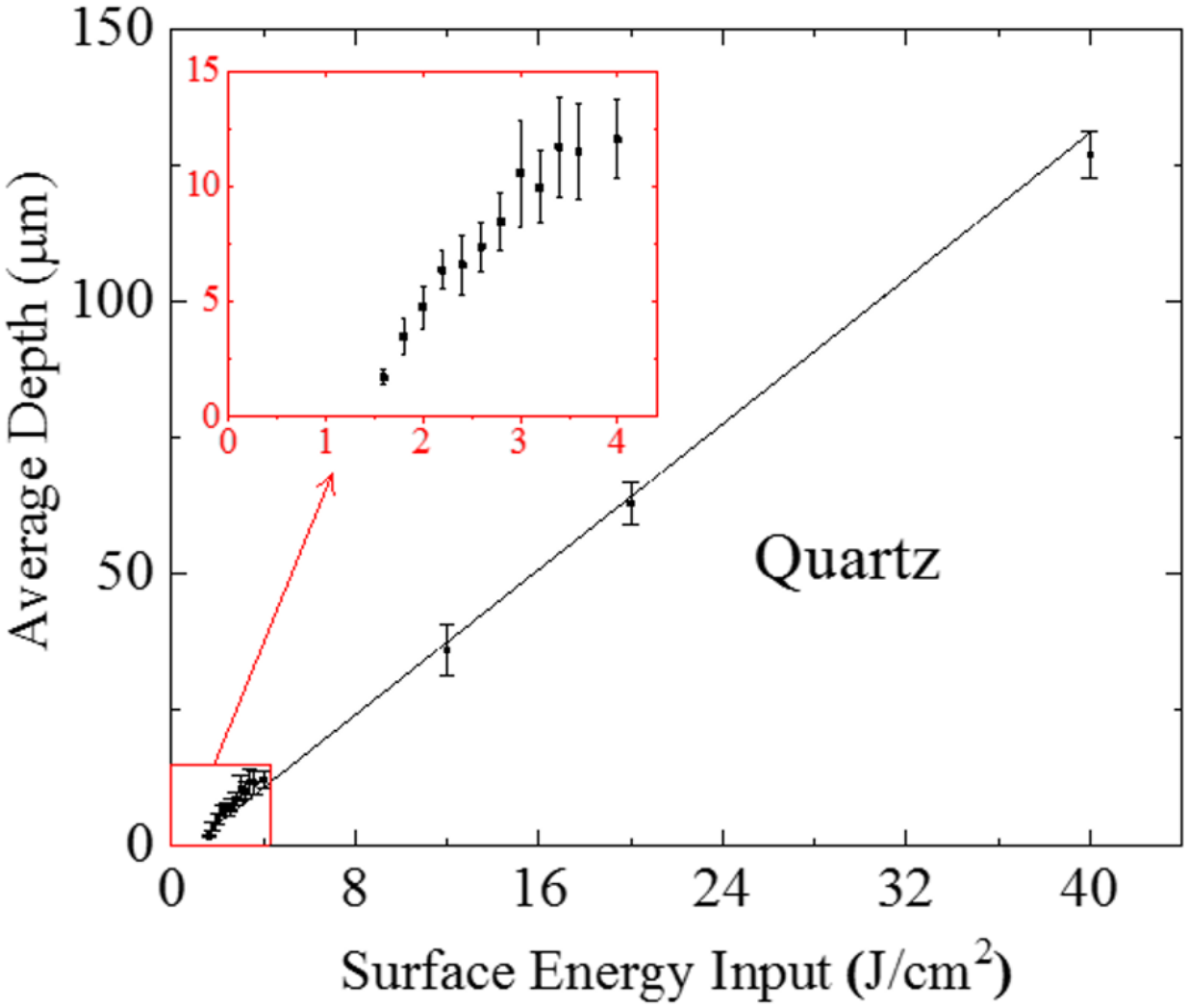

Figure 4.2 Average etched depth of a quartz using laser ablation method. As mentioned for the alumina etching, laser power and scanning speed were controlled to change the surface energy input.

Using the measured average depth depending on the surface energy input, a molecular energy input was calculated. Energy deposition of ~0.91 eV/molecule was obtained using the linear region of figure 4.1. As a 10.6 μm infrared laser (CO_2 laser) was used, photon energy was

0.12 eV/photon, indicating that individual molecules were hit with an average of ~8 photons before being ablated. The ablation rate started to flatten beyond ~60 J/cm^2. One thing to note is that the alumina thickness of ~200 μm was used for the depth measurement. Thus, the saturation can be explained by the fact that aluminum started to be exposed; higher reflective surface of the metal would reflect photons rather than absorbing their energy, making ablation less effective. More in-depth calculation regarding this calculation can be found in the Appendix.

Figure 4.3 shows the scanning electron microscope (SEM) images of powder-ablated alumina. The measured surface roughness of the powder-ablated surface was ~±5 μm. Figure 4.4 shows the SEM images of laser-ablated alumina surface. The surface roughness of the laser-ablated surface was ~±15 μm. Note that on the morphology of the laser-ablated surface there are cavities created, with random diameters, within the channels. The significance of these cavities is discussed later in this section.

As was shown in figure 3.5, the fabrication process complexity should also be considered. After a certain channel geometry is designed, laser ablation can complete a sample production with maximum time consumption of ~1 hour. However, the conventional technique can take up to ~5 days; this long time is mostly wasted by waiting for the mask print, cleanroom process and ink applications. Furthermore, the powder ablation method requires chemicals (photoresists, UV curable ink, micropowders, and the polymer material for the mold), whereas the laser ablation technique requires no hazardous chemicals. It should also be mentioned that laser ablation is a maskless process, whereas the powder ablation method requires blue ink directly applied on top of the sample and leaves residue, which is a carbon-based ink that may be detrimental for some applications; it can be a source of carbon as it can react with the plasma. In short, the newly developed laser ablation technique is advantageous in terms of creating microchannel/cavities.

Regarding production efficiency, reduced production time as well as less chemical usage make laser ablation more attractive than conventional ablation.

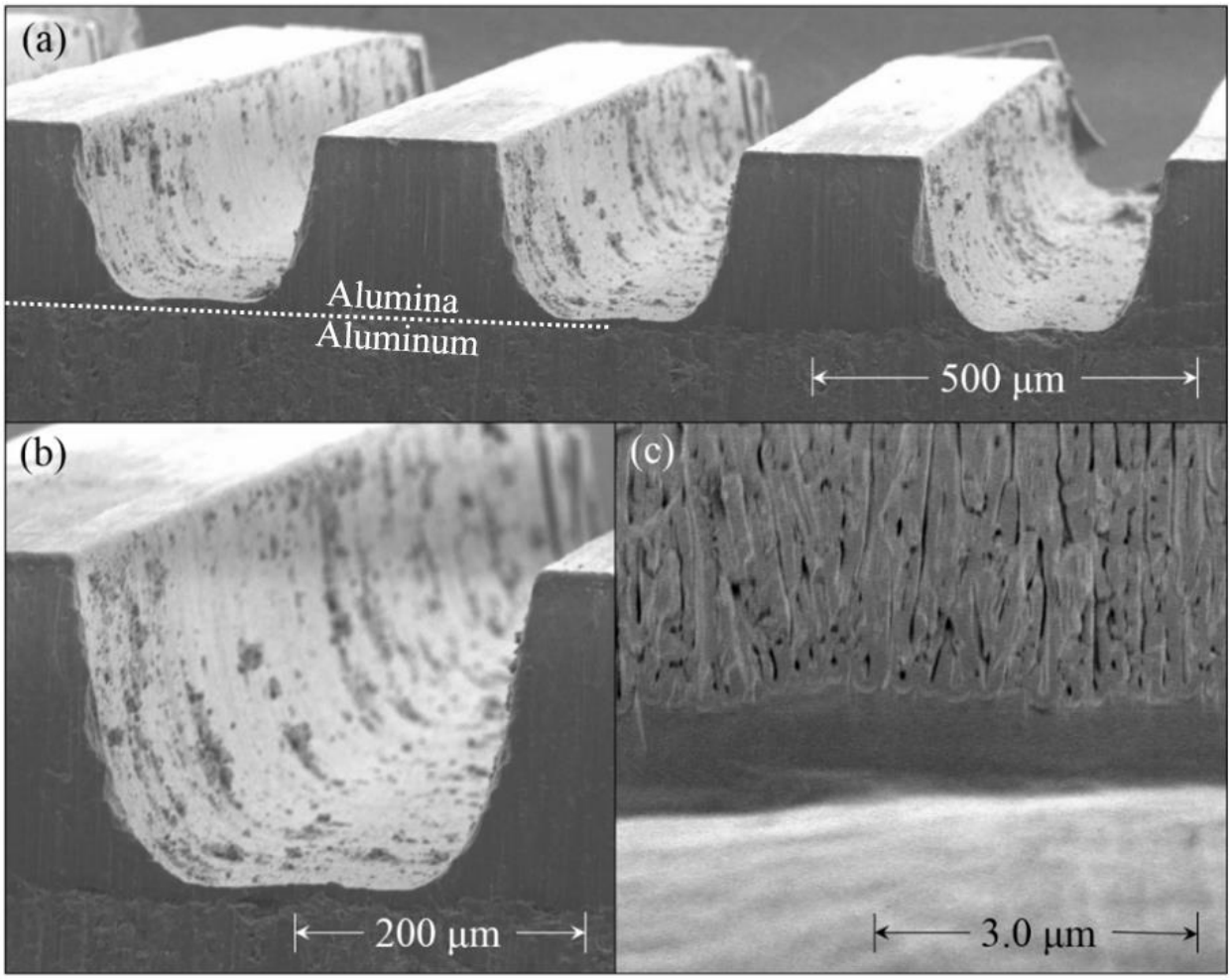

Figure 4.3 Scanning electron microscope (SEM) image of powder-ablated nanoporous alumina. (a) shows 3 microchannels from slanted angle, and (b) shows the surface of a single channel. (c) shows aluminum and alumina boundary. Unlike powder-ablated alumina surface, laser-ablated microchannels have ~300 (per mm^2) small cavities within them. (Reproduced from ref. 65.)

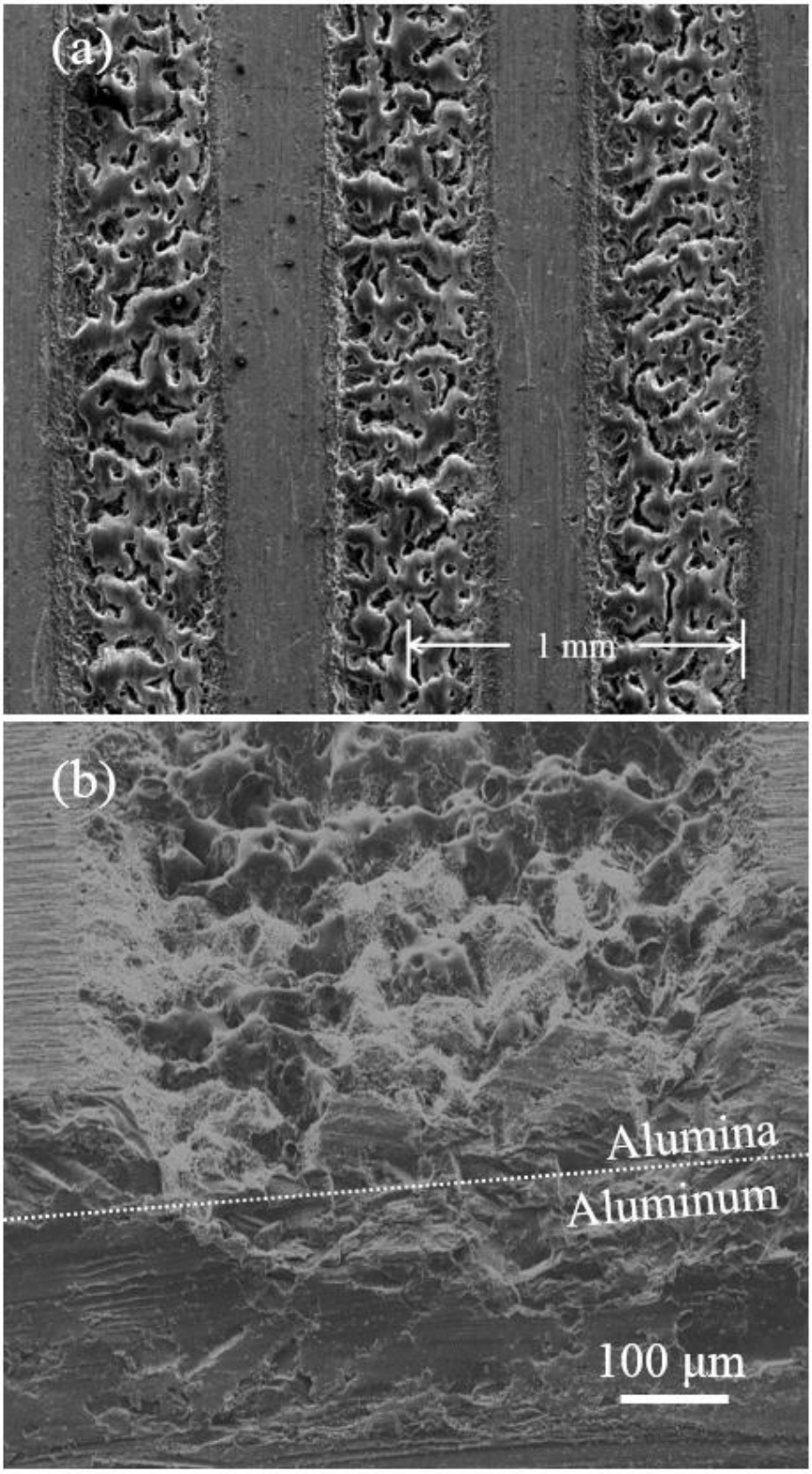

Figure 4.4 SEM image of laser-ablated nanoporous alumina surface. Top-view image of 3 microchannels with the width of ~500 μm (a), and a cross-sectional slanted view image of a single channel (b) are shown.

Figure 4.5 shows the microstylus surface profilometry obtained by sweeping across one microchannel made by the laser ablation technique. The figure shows the surface roughness of ~36 μm, which is very similar to the result obtained by the optical microscope (±15 μm). Figure 4.6 (a) shows the profilometry data of a single microchannel using one sweep of 20 J/cm^2 laser engraver output, and (b) shows the result from the same recipe but swept twice. As shown in the figure, the surface gets smoothed out as the laser ablation exposes the aluminum. Thus, in order to maximize the field emission effect, it is necessary to fine-tune the parameters of the laser ablation technique to get the maximum number of cavities with desired cavity diameter. In other words, the deeper channel does not necessarily induce higher reaction or electron density or temperature. It should be noted that the same design was used for both cases and the target channel width was 800 μm. Using one sweep, figure 4.6 (a), the channel width was exactly 800 μm. However, for figure 4.6 (b), the measured channel width was 840 μm; broadening happens because of (1) the greater channel depth and (2) a limitation of the mechanical arm that controls the laser engraver.

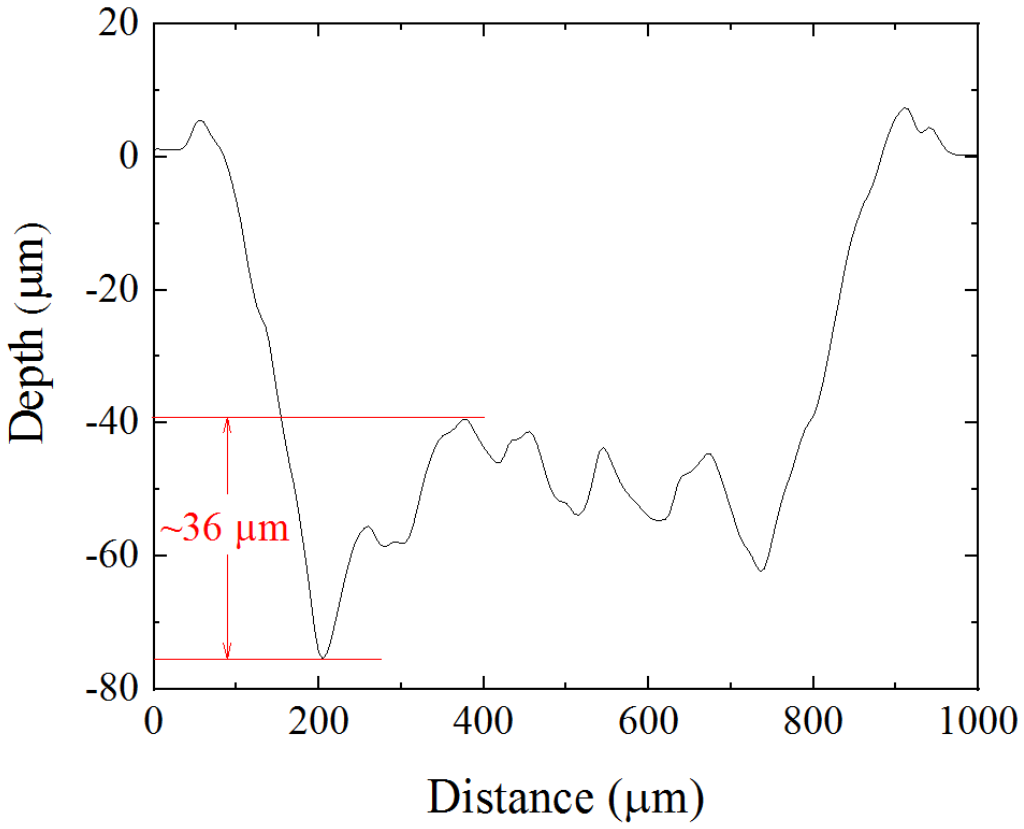

Figure 4.5 Surface profile measurement of an individual microchannel by microstylus profilometry. The depth variation on the bottom was ~36 μm (peak-to-peak), which was similar to the results obtained with an optical microscope (±15 μm).

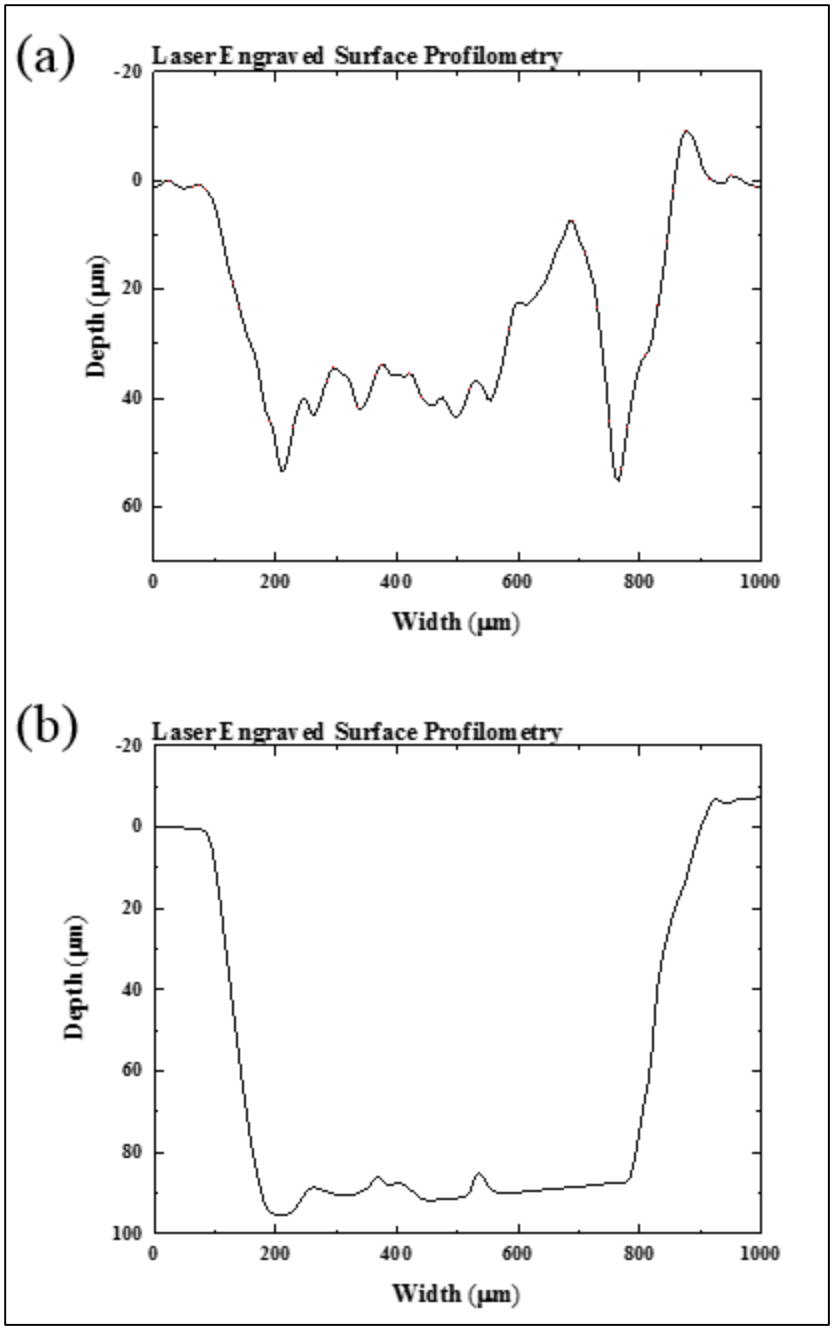

Figure 4.6 Microstylus profilometry obtained by sweeping a single microchannel laser-ablated alumina surface. (a) 20 J/cm^2 laser input was used, and (b) the same 20 J/cm^2 was used but the laser was swept twice on the same surface. The target channel width was 800 μm; (a) was measured to be 800 μm, but (b) was measured to be 840 μm. In short, ~5% broadening occurred by sweeping twice.

Figure 4.7 shows the measured cavity density and the average diameters. Randomly selected regions with areas of 500 μm by 500 μm were taken from the SEM images for the analysis.

The cavity count was ~300 /mm^2, and the average cavity diameter was ~33 μm. Although there existed, rarely, cavities whose diameter exceeded 100 μm, most cavity diameters ranged 10-50 μm.

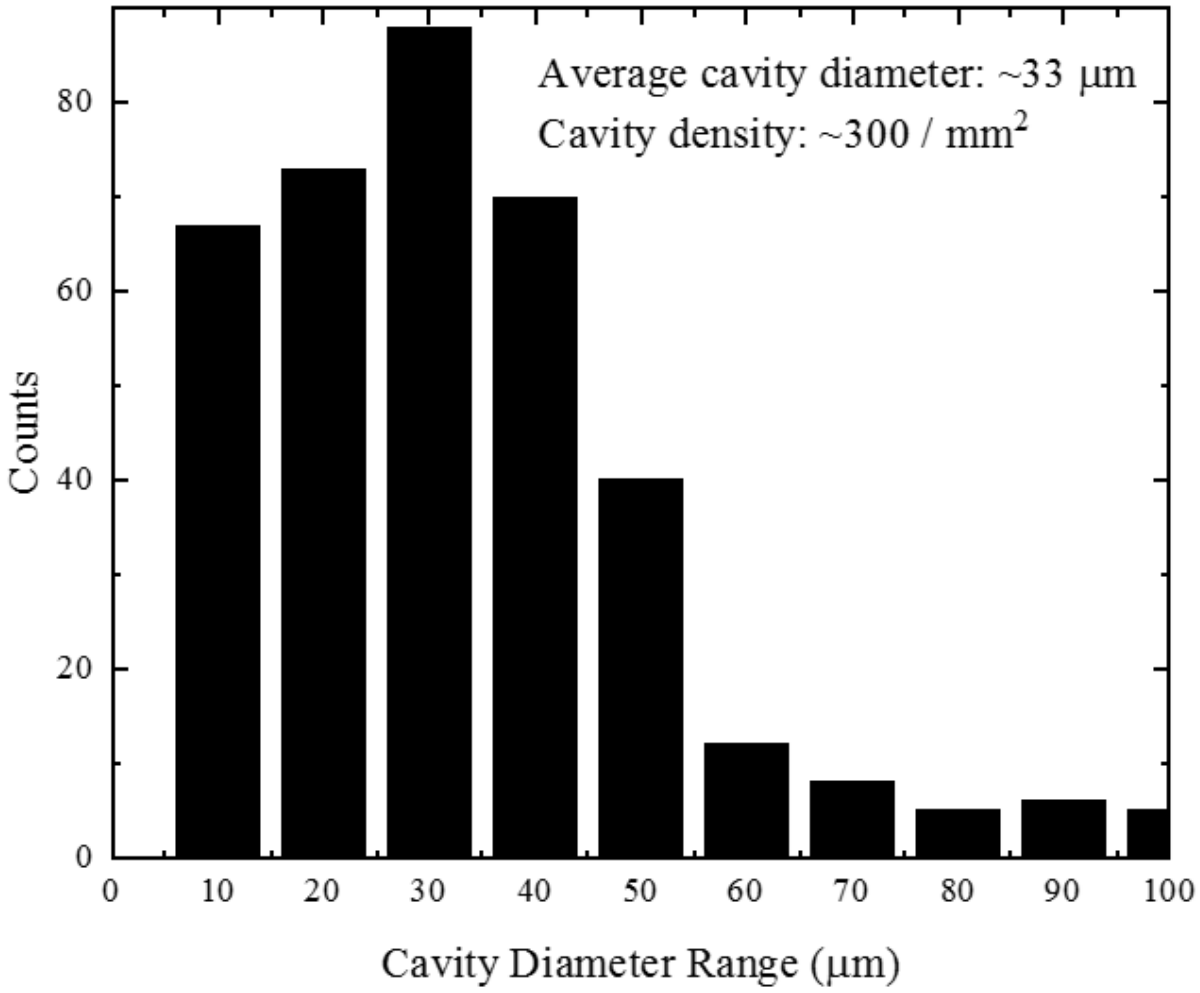

Figure 4.7 Measured cavity density and average diameters. The cavity density and the average cavity diameter were ~300 /mm^2 and ~33 μm, respectively. Most cavities had a diameter in the vicinity of 10-50 μm, even though some cavities had diameters greater than 100 μm. Data was obtained by counting cavities on the SEM images. Five random sites were chosen for the average calculation.

4.2 MICROPLASMAS WITHIN CAVITY SITES

Figure 4.8 shows the top-view SEM image of the edge of the laser-ablated channel. As one can see in this figure and in figure 4.4, it is possible to create cavities (i.e. holes) within the channels. Although randomly generated, these cavities are responsible for having higher surface area without applying any additives or beads. To better describe the topography, figure 4.9 shows the schematic diagram of those nanoporous alumina processed with conventional method and the laser ablation method.

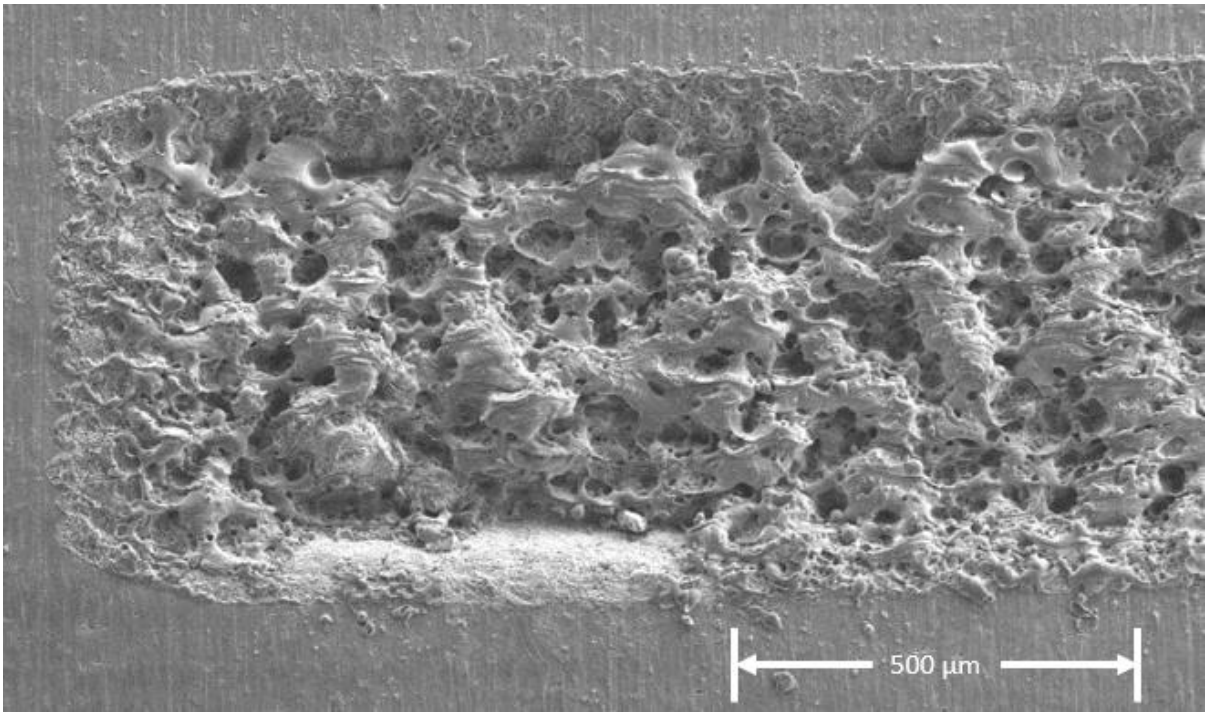

Figure 4.8 Top-view of a single microchannel recorded with scanning electron microscope (SEM). Randomly generated cavities by laser ablation technique are shown.

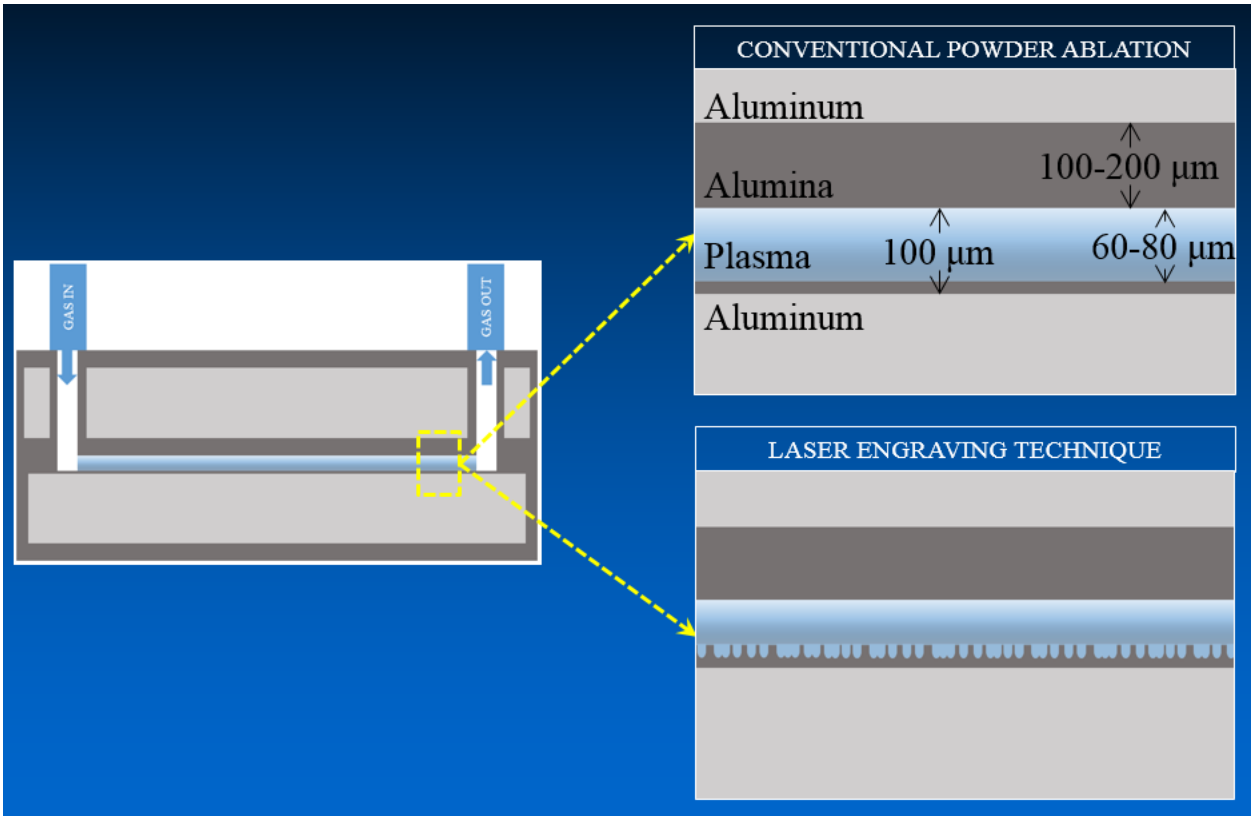

Figure 4.9 Schematic diagram illustrating the topographical difference of the bottom surface when different etching methods were used. Laser ablation creates cavities on the surface. It should be noted that, even though the illustration shows the cavities with relatively uniform diameter, the actual cavity diameter ranges 10-300 µm (refer to figure 4.8).

Figure 4.10 shows the laser-ablated microchannel operation using 300 Torr of argon depending on the applied voltage. Black solid squares represent the ICCD signal inside the cavity, and the red dots show the ICCD signal in the normal microplasma region (i.e. non-cavity region). The top electrode of ITO coated soda lime glass was used in order to observe the optical emission. Figure 4.11 was obtained similarly, and the only difference was the gas species (i.e., Ne instead of Ar).

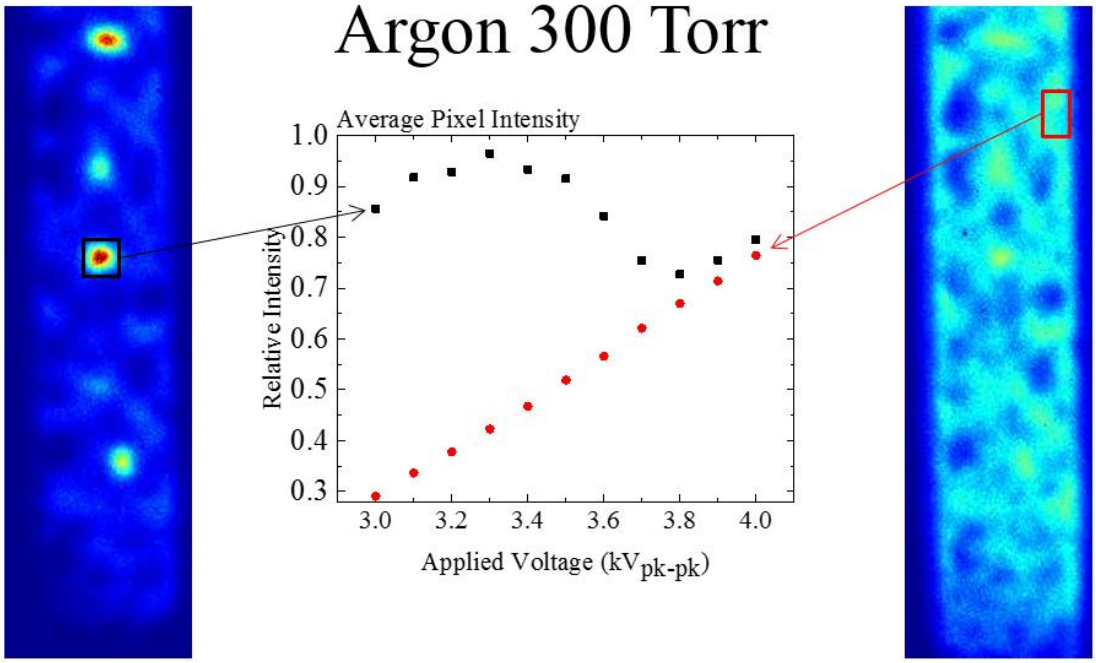

Figure 4.10 Comparison of the relative intensity, obtained by ICCD, difference between inside the cavity (black box and squares) and the general discharging regions (red box and dots) depending on the applied voltage (300 Torr Ar, non-flowing). It should be noted that both regions were in the same microchannel, and they were operated simultaneously. It should also be noted that cavity sites started to discharge first at lower voltages (showing very intense emissions encapsulated inside the cavity).

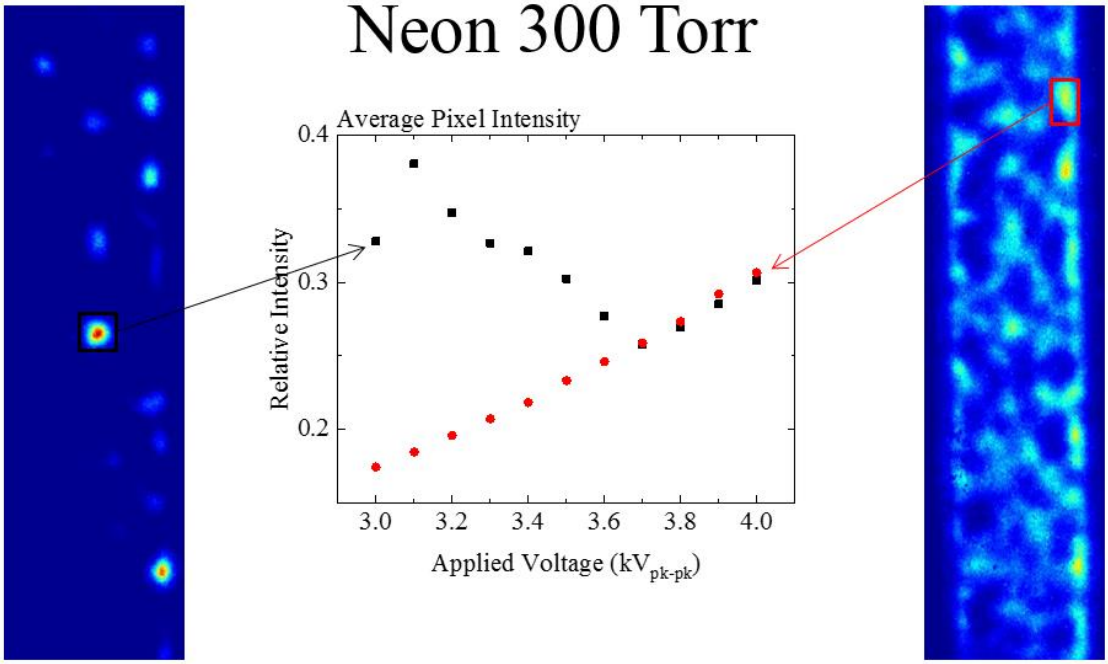

Figure 4.11 Data obtained similar to that of figure 4.10, except neon was used instead of argon. A similar trend in terms of relative intensity was obtained.

When considering the reduction of the cavity diameter, one should think about the minimum possible cavity diameter. Also, there will be no plasma if the cavity diameter is smaller than the calculated sheath thickness. Although the sheath thickness of microplasma cannot be visibly observed because of its small physical size, the approximation of the Debye length can be calculated using the following:

$$\lambda_{\mathrm{De}} = 743\sqrt{\frac{T_e[eV]}{n_e[cm^{-3}]}}\,[\mathrm{cm}]. \tag{4.1}$$

T_e is the electron temperature and n_e is the electron density. Using electron temperature of 3 eV and electron density of ~10^{16} cm^{-3}, the calculated Debye length is ~130 nm. Assuming that the sheath thickness is ~3-10 Debye length, the sheath thickness ranges 390-1300 nm. One should also think that, using the field emission that has a sheath region on each end, the minimum should be twice the approximation shown above. Thus, the cavity diameter should be at least >3 μm. Otherwise, there will be no plasma. In short, the optimum cavity size should be in the vicinity of ~5-100 μm to maximize the field emission effect, and any diameters outside of this range should not have an effective utilization of field emission effect. The measured diameter of those randomly generated cavities using the laser ablation method is within this range, and the surface structure can be well used for utilizing the field emission effect. However, further optimization should take place in order to make those cavities more uniform in terms of shape and size. It should be noted, though, that the sheath thickness depends on the current density as well as the pressure; the optimum sheath size for the individual microhollow geometry can be generalized by the following equation:

$$\sim 6 - 20\,\lambda_{D_e} < \mathrm{d}, \tag{4.2}$$

where λ_{D_e} is the Debye length, and d is the microcavity diameter. It should also be mentioned that the minimum microcavity diameter (the critical diameter) should exceed the mean free path of the interacting molecules in the system.

Figure 4.12 shows a typical waveform for the device operation using the gas flow rate of 100 sccm (pure CO_2) with sinusoidal driven voltage waveform.

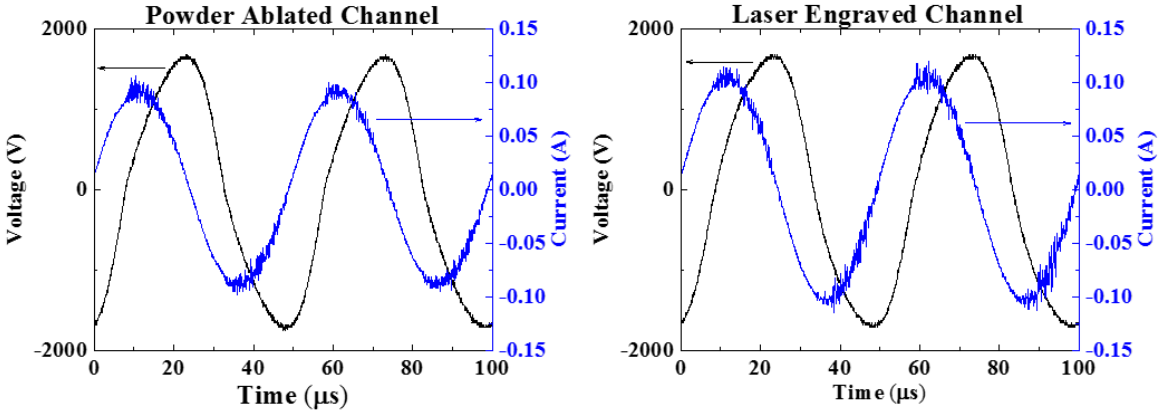

Figure 4.12 Typical discharging voltage and current for the devices made with powder ablation etching method (left) and laser ablation etching method (right). 20 kHz sinusoidal driven waveform was used for the operation.

4.3 CO_2 DISSOCIATION AND O_3 GENERATION

Figure 4.13 shows the current-voltage (I-V) characteristics of the devices made with both laser ablation method and the powder ablation method. As shown in the figure, the laser-ablated device started to discharge at ~850 V_{RMS}, whereas the powder-ablated device started to discharge at ~900 V_{RMS}. The linear fittings of the discharging plots have slopes of 0.088 and 0.082 for the laser ablation method and powder ablation method, respectively. The linear fittings also have x-intercepts of 872 V_{RMS} and 916 V_{RMS} for laser and powder ablation, respectively. Using the breakdown voltages obtained from the experiment and eqn. (2.5), it is approximated that current

density induced by the field emission (J_{FE}) is ~20 A/cm^2. This result is in good agreement with the approximate voltage measured for the breakdown voltage for each case. As one of the characteristics of the field emission effect, figure 4.13 shows higher current at the same given voltages. Also, the slope of the current increase was observed to be higher for the laser-ablated case, and it was also mentioned as one of the characteristics of the field emission effect. Using the linear fit, the calculation shows that the laser-ablated devices have 15-30% higher current, at any given voltage, when compared to the devices made with powder ablation method. In short, both (1) increased conductance of ~25% and (2) lower plasma breakdown voltage were observed for the laser-ablated device.

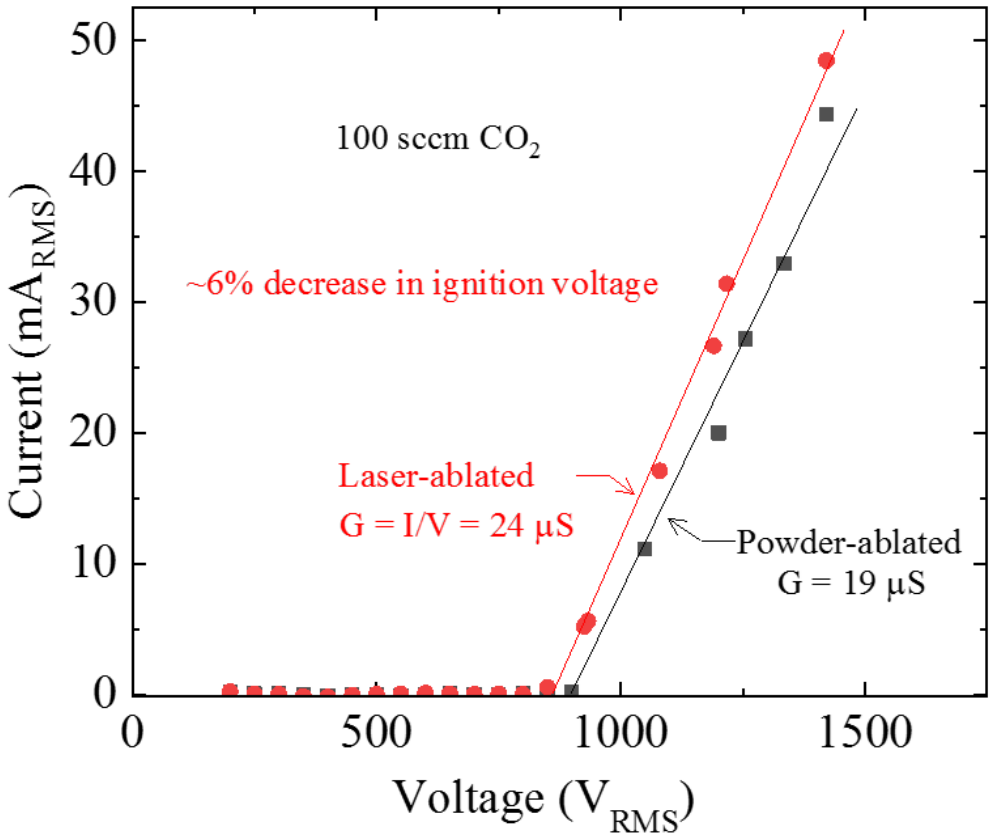

Figure 4.13 Current-voltage (I-V) characteristics of laser-ablated devices (red solid circles) and powder-ablated devices (black solid squares). Note the following: (1) laser-ablated devices started to discharge at slightly lower voltage (~850 V_{RMS}) than that for a powder-ablated device (~900 V_{RMS}), (2) higher current at any given input voltage for the laser-ablated device, and (3) lower slope resistance for the laser-ablated device. Driving voltage is a 20 kHz sinusoidal.

Figure 4.14 shows the comparison of dissociation rate using each method. Pure CO_2 gas is flowed for both cases, and all other experimental parameters were the same except how the devices were prepared. Discharge power was used as abscissa, as operating voltage produces very different current output and so serves poorly for direct comparison of device performance. Instead, the amounts of CO_2 dissociated at the same power were compared. Figure 4.15 shows the theoretical energy efficiency using the dissociation values depicted in figure 4.14. In order to calculate the energy efficiency, it was assumed that all the dissociated CO_2 was dissociated to CO. With this assumption, the following chemical equation could be used to calculate the theoretical energy efficiency:

$$CO_2 \rightarrow CO + \frac{1}{2}O_2\,, \Delta H = 2.9\ \text{eV}. \tag{4.3}$$

With this reaction, the energy efficiency could be calculated by the following equation:

$$\eta(\%) = A \cdot \left(\frac{\dot{m}}{\mu}\right) \cdot \left(\frac{2.9\ \text{eV}}{P}\right), \tag{4.4}$$

where A is the dissociation rate calculated above, $\dot{m}$ is the flow rate of CO_2 into the device, μ is the reduced mass of CO_2 and P is the discharge power of the device. In short, the maximum energy efficiencies obtained were 17.4% and 13.5% for the laser ablation and powder ablation methods, respectively, indicating that laser ablation is ~30% more energy efficient. The fitting shows that the maximum energy efficiency values were 17.7% and 13.6% for the laser ablation and the powder ablation methods, respectively; the maximum discrepancy between the measured data and the fitting was ~2%. This result is achieved without changing any other experimental parameters, so it can be said that the efficiency increase was solely achieved by using the new etching technique.

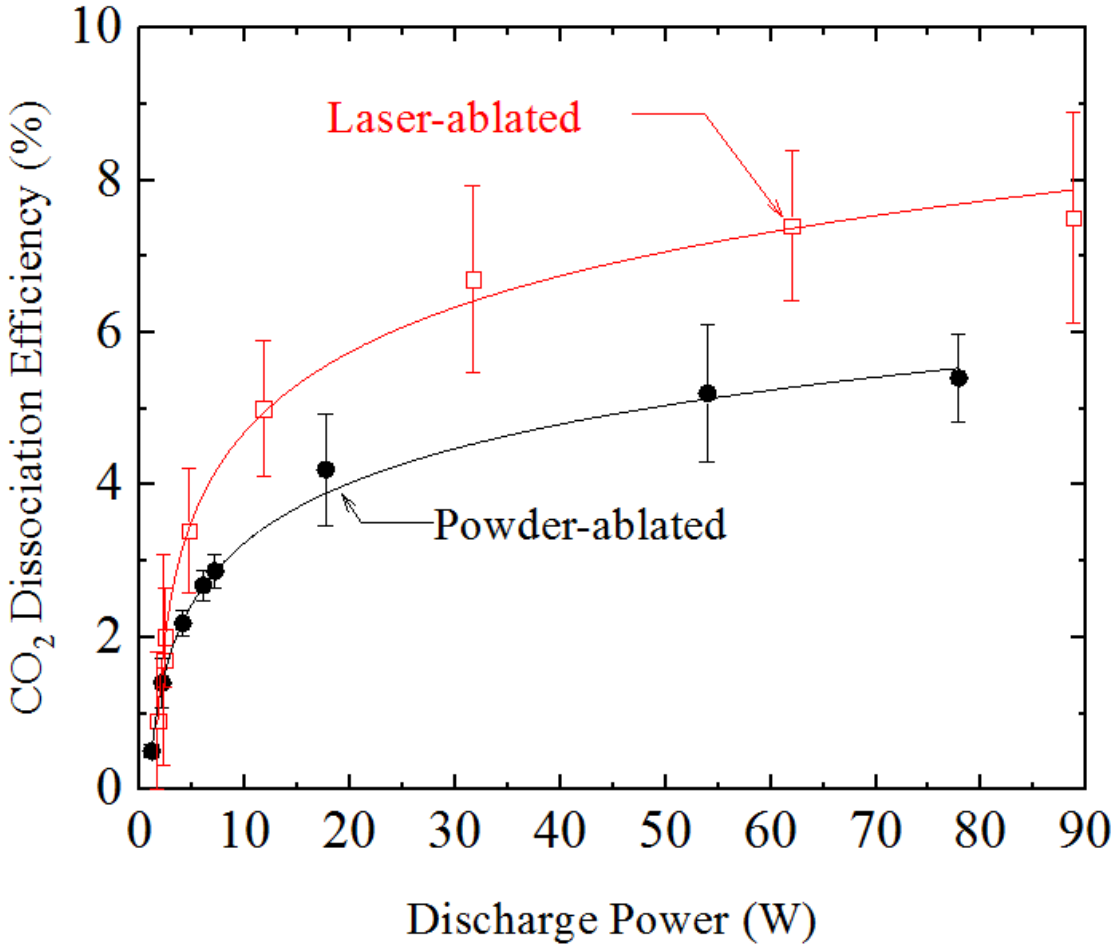

Figure 4.14 CO_2 dissociation rate, using RGA, depending on the etching methods. 100 sccm of pure CO_2 (99.999%) was used. Red squares show the results for the laser processed devices, and black solid circles show the results for the powder-ablated devices. Solid lines show the log fitting, and the error bars indicate $\pm 1\sigma$. As shown in the figure, CO_2 dissociation rate was significantly increased by using the laser ablation method. Other than the etching method, all other parameters were kept the same.

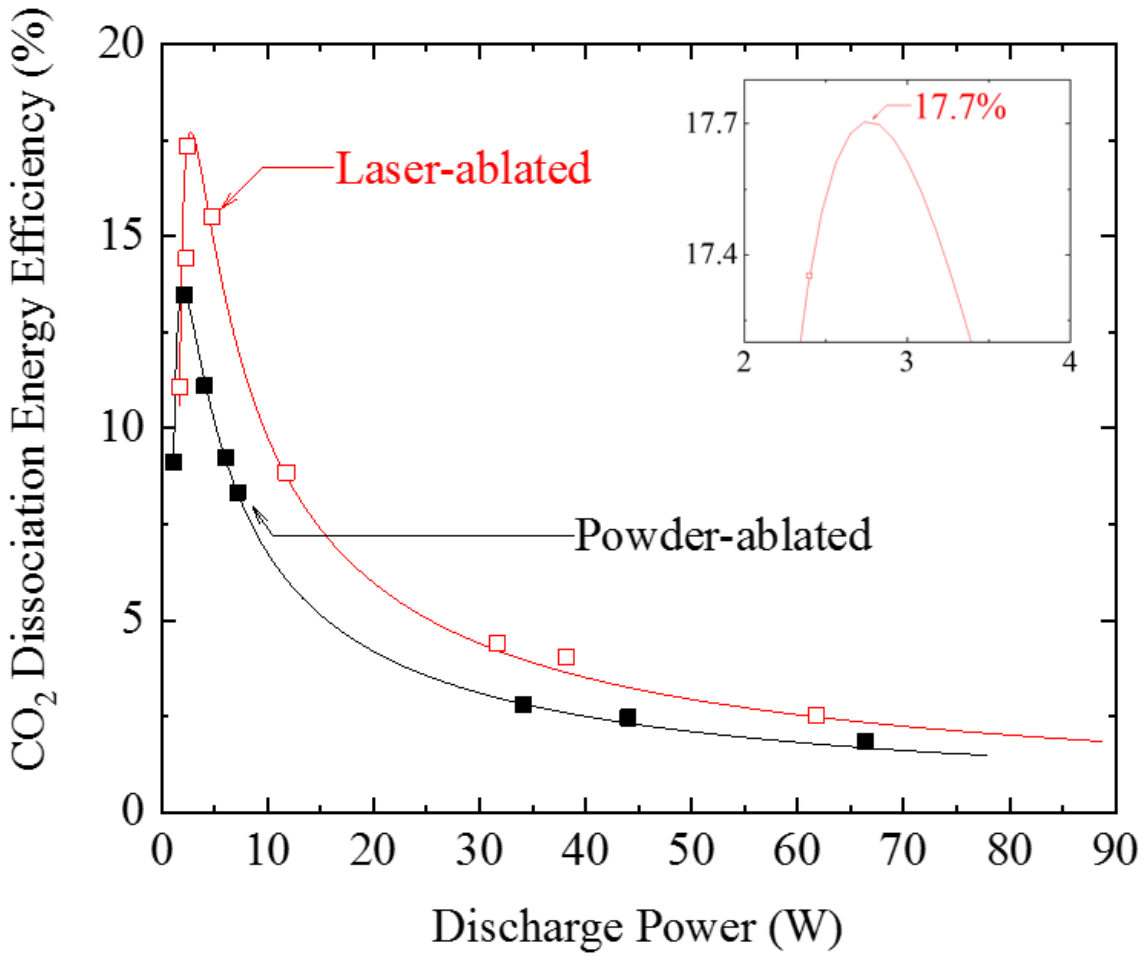

Figure 4.15 Theoretical energy efficiency calculated using the results shown in figure 4.14. Red squares show the laser-ablated device performance, and black solid squares show the powder-ablated device performance. The maximum energy efficiencies obtained by experiment were ~17.4% and 13.5% for the laser-ablated and the powder ablation methods, respectively. Solid lines show the energy efficiency trends using the fitting obtained from the figure 4.14. In short, about 4%p was gained (~30% increase) by using the laser ablation method. It should again be noted that all other experimental parameters were kept the same.

Most plasma systems' dissociation energy efficiency results shown in figure 2.3[27] indicate that most systems have either low flow rate (<20 sccm) or low energy efficiency (<5%). The energy efficiency reported in this dissertation is 17.4%, which is off the ordinate shown in figure 2.3. A system using pulsed corona (reference 17 of the figure and the table) has relatively high energy efficiency that exceeds 14%, but the device lifetime, because of its system configuration (pulsed corona), limits the system's reliability as a dissociation source.

The ionization energy of CO_2 is 13.77 eV. Although this is not the only reaction that leads to the dissociation, higher dissociation rate indicates there are now more electrons that can reach this energy level. With only the topographical difference, it is obvious that the surface interaction is responsible for electron energies being skewed even higher.

For the ozone generation comparison, the standardized test taken at the EP Purification was used. EP Purification is a corporation that manufactures a commercial-grade ozone generator. Although the details of the device geometry cannot be discussed because of the intellectual property protection, it was possible to use their tools to test the devices. The testing conditions are as follows:

1) Device aging (pre-test): 1 hour
2) Flow rate: 1.0 to 5.0 lpm
3) Power: 15 W fixed
4) Device cooling: air cooled (fan)
5) Feed gas: >95% oxygen using oxygen concentrator

Using these experimental parameters, it was possible to compare the laser-ablated and the powder-ablated device performance as an ozone generator. Figure 4.16 shows the ozone production efficiency at various flow rates. Depending on the flow rate, the overall ozone generation efficiency of laser ablation is reported to be ~7.1-11.2% better than that of powder ablation.

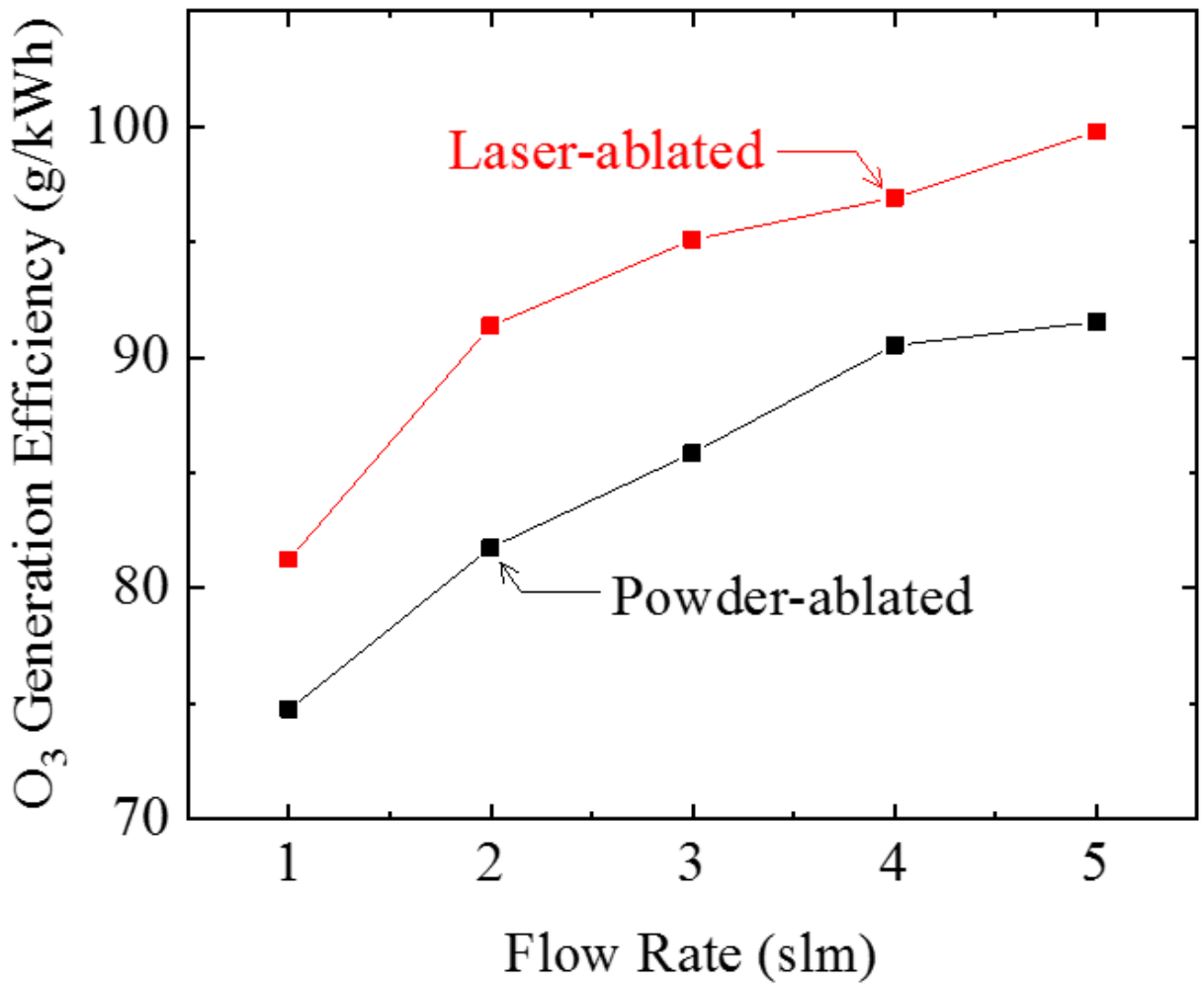

Figure 4.16 Ozone generation efficiency comparison between laser-ablated devices and powder-ablated devices. A standardized test developed by EP Purification was used for this experiment. Depending on the flow rate, an overall efficiency increase in the range of ~7-11% was observed for the laser ablation method. It should also be mentioned that, except for the etching method, all other parameters, including the channel geometry, were kept the same.

In short, the CO_2 dissociation and O_3 generation were measured in order to test the performance improvement caused by changing the etch technique to laser ablation rather than powder ablation. The laser-ablated devices show ~29% and ~7-11% improvement for the CO_2 dissociation and the O_3 generation efficiency, respectively. Since every effort was made to keep

all experimental parameters except the etching technique identical, it can be said that this improvement came from changing the etching technique to the laser ablation method.

4.4 CARBON DIOXIDE (CO_2) AND HYDROGEN (H_2) MIXING

Along with CO_2, hydrogen (H_2) was introduced into the microplasma to observe the interaction between them. The experiment was conducted and evaluated chemically and optically. For the optical observation, the optical device described above is effective in terms of observing the plasma chemistry inside the microchannels. However, the thickness of ITO coated glass, which is at least 400 μm, reduces the electric field significantly. In order to keep the electric field the same as that in the actual chemical reactor described in this dissertation, two alumina plates were used for the observation reported in this section; the plasma emission was observed from the tubing area. By using two alumina plates, it was possible to keep the inter-electrode distance to ~200-300 μm, whereas, if ITO coated glass was used, the optical device described above would have ~500 μm inter-electrode distance. Figure 4.17 shows the schematic of the experiment configuration. The optical emission spectrum was taken with an Ocean Optics Miniature Spectrometer, which has an observation range of 350-1032 nm with resolution of 1.42 nm. Dark spectrum was taken and subtracted from the recorded spectrum, and the integration time of 5 seconds was used for all experiments. Both CO_2 and H_2 gas flows were controlled by the volumetric mass flow controller (Aalborg), and H_2 volumetric composition ranging 0-50% was tested; the total flow rate was set to be 50 sccm for all the experiments described in this section.

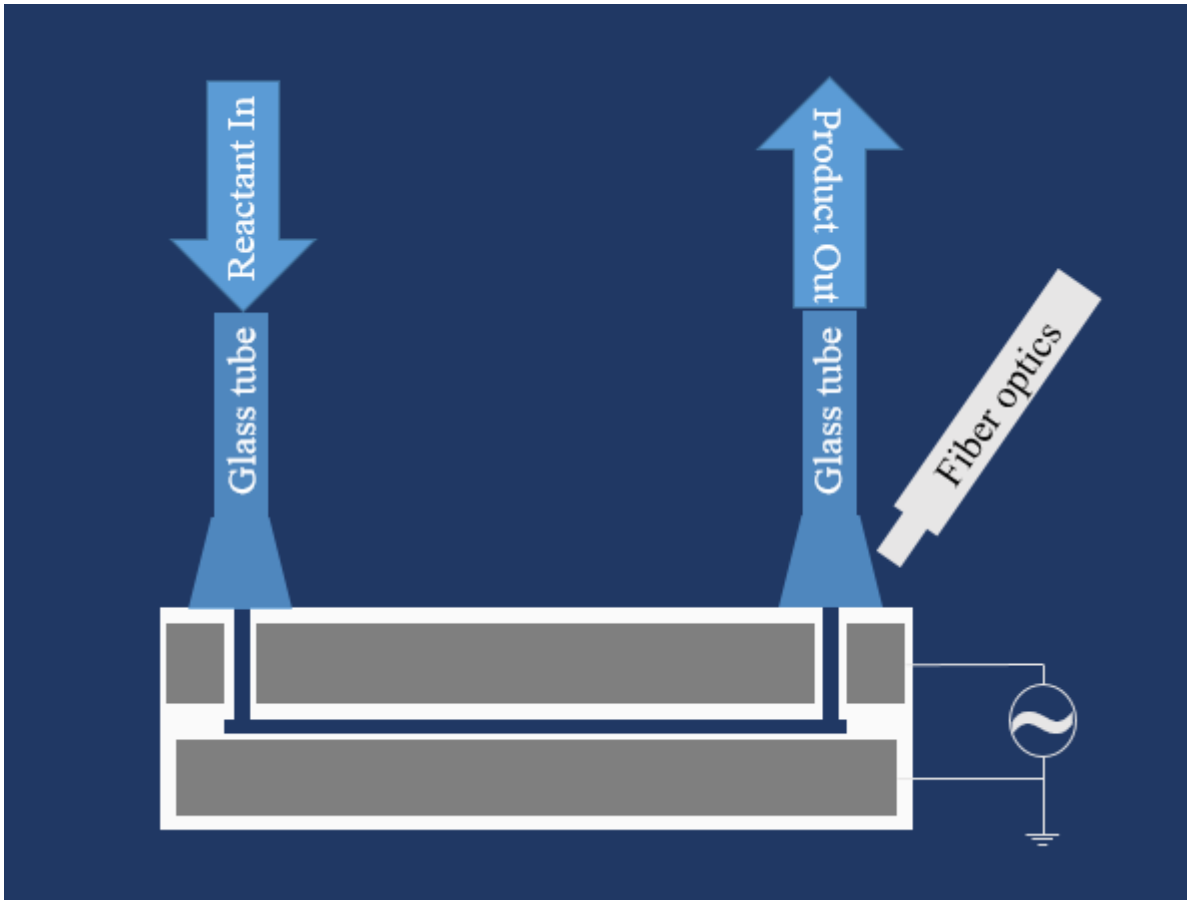

Figure 4.17 Experiment schematic for the optical observation. Two Al/Al_2O_3 plates were used, instead of ITO coated glass on the top side, in order to keep the dielectric properties and the thickness identical to that of an actual reactor. In-situ optical emission spectroscopy was enabled by observing the light emission from the tube side of the output port.

It is very interesting to compare the results taken from laser-ablated devices to those from powder-ablated devices. Figure 4.18 shows the normalized intensity of the optical spectroscopy using 50 sccm of CO_2; both of them were discharging at 1.6 kV_{RMS}. It should be noted that the normalization factors are different for each line; the relative intensity of laser-ablated devices was higher than that of powder-ablated. This was expected because, at the same voltage, laser-ablated devices carry higher currents.

Another factor to consider, in figure 4.18, is the region indicated as "afterglow". According to Fowler and Gaydon,[66] this afterglow is the CO_2 afterglow, which is produced by the direct

combination of CO and O_2 without dissociation into atoms of carbon and oxygen or molecules of carbon. In other words, the higher the afterglow region, the higher the recombination rate. Thus, the normalized intensity of the spectrum shows how much energy is allocated to the afterglow, CO_2^+ Fox-Duffendack-Barker (FDB) bands and CO Angstrom bands; the figure obviously shows that there is much less afterglow for the laser-ablated case, compared to that of the powder-ablated case. The afterglow-to-peaks ratio is lower for the laser-ablated device compared to that of powder-ablated, indicating that less recombination occurs.

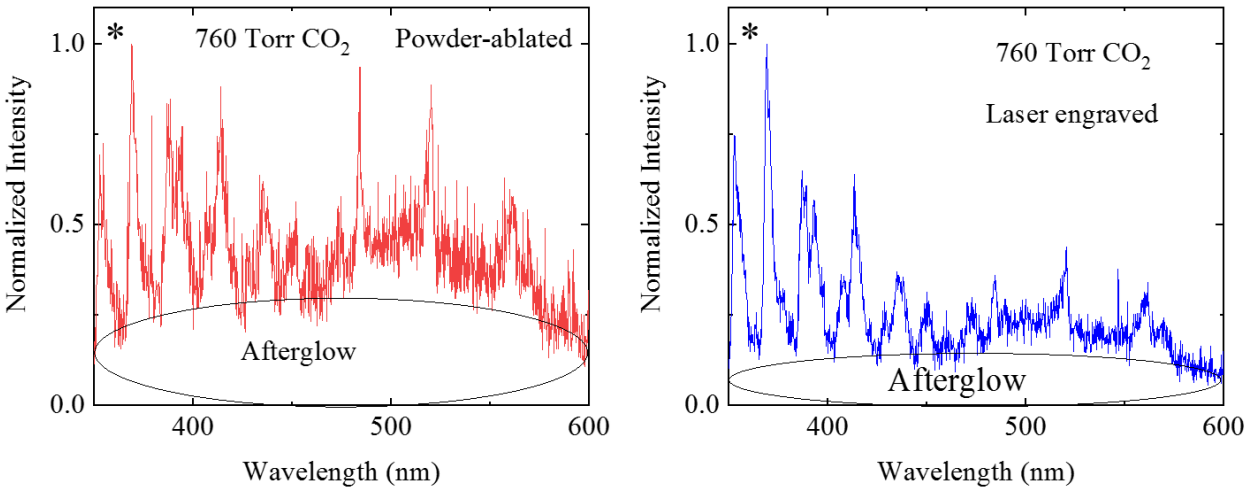

Figure 4.18 Normalized emission spectrum of microplasma discharge observed for powder-ablated device (left) and laser-ablated device (right). The highest peak (denoted with asterisk in each figure) was set to be 1 for the normalization of each case. Flow rate of 50 sccm using pure CO_2 was used, and the operation voltage was kept at 1.6 kV_{RMS} for both cases. The afterglow region broadly expands from ~350-600 nm. Significantly reduced afterglow, which is coming from the recombination of the CO_2, was observed for the laser-ablated device; less reverse reaction occurs, which indicates higher dissociation rate for the CO_2. Although this figure does not compare the relative emission intensity between the two cases because the figures were normalized, the integration of the area under the peaks from 350-600 nm showed that laser-ablated device emitted ~46% higher intensity compared to that of powder-ablated device.

Figure 4.19 shows the optical emission spectrum taken similarly to figure 4.18, except the gas used was 25/25 sccm of CO_2/H_2 mixtures. Again, the spectrum of the laser-ablated device shows much less afterglow and more distinct peaks than that of the powder-ablated device.

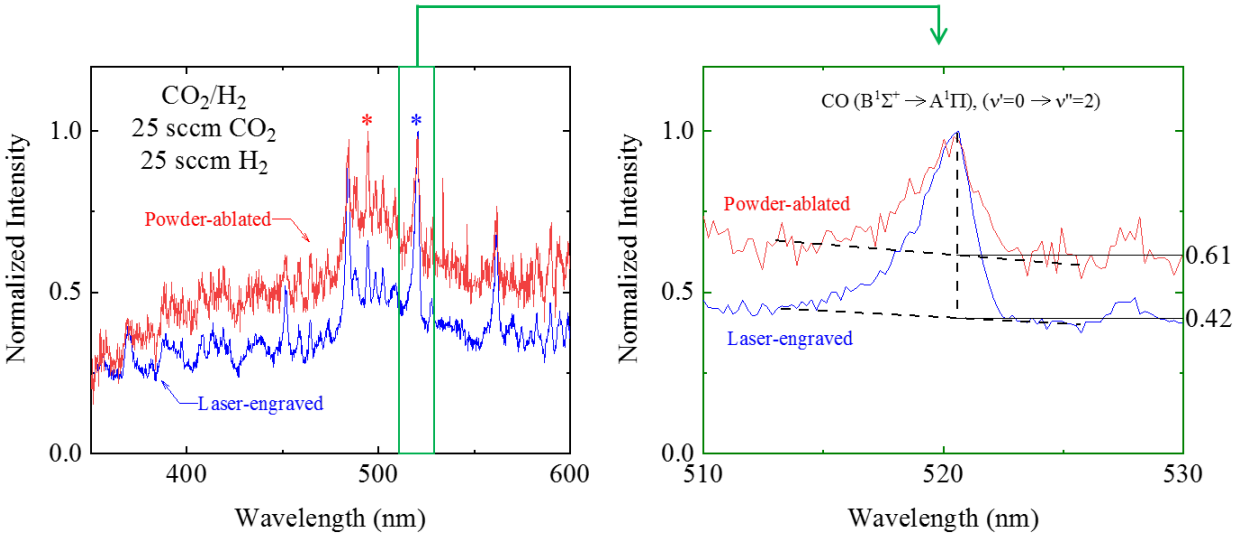

Figure 4.19 Optical emission spectrum data taken similar to that of figure 4.18, except 25/25 sccm of CO_2/H_2 was used for the gas flow. Asterisks show the highest peaks for each case for the normalization. Although the figure on the left shows the suppressed afterglow region for the laser-ablated device, the figure on the right was used to approximately quantify how much the afterglow was out of the total peak. One of the CO Angstrom peaks (v'=0→ v''=2) was used for the approximation. One more thing to note is that, as H_2 composition increased, CO Angstrom bands started to dominate; more detailed spectra are shown in figure 4.20. Furthermore, even though this normalized intensity does not show it, the relative intensity was ~2 times higher for the laser-ablated device.

Figure 4.20 shows the optical emission spectra of laser-ablated microplasma using various volumetric compositions of CO_2/H_2. Figure 4.20 (a)-(e) show the relative intensity of each composition, and (f) shows the combined. As shown in the figure, the overall emission (the area integration) increases as H_2 composition is increased.

Furthermore, as H_2 composition was increased, the ratio of the integrated area under the CO Angstrom system started to dominate, whereas CO_2^+ FDB system started to diminish. CO_2^+ ($\tilde{A} \rightarrow \tilde{X}$) FDB expands from the 325.4-434.2 nm range, whereas CO ($B^1\Sigma \rightarrow A^1\Pi$) Angstrom system expands from 451.1-608 nm. The assignment of FDB system and Angstrom system can be found in the author's master's thesis.[26] This phenomenon can be explained by the interaction of CO_2 and H_2. Considering several reactions of CO_2,

$$CO_2 \leftrightarrow CO + \frac{1}{2}O_2, \tag{4.5}$$

$$CO_2 \leftrightarrow CO_2^+ + e^-. \tag{4.6}$$

These two reactions show the dissociation and ionization of CO_2. By consuming ionized CO_2 (i.e. CO_2^+), the product population of the eqn. (4.6) gets reduced, which favors the forward reaction. Something similar happens for eqn. (4.5). As atomic O is reacting with atomic H, products including hydroxide can be formed, which makes the product population decrease and favors the forward reaction. Figure 4.21 shows the normalized intensity, which undoubtedly shows the ratio change between CO_2^+ FDB and CO Angstrom Systems. The operation voltage was kept at 1.6 kV_{RMS} with sinusoidal driven waveform.

In short, the emission spectroscopy observation shows that, by introducing H_2 into the system and letting its products (ionized/dissociated/excited H_2) react with CO_2 products, the relative population of CO_2^+ diminished while CO bands increased.

Chemical analysis using RGA was conducted. Figure 4.22 is the RGA data taken using various H_2 compositions. As shown in figure 4.22, mass 46 increased as H_2 composition was increased. Also, mass 1 and mass 16 decreased, indicating they were consumed by secondary reactions. Mass 17 (OH) signal was increased, which shows the formation of hydroxide. Furthermore, the increasing CO_2 dissociation rate as the H_2 composition increased, shown in Figure 4.23, indicates that the reverse reaction (i.e. going back to CO_2 from either excited states or dissociated molecules) was hindered by the secondary reactions with hydrogen.

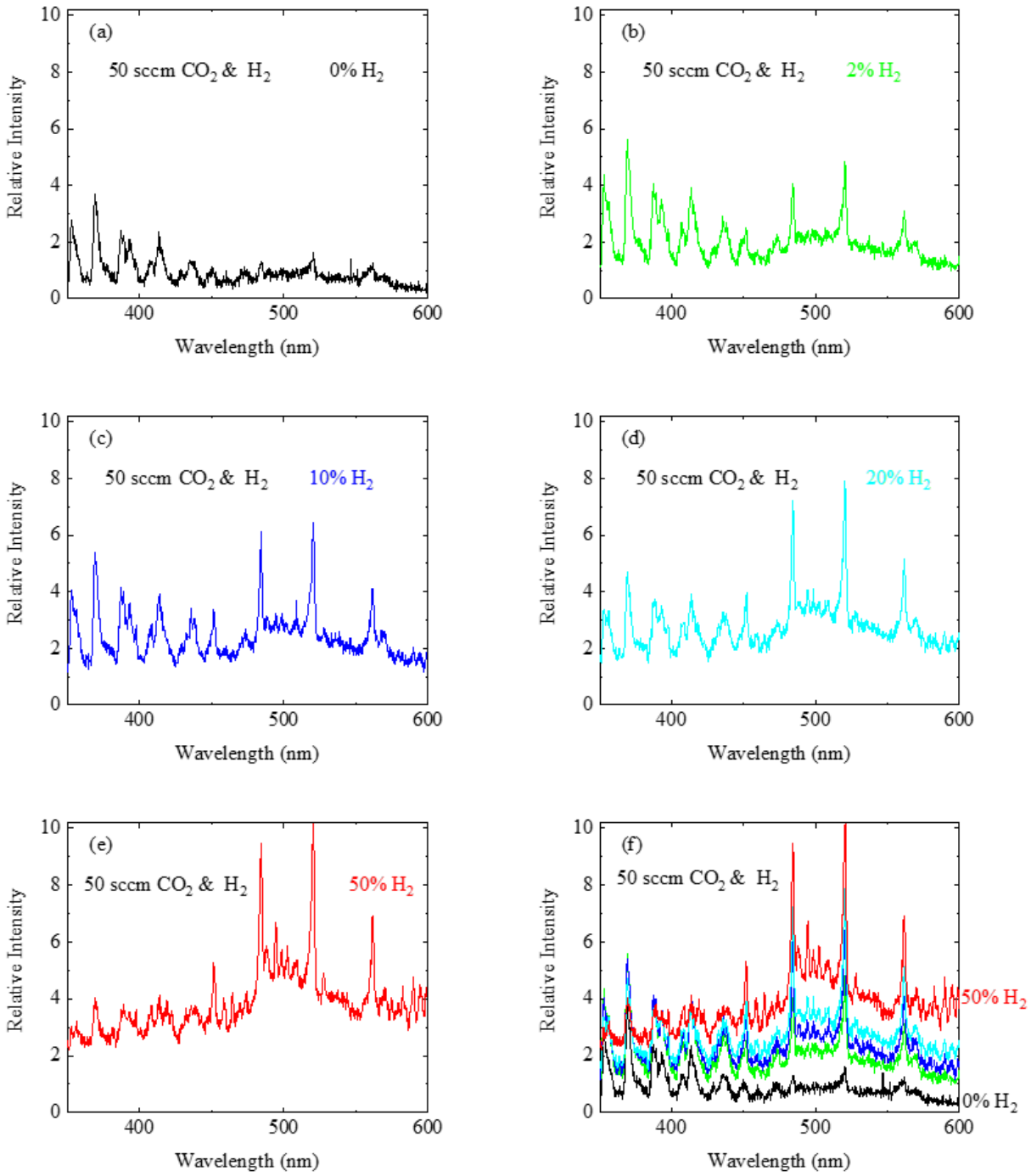

Figure 4.20 Optical emission spectroscopy using various compositions of H_2 into CO_2. Device configuration and the observation schematic are shown in figure 4.17. Optical spectrometer from Ocean Optics was used for the measurement (resolution: 1.42 nm), and the total volumetric flow rate of 50 sccm was used for all cases. (a) - (e) show 0, 2, 10, 20, and 50% H_2 volumetric composition, respectively. (f) shows all combined spectra from (a)-(e). It should be noted that the relative intensity increases as H_2 composition increases. Also, CO_2^+ ($\tilde{A} \rightarrow \tilde{X}$) FDB band systems (325.4-434.2 nm) start to diminish, whereas CO ($B^1\Sigma \rightarrow A^1\Pi$) Angstrom bands (451.1-608 nm) start to dominate as H_2 composition is increased, indicating that the device is more capable of making CO instead of exciting CO_2 and ionizing it. The operation voltage was kept at 1.6 kV_{RMS} with 20 kHz sinusoidal waveform driven.

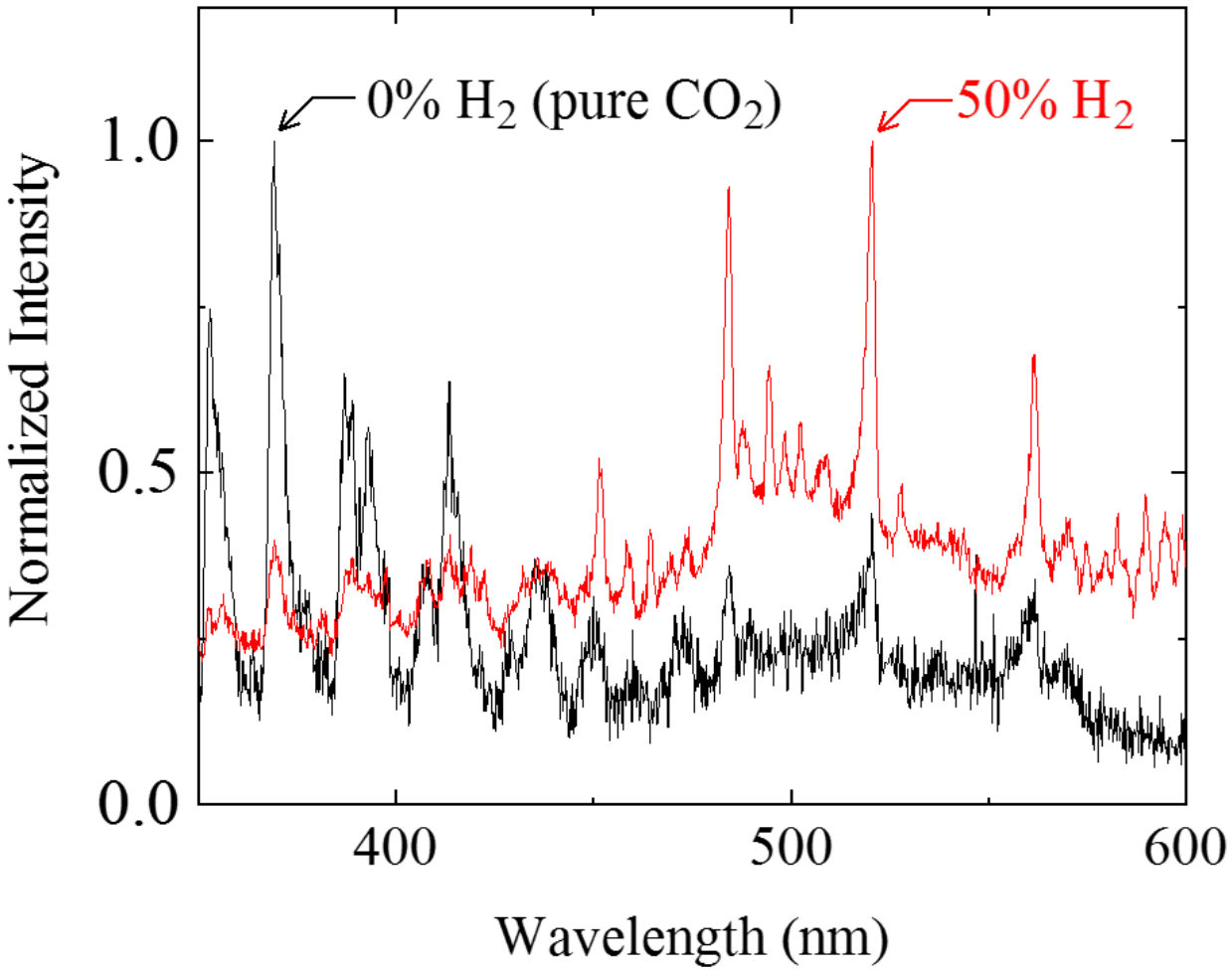

Figure 4.21 Normalized optical emission spectroscopy of 0% (black line) and 50% (red line) from figure 4.20 (a) and (e). CO_2^+ peaks diminished when H_2 was introduced, and CO Angstrom bands started to dominate. Analysis similar to that depicted in figure 4.19 was done; peak-to-afterglow ratio was 1.25:1 and 0.75:1 for the 50% H_2 and 0% H_2 case, respectively.

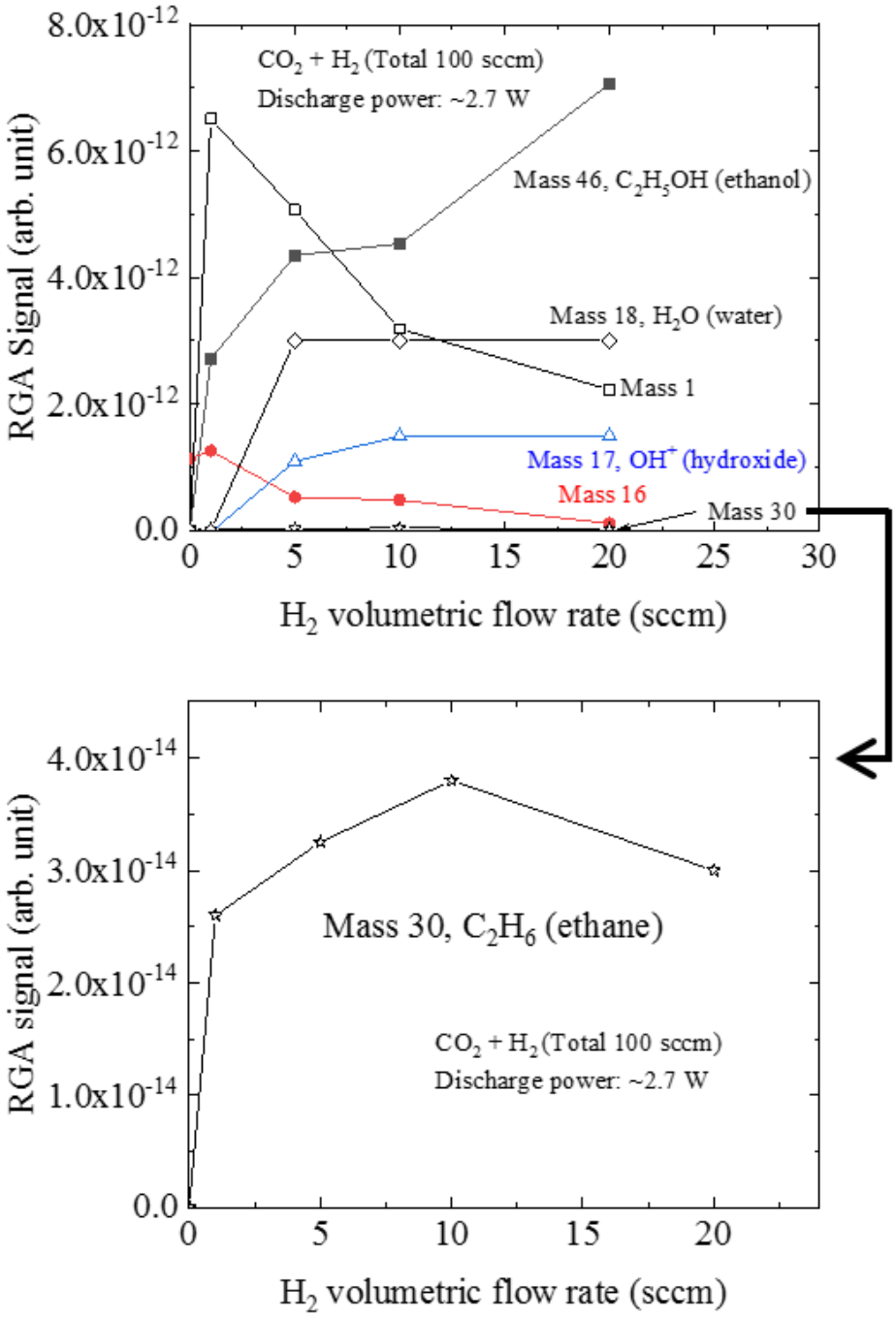

Figure 4.22 (Top figure) RGA data signal trends for various masses depending on H_2 volumetric composition. Total flow rate of 100 sccm was used. Traces of mass 1 (atomic hydrogen), 16 (atomic oxygen), 17 (hydroxide), 18 (water), 30 (ethane), and 46 (ethanol) were observed. (Bottom figure) RGA data for the mass 30, which is expected to be ethane or formaldehyde. Although about two orders of magnitude lower signal than other masses, significant increase in the mass signal 30 was detected (from 10^{-16} to 10^{-14}) once H_2 was introduced into the system. The signal was increasing, then decreased at 20% H_2 composition, a trend similar to that of absolute amount of CO_2 dissociation (refer to figure 4.23 bottom figure). This shows that, under the assumption that dissociated CO_2 mostly becomes CO, the formation of mass 30 is dependent on the absolute dissociation amount of CO_2. Mass 29 was also detected as soon as 1 sccm H_2 was added to the system, but the signal was constant regardless of the H_2 composition.

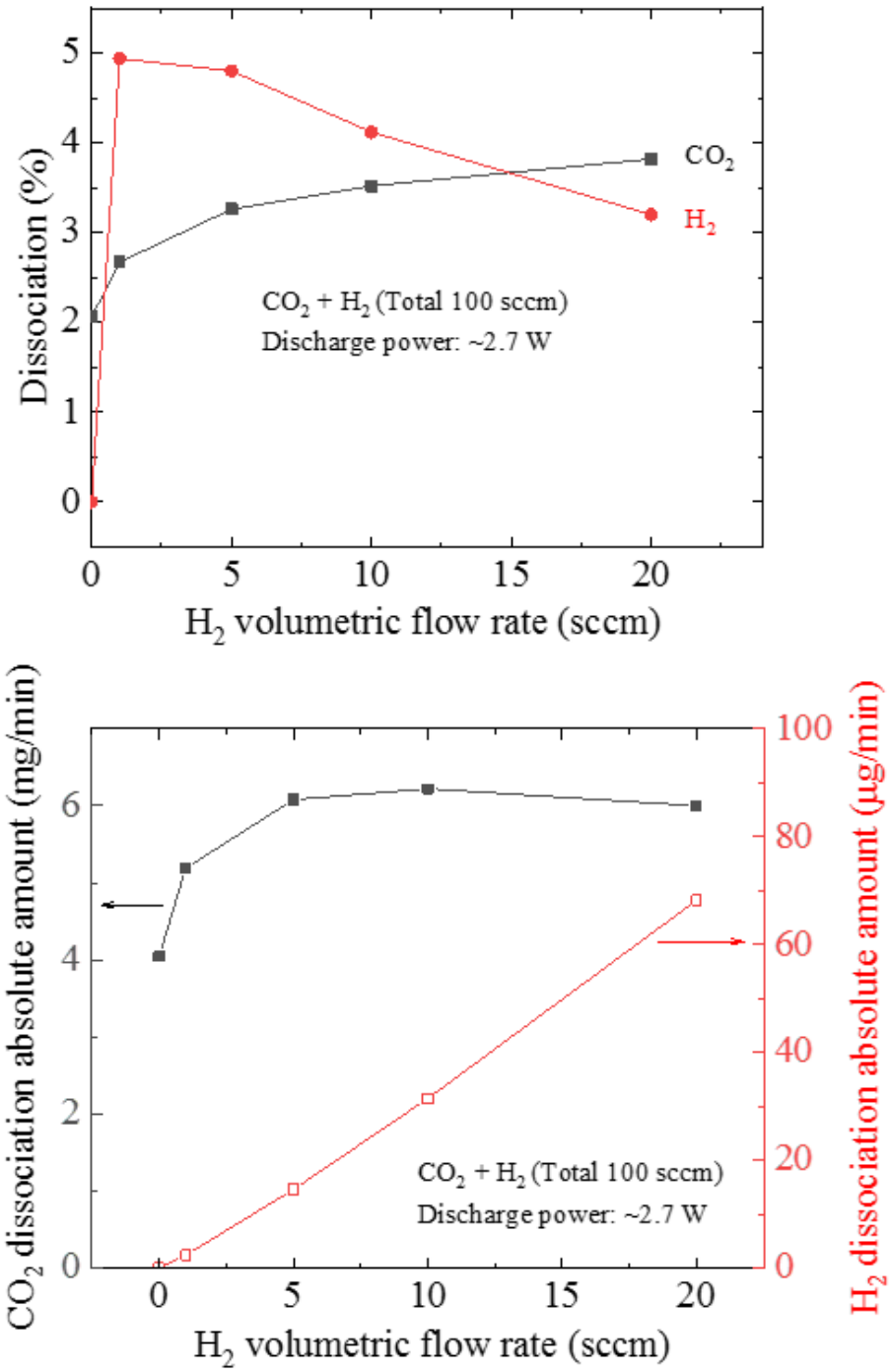

Figure 4.23 (Top figure) Dissociation rate change depending on the H_2 volumetric composition change. The discharge power was kept at ~2.7 W. CO_2 dissociation rate was increased as H_2 composition was increased. It was speculated that, as dissociated and ionized CO_2 was going into the secondary reaction with dissociated/ionized H_2 (refer to the eqn. (4.5) and (4.6)), the product population decreased because now the rate constant for the reverse reaction is decreased. Thus, higher CO_2 dissociation was achieved. (Bottom figure) The absolute dissociated amount of CO_2 (black solid square) and H_2 (red blank square) depending on the H_2 volumetric composition in the CO_2 plasma system. The trend of the amount of CO_2 dissociated is very similar to the formation of the mass 30 (refer to the figure 4.22 bottom figure).

For the CO_2 dissociation, it should be noted that the absolute amount of CO_2 dissociation decreased when 20% volumetric composition of H_2 was mixed. This can be explained by using the chemistry simulation of CO_2 hydrogenation using the one-dimensional DBD fluid model study done by De Bie *et al.*[67] Considering the recombination (i.e. going back to CO_2), the following three reactions are responsible:

$$CO + H \rightarrow CHO, \tag{4.7}$$

$$CO + O \rightarrow CO_2, \tag{4.8}$$

$$CHO + O \rightarrow CO_2 + H. \tag{4.9}$$

Although eqn. (4.7) does not have CO_2 formation directly, it should be mentioned because, in CO_2/H_2 mix plasma reaction, CHO radical is the main reactant that leads to CO_2 recombination (refer to eqn. (4.9)). Back to the reaction coefficient, the reaction coefficients of each reaction from (12)-(14) are 10^{17}, 10^{15}, and 7×10^{15} $cm^{-3}\cdot s^{-1}$, respectively. In other words, comparing the reaction coefficients of eqns. (4.8) and (4.9), the latter is more responsible for the recombination to CO_2. The overall equilibrium state of CO_2 dissociation in the plasma favors the forward reaction (i.e. high concentration of CO does not cause the recombination). High concentration of H is what is responsible for the recombination of CO_2. Thus, excess H does induce higher recombination rate of CO_2. Thus, there exists an optimal CO_2/H_2 composition that has the highest CO_2 dissociation rate. From the experiment, it was concluded that H_2 volumetric composition ranging 5-10% is optimal for the maximum CO_2 dissociation.

By changing only one parameter, the surface topography, higher reaction rate was achieved. Owing to the field emission effect within the cavities, mean electron energy is now even more non-Maxwellian and pushed further to the higher energy. This fact causes individual electrons to

have higher chance to ionize and dissociate (good for the reactor) rather than relax or contribute to the non-significant reactions such as afterglow (not good for the reactor). Furthermore, introducing H_2 into the system stabilizes the products rather than letting them have the reverse reaction; it was observed, though, that there exists an optimum amount of H_2 that can be added in order to get the best dissociation result. In this section, access to the higher electron energy using the laser ablation method was discussed. In section 4.5, higher electron density achieved by using the laser ablation method will be discussed.

There is a reason why figure 4.22 and 4.23 were obtained with the discharge power of ~2.7 W. As shown in figure 4.15, the energy efficiency of the CO_2 dissociation was the highest at ~2.7 W. Using the dissociation rate shown in figure 4.23, figure 4.24 shows the theoretical energy efficiency using various flow rates of H_2 ranging from 0-20 sccm out of the total flow rate of 100 sccm. It can be said that this figure is the summary of this whole dissertation. The very first motivation of this dissertation was to increase the energy efficiency of the CO_2 dissociation and, by combining (1) field emission effect (laser-ablated) and (2) H_2 mixing, the maximum energy efficiency of 23.5% was achieved.

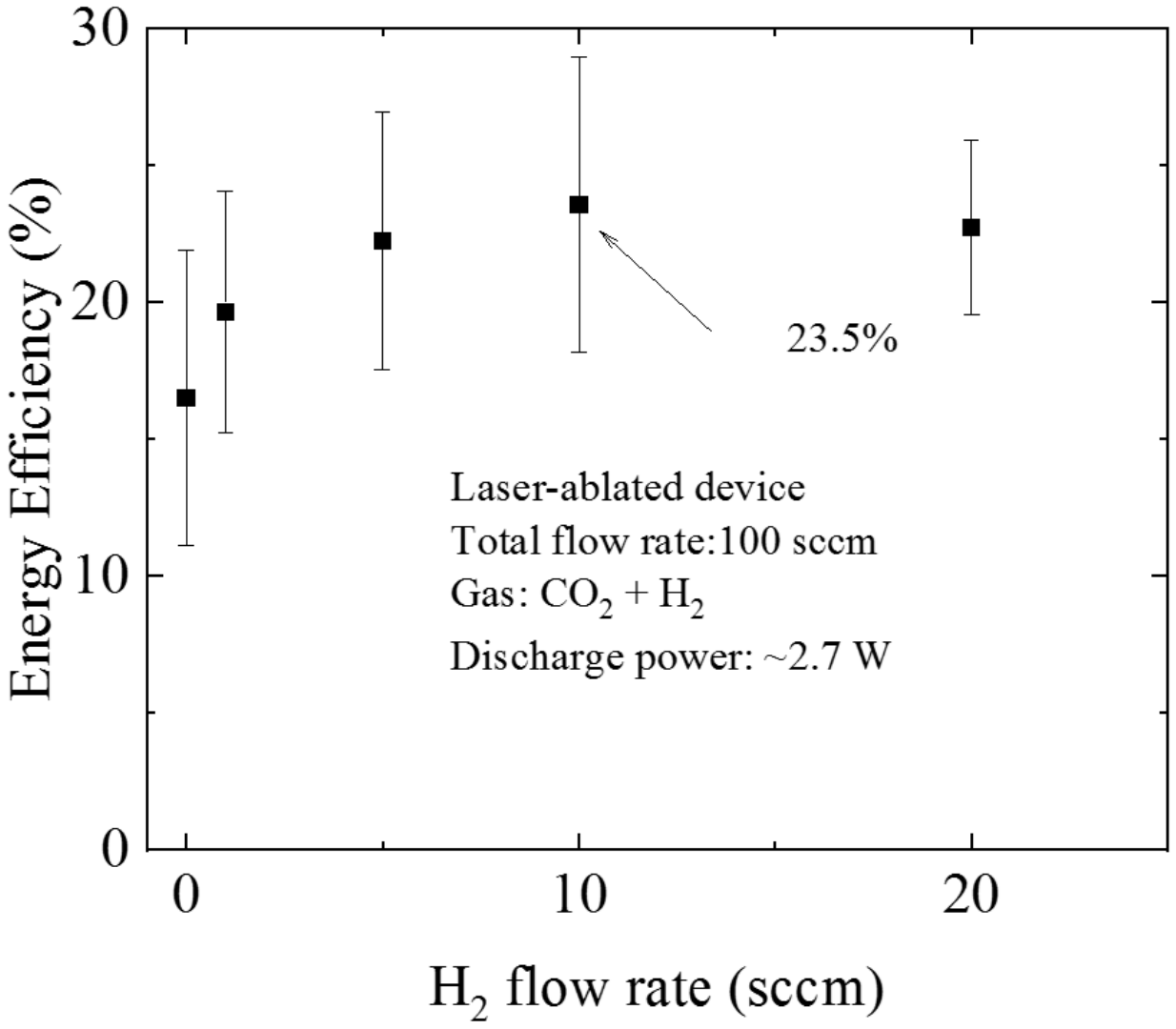

Figure 4.24 Theoretical energy efficiency of CO_2 dissociation. Laser-ablated device with CO_2/H_2 gas mixture was used, and the discharge power was set to be ~2.7 W. Error bars show ±σ. Combining the field emission and H_2 mixing effect, the best experimental energy efficiency was 23.5% when 10% H_2 was used.

Figure 4.25 shows the calculated theoretical energy efficiency comparing each technique. "MP + FE" denotes microplasmas and field emission effect, and "MP + FE + H_2" denotes microplasmas and field emission effect and hydrogen mixing.

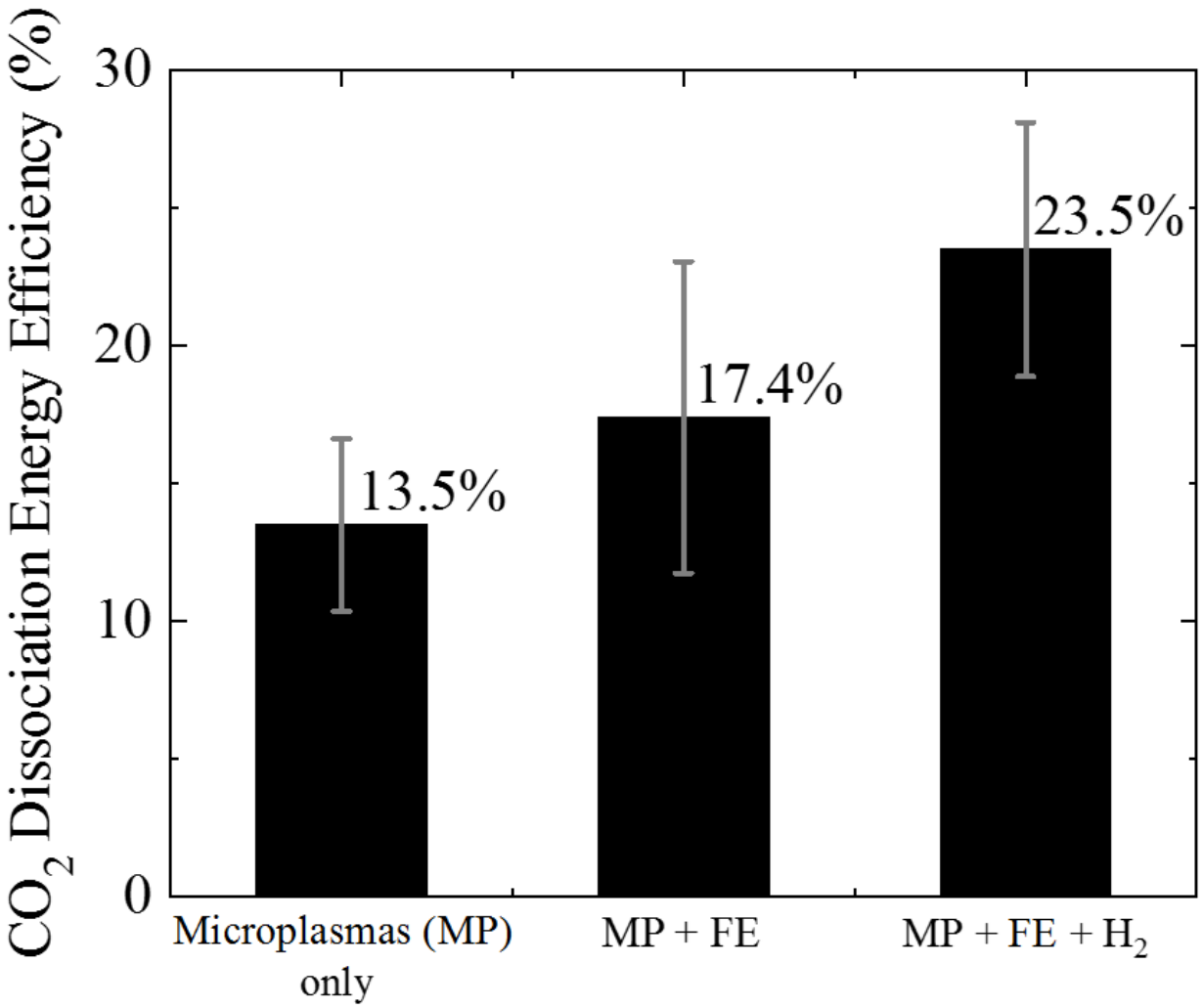

Figure 4.25 Calculated theoretical energy efficiency comparing each technique. "Microplasmas (MP) only" denotes the result using conventional microplasma device (powder-ablated device), "MP + FE" denotes microplasmas and field emission effect (laser-ablated device), and "MP + FE + H2" denotes microplasmas and field emission effect and hydrogen mixing (laser-ablated device with 10% volumetric H_2 mixing with the total flow rate of 100 sccm). Error bars show ±1σ.

4.5 ELECTRON DENSITY MEASUREMENTS BY STARK BROADENING

Although the exact average electron energy increase could not be obtained, electron density could be obtained using the Stark broadening.[68-70] For this experiment, static 300 Torr Ar + H_2 (1% H_2 by volume) gas was used. Although the exact electron density of this experiment will be different from that using pure CO_2 with atmospheric pressure, the experiment conducted and described in

this chapter illustrates well the electron density difference between the laser-ablated devices and the powder-ablated devices.

The hydrogen alpha (H_α) line is commonly used to measure the electron density.[68-70] The broadening of this line depends on instrumental, Doppler, van der Waals, and Stark broadenings.[71] By measuring the full-width-at-half-maximum (FWHM) and subtracting all other broadenings, Stark broadening is directly proportional to electron density. Thus, Stark broadening can be obtained using the equation

$$\Delta\nu_{Stark} = FWHM - (\Delta\nu_{instrument} + \Delta\nu_{Doppler} + \Delta\nu_{van\ der\ Waals}), \quad (4.10)$$

where $\Delta\nu_{Stark}, \Delta\nu_{instrument}, \Delta\nu_{Doppler}, \Delta\nu_{van\ der\ Waals}$ are the Stark broadening, instrument broadening, Doppler broadening, and van der Waals broadening, respectively. All units are in nm. The instrument broadening is caused by the light divergence after the emission,[72] and the measured instrumental broadening was 0.02 nm. The Doppler broadening is caused by the distribution of molecular velocities,[73] so it is related to the gas temperature as well as the molecular mass. Doppler broadening can be calculated by

$$\Delta\nu_{Doppler} = (7.162 \cdot 10^{-7}) \cdot \lambda \cdot \sqrt{\frac{T_g}{M_A}}, \quad (4.11)$$

where λ, T_g, and M_A are wavelength (in nm), gas temperature (in K), and atomic mass (in g/mol), respectively. Thus, using λ, T_g, and M_A values of 656.28 nm, 400 K and 1 g/mol, respectively, the Doppler broadening is calculated to be 0.009 nm. The dipole interactions also cause the broadening, and it can be calculated by van der Waals broadening,[73,74]

$$\Delta\nu_{van\ der\ Waals} = (8.18 \cdot 10^{-26}) \cdot N \cdot \lambda^2 \cdot (a \cdot R^2)^{2/5} (\frac{T_g}{\mu})^{3/10}, \quad (4.12)$$

where N, λ, α, R^2, T_g, and μ are the atomic number density of hydrogen (in cm^{-3}), atomic wavelength (in nm), atomic polarizability of neutral perturber Ar (16.54×10^{-25} cm^3),[75] difference in the square radius of H_2 in the upper and lower levels (in Bohr radius a_0), gas temperature (in K), and the reduced mass, respectively. For R^2, the following calculation was used:

$$R^2 = R_i^2 - R_f^2, \tag{4.13}$$

$$\text{where } R_j^2 = \frac{n_j^2}{2}[5n_j^2 + 1 - 3l_j(l_j + 1)], \text{ j= i and f,} \tag{4.14}$$

where l_j is the electron orbital quantum number, and n is the principal quantum number (n = 2 and 3 were used for the Balmer series H-alpha). Plugging in the experimental parameters, calculated $\Delta\nu_{van\ der\ Waals}$ was 0.009 nm.

Subtracting all other broadening mechanisms (instrumental, Doppler, and van der Waals), Stark broadening could be obtained using eqn. (4.10). Figure 4.26 shows the experimentally obtained Balmer series H_α using Lorentzian fitting. As shown in the graph, the full-width-at-half-maximum was observed to be 0.34 nm and 0.33 nm for laser-ablated device and powder-ablated device, respectively. Using eqn. (4.10), the Stark broadening was obtained to be 0.30 nm and 0.29 nm for laser-ablated and powder-ablated, respectively. Using these values, electron density can be calculated by the tabulated fitting[76] that has been experimentally developed by other studies,

$$\log(n_e) = 20.7 + \frac{-8.9}{1+(\frac{\Delta\nu_S}{0.38})^{0.33}}. \tag{4.15}$$

Using this equation and Stark broadening measurements, the electron densities are calculated to be $1.2\times10^{16} \pm 0.8\times10^{15}$ cm^{-3} and $1.1\times10^{16} \pm 0.8\times10^{15}$ cm^{-3} for the laser-ablated and powder-ablated device, respectively. In short, the electron density increase of ~8% was observed when laser-

ablated device was used. It should again be noted that the etching method was the only variable; all other experimental parameters were identical.

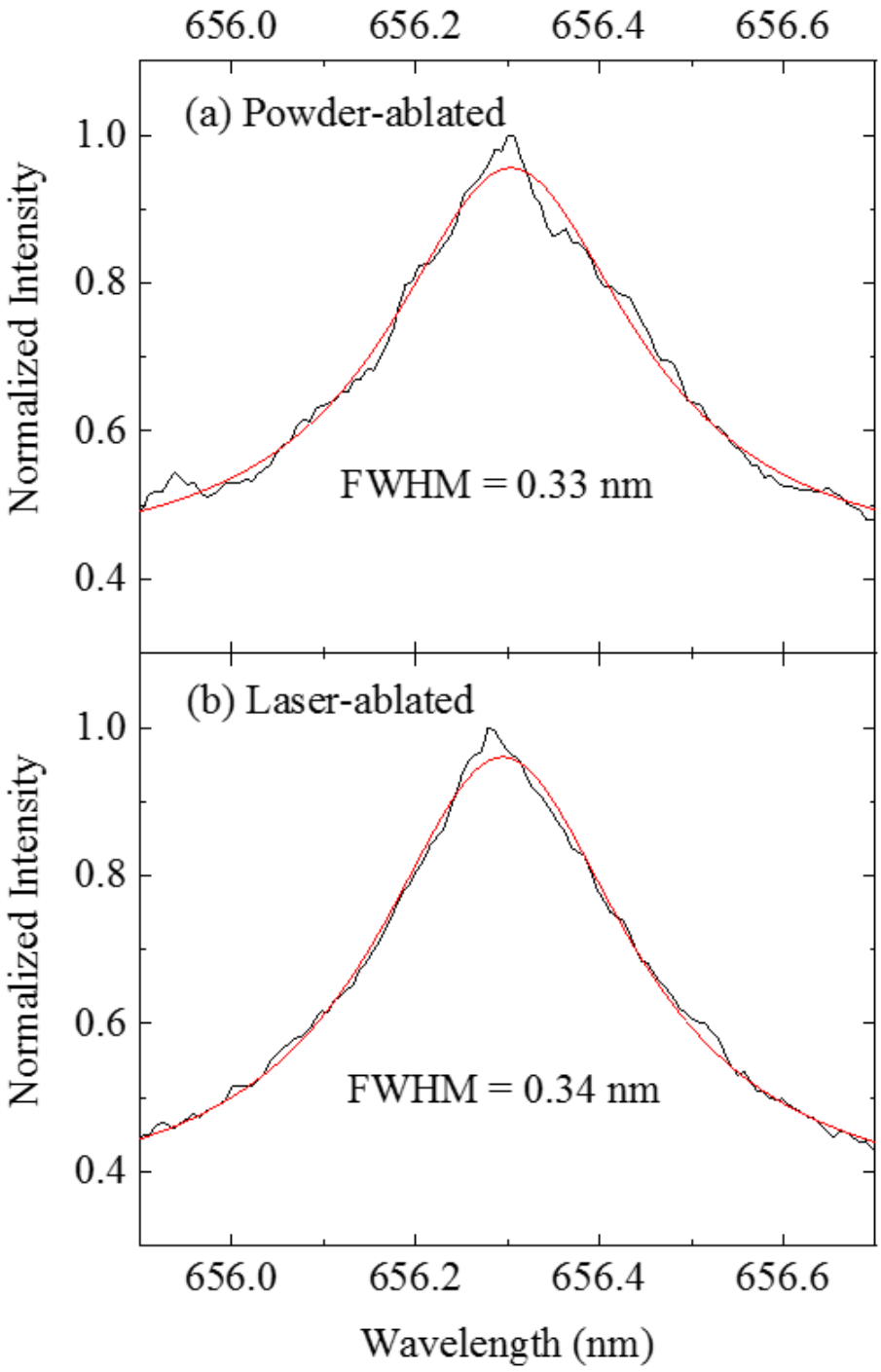

Figure 4.26 Experimentally obtained Balmer H_α line emission spectroscopy using 300 Torr (Ar/H_2, 1% H_2 by volume) for (a) powder-ablated and (b) laser-ablated device. 20 kHz 1.4 kV_{RMS} was applied for both cases. The Lorentzian fitting shows that more broadening occurs when laser-ablated device is used.

4.6 CO_2 DISSOCIATION RATE COEFFICIENT CALCULATION

Simple kinetic modelling using major reactions of CO_2 electron impact was carried out to observe how much dissociated CO_2 comes from the ionized CO_2 (i.e. CO_2^+) species. Table 4.1 shows the rate coefficient of individual reactions used in this modelling.

Table 4.1 Reactions and their rate coefficients used in this modelling. (R1)-(R6) show direct CO_2 dissociation using electron impact, and (R7) & (R8) show the dissociative recombination. (R9) shows the ionization rate coefficient, and the product of this reaction is the reactant of (R7) and (R8).

No.	Reaction	K, Rate Coefficient (cm^3/s)	Category	Reference
R1	$CO_2 + e^- \rightarrow CO + O^-$	$(5\times10^{-13})\times(T_g/300)^{1.5}\times(T_{e,(K)}/300)^{-1.5}$	Direct Electron Impact Dissociation	77
R2	$\rightarrow O_2^+ + C + e^- + e^-$	$(0.05)\times(1.4\times10^{-11})\times(T_{e,(K)})^{0.5}\times(1+1.3\times10^{-5}\times T_{e,(K)})\times\exp(-1.5\times10^5/T_{e.(K)})$		78,79
R3	$\rightarrow CO^+ + O + e^- + e^-$	$(0.1)\times(1.4\times10^{-11})\times(T_{e,(K)})^{0.5}\times(1+1.3\times10^{-5}\times T_{e,(K)})\times\exp(-1.5\times10^5/T_{e.(K)})$		
R4	$\rightarrow C^+ + O_2 + e^- + e^-$	$(0.1)\times(1.4\times10^{-11})\times(T_{e,(K)})^{0.5}\times(1+1.3\times10^{-5}\times T_{e,(K)})\times\exp(-1.5\times10^5/T_{e.(K)})$		
R5	$\rightarrow O^+ + CO + e^- + e^-$	$(0.1)\times(1.4\times10^{-11})\times(T_{e,(K)})^{0.5}\times(1+1.3\times10^{-5}\times T_{e,(K)})\times\exp(-1.5\times10^5/T_{e.(K)})$		
R6	$\rightarrow CO + O + e^-$	1.6×10^{-11}		80
R7	$CO_2^+ + e^- \rightarrow CO + O$	$(2\times10^{-5})\times(T_g)^{-1}\times(T_{e,(eV)})^{-0.5}$	Dissociative Recombination	81
R8	$\rightarrow C + O_2$	$(3.94\times10^{-7})\times(T_e)^{-0.4}$		82
R9	$CO_2 + e^- \rightarrow CO_2^+ + e^- + e^-$	$(0.65)\times(1.4\times10^{-11})\times(T_{e,(K)})^{0.5}\times(1+1.3\times10^{-5}\times T_{e,(K)})\times\exp(-1.5\times10^5/T_{e.(K)})$	Ionization	78,80

For this modelling, the reactions were divided into two groups: (1) CO_2 dissociation by direct electron impact and (2) CO_2 dissociation coming from the ionized CO_2. (R1)-(R6) are group

1, and (R7) & (R8) are group 2. Only electron impact reactions were employed in this study; any ion-neutral, ion-ion, and neutral-neutral reactions were neglected. Also, the calculation only considers the reactions that dissociate CO_2; any secondary reactions from the products of CO_2 for the further CO_2 dissociation were neglected. The population created by the ionization reaction (R9) is the reactant for the dissociative recombination. Thus, the overall rate coefficients of (R7) and (R8) are bottlenecked by the population of CO_2^+. However, once there are ionized CO_2, a majority of them are dissociated (this will be discussed in the following paragraph). Thus, for the rate coefficient of the dissociative recombination, it was assumed that all ionized CO_2 were dissociated by the dissociative recombination. The gas temperature of 400K was used for the calculation. Figure 4.27 shows the rate coefficient using the equations from table 4.1. The black line shows the sum of all the CO_2 dissociation by direct electron impact, and the red line shows the sum of the rate coefficient of CO_2 dissociation by dissociative recombination. The rate coefficient of the dissociative recombination (i.e. ionized CO_2 with e^-) becomes significant as soon as the electron energy exceeds ~2.5 eV. Of course, this can only be achieved when the microplasma system has (1) high enough electron energy and (2) sufficient population of ionized CO_2 created.

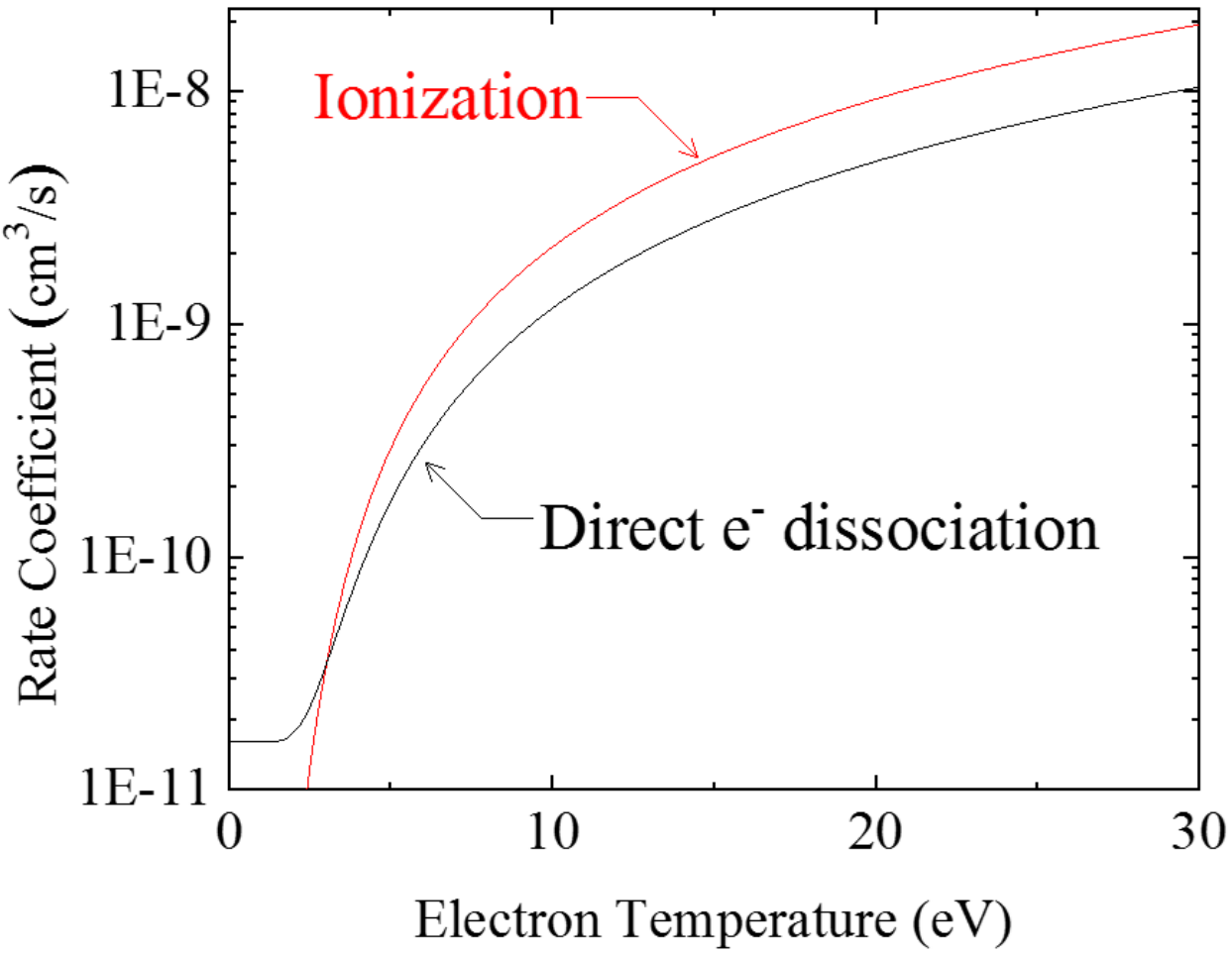

Figure 4.27 Total rate coefficients of CO_2 dissociation using various mechanisms. Ordinate is in log scale. Reactions used for the calculation are shown in table 4.1. Black and red lines represent the rate coefficient of direct electron impact (sum of (R1)-(R6)), and ionization (R9), respectively.

Rate coefficient is different from the rate constant, and further experiment should be conducted to observe the absolute amount of CO_2 dissociation coming from the direct electron impact and the dissociative recombination. With the current device, where the exact population of ionization is not known, it is not possible to get the exact rate constant of each reaction group. However, it is observed that, by calculating the rate coefficients, the dissociative recombination (hence ionization of CO_2) plays an important role as the electron energy increases. A device made with laser ablation had higher CO_2^+ relative intensity (thus higher population) with higher electron

density. Thus, combining with the calculation shown in this section, laser-ablated devices are more effective (in terms of CO_2 dissociation) especially when the average electron temperature is high enough for the ionization (and thus dissociative recombination) to be more significant. Aerts *et al.*[59] proved, through simulation at high reduced electric field regime (>100 Td), that the contribution of the electron impact dissociation for the CO_2 dissociation is only ~50%, and the other 50% comes from the electron impact ionization related processes. Observing significantly improved CO_2 dissociation and CO_2^+ emission intensity using the laser-ablated devices, this dissertation introduces an ablation technique that can achieve a device that can reach the electron energy and the reduced electric field described in the simulation.[75]

Furthermore, ionization related dissociation can be improved. Although my calculation assumed that all ionized CO_2 goes to dissociation, in reality, some ions participate in the reverse reaction of going back to CO_2 (22%p to be exact).[67] In other words, if these CO_2^+ can be used instead of going back to CO_2, ~20% increase of CO_2 dissociation can be achieved. Figure 4.22 (top figure) shows the decrease in mass 1 (H atom), which indicates that the ions were consumed during the plasma reaction. Also, higher dissociation rate of CO_2 (refer figure 4.25) by mixing H_2 shows that it utilized ionized CO_2. It should be noted, though, that CO_2^+ is not the only reaction that H_2 is involved with; for example, the products of H_2 can react with any of the radicals created by the (R1)-(R6). Due to the complexity of the reaction pathways when H_2 is added, individual reactions were not studied here. However, by the experiments reported in this dissertation, it can be concluded that mixing H_2 has a positive effect on (1) increasing the dissociation of CO_2 and (2) creation of value-added chemicals. Furthermore, my result matches with the CO_2 + H_2 simulation done by De Bie *et al.*[67]; adding H_2 into CO_2 plasma model increases the CO_2 dissociation.

In summary, this section calculates the rate coefficient of some major reactions of CO_2 dissociation using electron impact. Ionization seems to play a bigger role as electron energy increases. Chemical experiments and calculations observed in this section partially agree with the simulations done by other groups.[74,78]

4.7 ELECTRIC FIELD SIMULATION IN THE CAVITY SITES

Electric field inside the cavities has been simulated using Comsol software. Two-dimensional simulation was conducted. Various aspect ratios of cavities were used for the simulation. Figure 4.28 shows the illustration used for the simulation. Relative permittivities of 1, 10, and 1 for Al, Al_2O_3, and CO_2 were used, respectively. Extremely fine meshes were used for all cases, and figure 4.29 shows one of the meshes generated for the simulation. Triangular meshes were generated, and the number of elements generated ranged 18059-26201. Table 4.2 shows the cavity dimension and number of meshes generated.

Two-thousand (2,000) V was applied to the top aluminum, and the bottom aluminum was set to be ground. Figure 4.30 illustrates the electric potential in color scheme. White arrows in the figure indicate the electric field. Figure 4.31 shows electric field lines inside the cavities. As the radius of the cavity changes, the horizontal and vertical composition of electric field lines in the cavity changes. The horizontal electric field is responsible for electron oscillation inside the cavities, and that causes more intense activity (refer to figure 4.10 and 4.11) of electrons. Also, as the radius of the cavity decreases too much (say r = 1 μm), the majority of electric field inside the cavity is vertical. In fact, the electric field was as small as the electric field in Al_2O_3. In other words, when the cavity opening is too small, the cavity is not recognized. On the other hand, when

r = 30 µm, the openings are so wide that, even though there is a horizontal component of the electric field, electrons have higher probability of escaping out of the cavity. In short, the *pendulum effect* will not be effective when the cavity opening is either too small or too large. Thus, it is of interest to generate cavities with uniform cavity radius and depth.

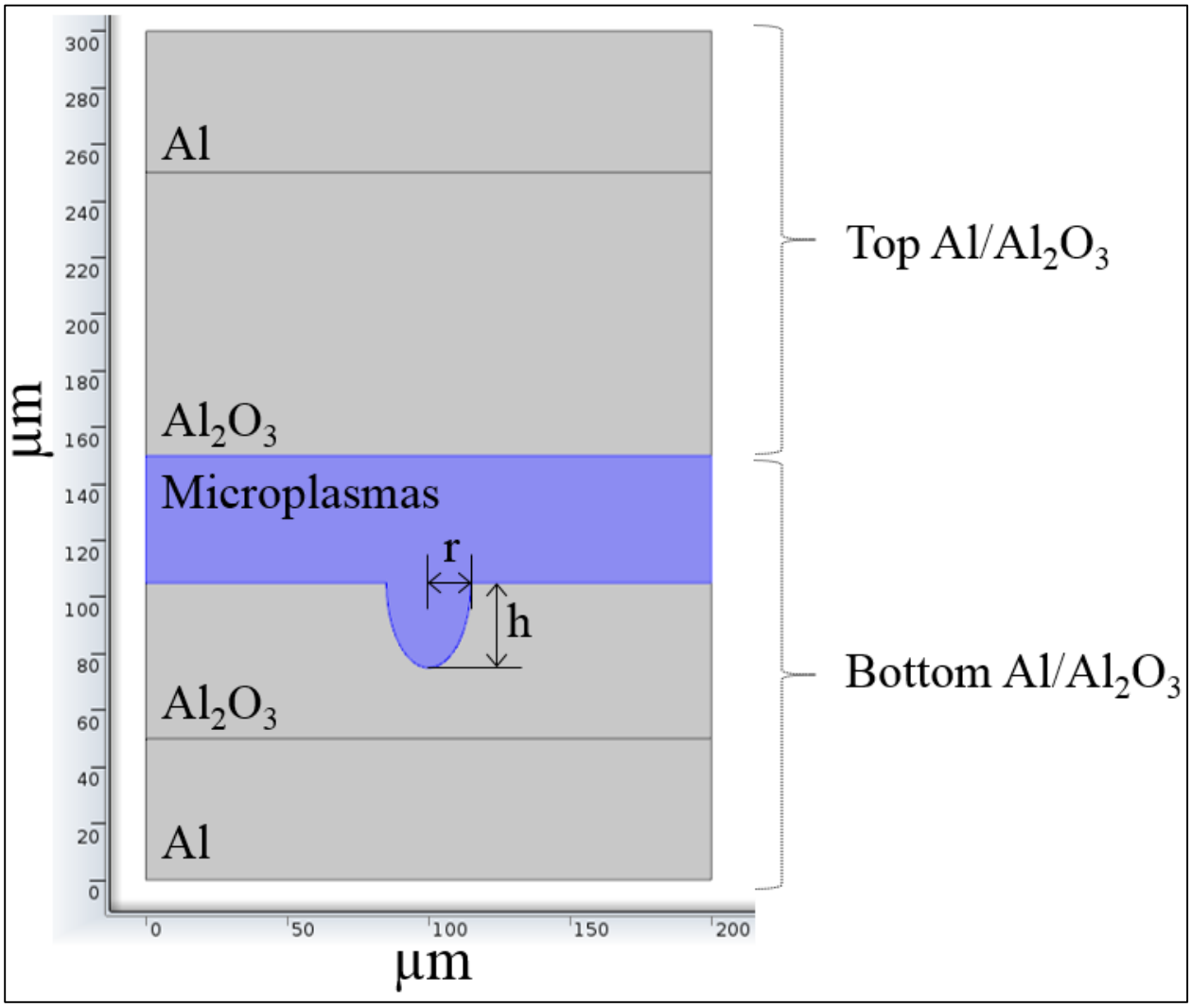

Figure 4.28 Spatial dimension illustration of systems used for the electric field simulation. Depicted as "Microplasmas", carbon dioxide was used with the relative permittivity of 1. The relative permittivities of 1 and 10 were used for Al and Al_2O_3, respectively. Cavity diameter was varied from 2 to 60 µm, with the set depth of 30 µm. Table 4.2 shows varied dimensions as well as number of elements created for the simulation for each case.

Table 4.2 Cavity dimensions and number of elements generated using extremely fine mesh setting. Cavity radius r (shown in fig. 4.28) was varied from 1 to 30 µm, whereas the depth (h) was set to be 30 µm.

r (µm)	h (µm)	Domain element	Boundary element	Total element
1	30	25470	731	26201
5	30	19850	664	20514
10	30	17980	637	18617
15	30	17526	627	18153
30	30	17440	619	18059

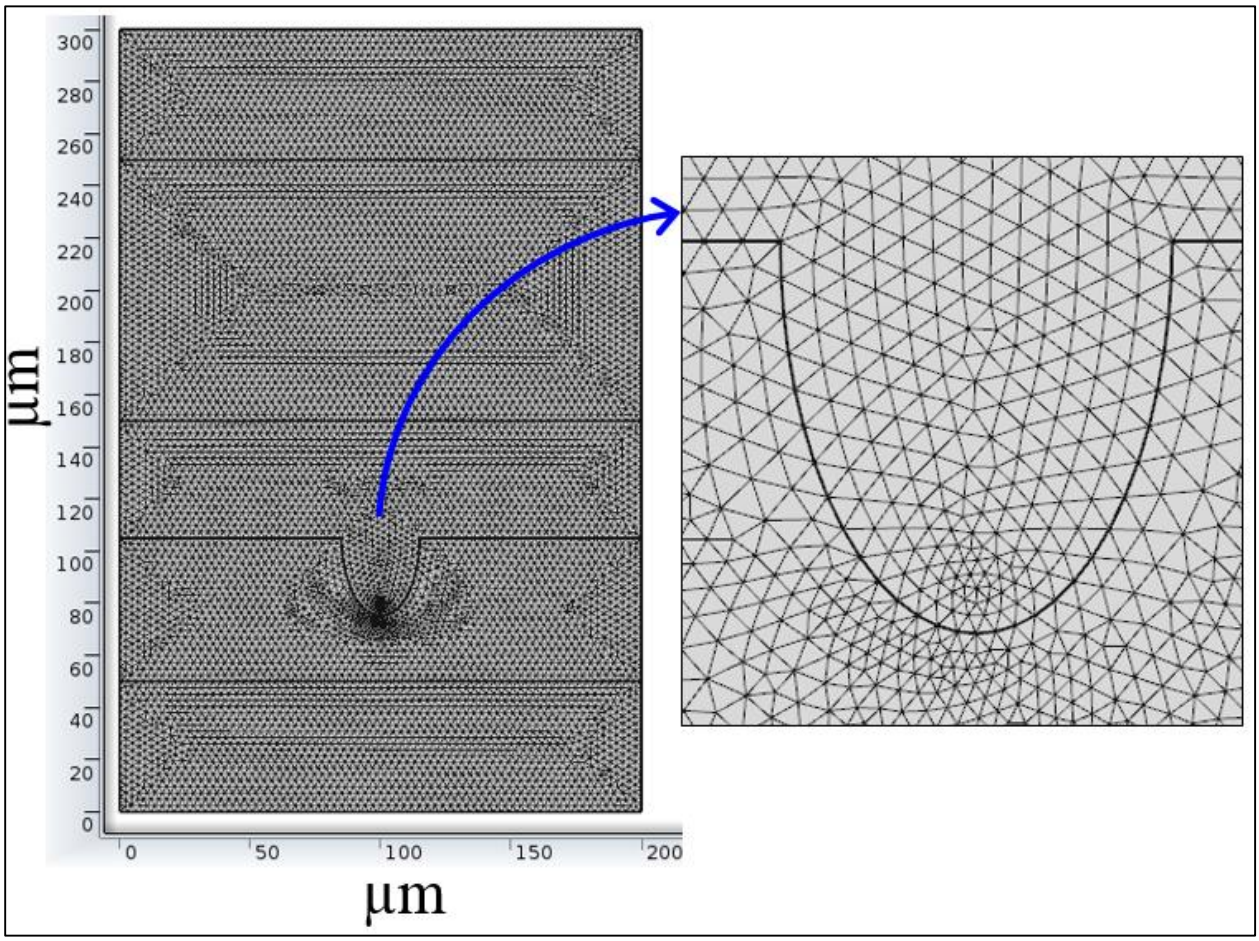

Figure 4.29 Illustration of generated meshes using extremely fine setting with triangular shape. The number of elements varied from 18,059 to 26,201 depending on cavity size. Table 4.2 shows exact number of elements generated for each case.

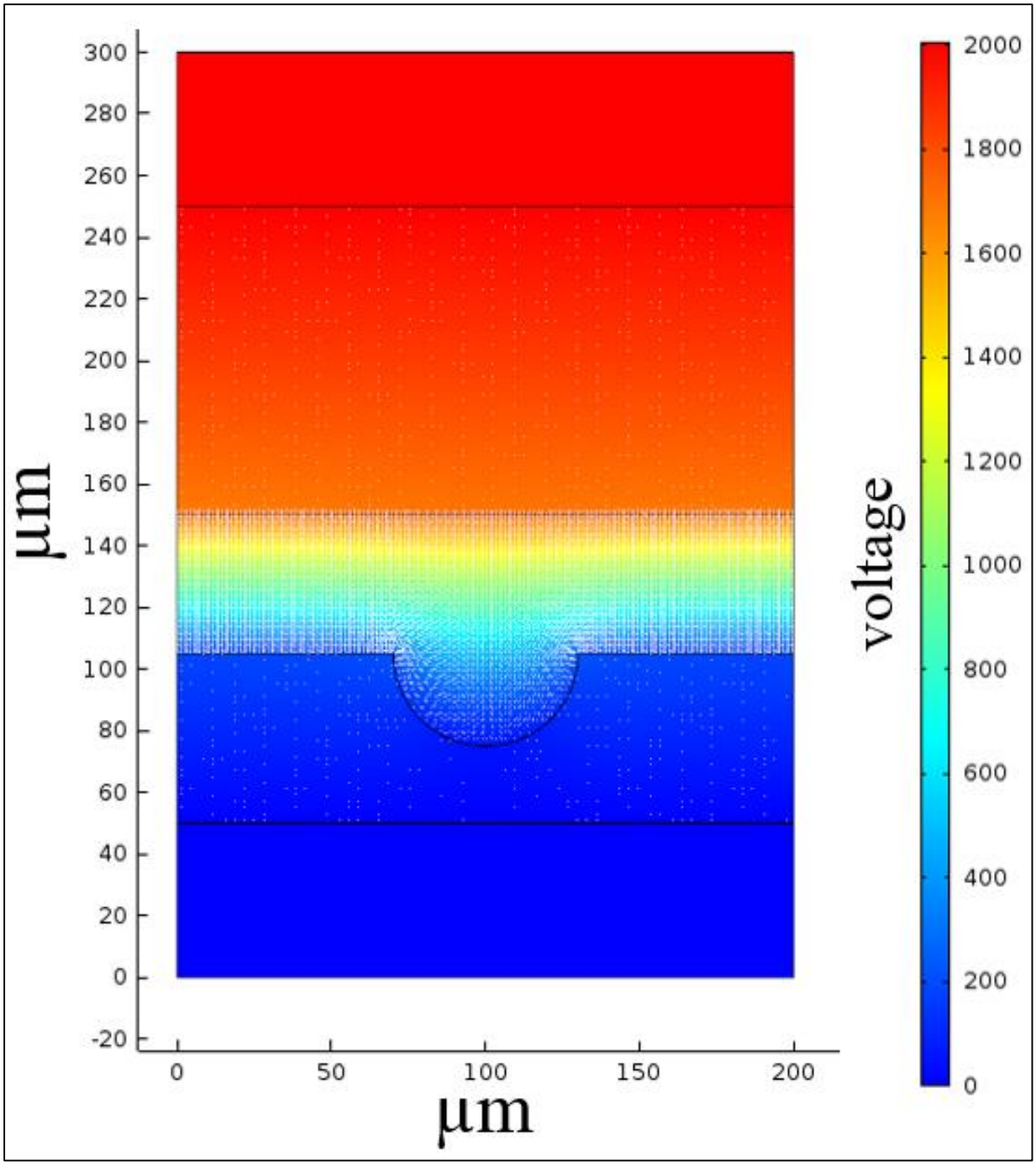

Figure 4.30 Electric potential simulation using r = 30 µm and h = 30 µm. Color bar on the right indicates the voltage.

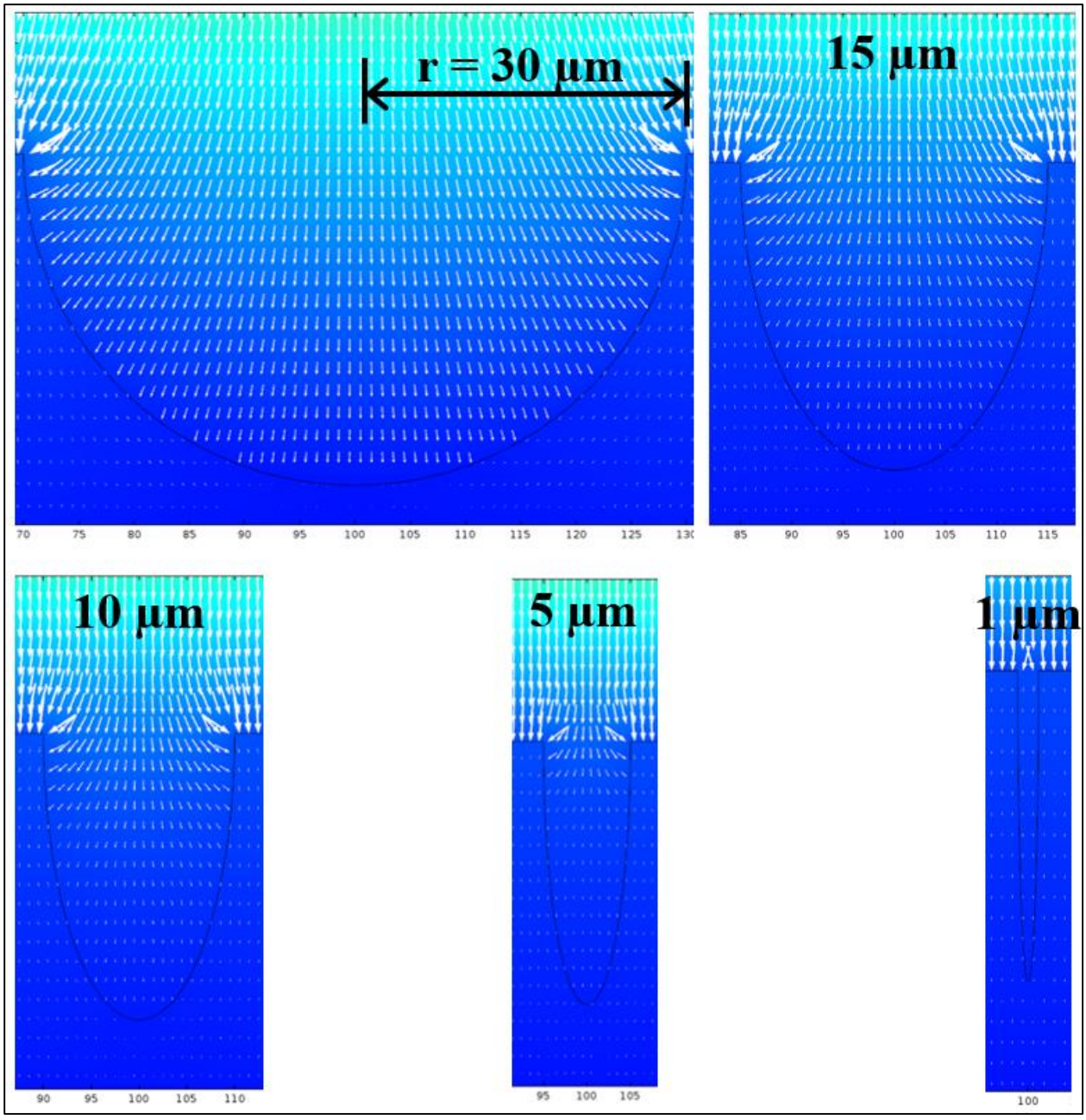

Figure 4.31 Electric field lines depending on the cavity radius. Cavity radius was varied from 1 to 30 µm, while the depth of the cavity was set to be 30 µm. When the cavity radius was the smallest (i.e. r = 1 µm), the electric field strength in the cavity was as small as those in the Al_2O_3. Also, the largest radius case (i.e. r = 30 µm) showed that, even though there was a horizontal component, most are vertical components that would not likely trap electrons in the cavity.

CHAPTER 5: CONCLUSIONS

In this dissertation, a newly developed laser ablation technique was introduced to fabricate microplasma devices. The device's ablated surface has cavities (craters) with random diameters ranging 5-150 μm. Electrical and optical characteristics of these cavities and hollow cavities within microchannels have been compared. Using higher surface-plasma interaction because of higher surface area, CO_2 dissociation energy efficiency has increased from ~13.5% to ~17.4% without change of any other parameters. Lower breakdown voltage (~6% decreased) has been observed for the laser-ablated chips compared to that of powder-ablated. Also, higher current has been observed, at any given voltage, for the laser-ablated chips compared to that of powder-ablated. This result agrees with the augmented field emission effect because of higher surface area.

Introducing 10% (by vol.) of H_2 into CO_2 further increased the energy efficiency to ~23.5%. Mixing 20% H_2 seemed to decrease the dissociation rate of CO_2, which indicates that there exists an optimal composition of CO_2/H_2 that maximizes the CO_2 dissociation. Overall, ~75% energy efficiency increase was achieved by using laser ablation with H_2 mixing. It should also be noted that, using the RGA, detectable amount of mass 30 (methane of formaldehyde) and 46 (ethanol or formic acid) has been observed. Furthermore, as H_2 composition increased, optical emission spectroscopy observation showed that CO/CO_2^+ (i.e. more CO generation) intensity increased, as well as the overall intensity. For the O_3 generation, ~7-11% increase of generation efficiency, compared to that of powder-ablated chips, has been achieved.

Regarding the fabrication process, it should be noted that the processing time has been significantly reduced using the newly introduced laser ablation technique. Another advantage of

laser ablation is that it does not consume any environmentally (and biologically) hazardous chemicals such as photoresist or micropowder. Furthermore, as it was shown in this dissertation that plasmachemical reaction can benefit from the surface roughness, it is of its distinct advantage that it can create rougher surfaces (±15 µm) that powder ablation cannot generate (±5 µm).

The reaction in the newly invented device benefitted from randomly generated cavities with random sizes that ranged ~0-100 µm diameter with ~300/mm^2 density (average diameter ~33 µm). However, discharge of uniform cavities with upside-down truncated cone shape, with bottom diameter of 150 µm and top diameter of 300 µm, could be achieved. It is possible that, rather than having cavities with random sizes, further optimization can be achieved by controlling the diameter of cavities because more surface area leads to higher plasma-surface interaction. Thus, further studies should include more in-depth observation and analysis of electron activities within the cavities that are dependent on the physical geometry of the cavities.

REFERENCES

[1] J. G. Eden, S.-j. Park, N. P. Ostrom, S. T. McCain, C. J. Wagner, B. A. Vojak, J. Chen, C. Liu, P. von Allmen, and F. Zenhausern, "Microplasma devices fabricated in silicon, ceramic, and metal/polymer structures: arrays, emitters and photodetectors," *Journal of Physics D: Applied Physics*, vol. 36, pp. 2869-2877, 2003.

[2] K. H. Schoenbach and K. Becker, "20 years of microplasma research: a status report," *The European Physical Journal D*, vol. 70, pp. 29, 2016.

[3] J. G. Eden, S.-j. Park, J. H. Cho, M. H. Kim, T. J. Houlahan, B. Li, E. S. Kim, T. L. Kim, S. K. Lee, K. S. Kim, J. K. Yoon, S. H. Sung, and P. Sun, "Plasma science and technology in the limit of the small: Microcavity plasmas and emerging applications," *IEEE Transactions on Plasma Science*, vol. 41, pp. 661, 2013.

[4] C. J. Wagner, S.-j. Park, and J. G. Eden, "Excitation of a microdischarge with a reverse-biased pn junction," *Applied Physics Letters*, vol. 78, pp. 709, 2001.

[5] S.-j. Park, K. S. Kim, and J. G. Eden, "Nanoporous alumina as a dielectric for microcavity plasma devices: Multilayer Al/Al_2O_3 structures," *Applied Physics Letters*, vol. 86, 221501, 2005.

[6] K. S. Kim, "Microstructural control of aluminum/aluminum oxide electrochemistry: aluminum/aluminum oxide photonic devices," PhD dissertation, University of Illinois at Urbana-Champaign, Urbana, IL, 2004.

[7] M. H. Kim, J. H. Cho, S. B. Ban, R. Y. Choi, E. J. Kwon, S.-j Park, and J. G. Eden, "Efficient generation of ozone in arrays of microchannel plasmas," *Journal of Physics D: Applied Physics*, vol. 46, pp. 305201, 2013.

[8] J. H. Lozano-Parada and W. B. Zimmerman, "The role of kinetics in the design of plasma microreactors," *Chemical Engineering Science*, vol. 65, pp. 4925, 2010.

[9] F. Rehman, J. H. Lozano-Parada, W. B. Zimmerman, "A kinetic model for H_2 production by plasmolysis of water vapours at atmospheric pressure in a dielectric barrier discharge microchannel reactor," *SciVerse Science Direct*, vol. 37, pp. 17678, 2012.

[10] K. H. Becker, K. H. Schoenbach, and J. G. Eden, "Microplasmas and applications," *Journal of Physics D: Applied Physics*, vol. 39, pp.55, 2006.

[11] A. Fridman, *Plasma Chemistry*, New York: Cambridge University Press, 2008.

[12] Y. Xu, "A general comparison between tokamak and stellarator plasmas," *Matter and Radiation at Extremes*, vol. 1, pp.192, 2016.

[13] S. Jodpimai, S. Boonduang, and P. Limsuwan, "Dielectric barrier discharge ozone generator using aluminum granules electrodes," *Journal of Electrostatics*, vol. 74, pp. 108, 2015.

[14] M. H. Kim, J. H. Cho, S. B. Ban, R. Y. Choi, E. J. Kwon, S.-j Park, and J. G. Eden, "Efficient generation of ozone in arrays of microchannel plasmas," *Journal of Physics D: Applied Physics*, vol. 46, pp. 305201, 2013.

[15] M. H. Kim, J. H. Cho, S.-J. Park, and J. G. Eden, "Modular and efficient ozone systems based on massively parallel chemical processing in microchannel plasma arrays: performance and commercialization," *European Physics Journal*, Special Topics, vol. 226, pp. 2923, 2017.

[16] K. Tachibana, "Design and control of microplasma devices based on spectroscopic diagnostics," in *2nd International Workshop on Microplasmas*, 2004.

[17] B. Abdullah, N. A. A. Ghani, D.-V. N. Vo, "Recent advances in dry reforming of methane over Ni-based catalysts," *Journal of Cleaner Production*, vol. 162, pp. 170-185, 2017.

[18] National Research Council and National Academy of Engineering of the National Academies, *The Hydrogen Economy: Opportunities, Costs, Barriers, and R&D Needs.* Washington, DC: The National Academies Press, 2004.

[19] D. Yarmolich, Ya. E. Krasik, E. Stambulchik, V. Bernshtam, J. K. Yoon, B. Herrera, S.-J. Park, and J. G. Eden, "Self-pulsing 104 A cm−2 current density discharges in dielectric barrier Al/Al2O3 microplasma devices," *Applied Physics Letters*, vol. 94, no. 1, 011501, 2009.

[20] E. Badareu and I. Popescu "Researches on the double cathode effect," *International Journal of Electronics*, vol. 4, no. 6, pp. 503-514, 1958.

[21] M. J. Kushner, "Modelling of microdischarge devices: Plasma and gas dynamics," *J. Phys. D, Appl. Phys.*, vol. 38, no. 11, pp. 1633–1643, 2005.

[22] J.-P. Boeuf, L. C. Pitchford, and K. H. Schoenbach, "Predicted properties of microhollow cathode discharges in xenon," *Appl. Phys. Lett.*, vol. 86, no. 7, 071501, 2005.

[23] H. J. Lee, S.-J. Park, and J. G. Eden, "Pulsed microplasmas generated in truncated paraboloidal microcavities: Simulations of particle densities and energy flow," *J. Phys. D, Appl. Phys.*, vol. 45, no. 40, 405201, 2012.

[24] K. H. Becker and K. H. Schoenbach, "High-pressure microdischarges," in *Low Temperature Plasmas*, vol. 2, R. Hippler, H. Kersten,M. Schmidt, and K. H. Schoenbach, Eds. Weinheim, Germany: Wiley-VCH, 2008.

[25] K. Tachibana, "Microplasma generation in artificial media and its potential applications," *Pure Appl. Chem.*, vol. 82, no. 6, pp. 1189–1199, 2010.

[26] C. Shin, "Dissociation of carbon dioxide in an Al/Al_2O_3 microplasma channel reactor at atmospheric pressure," M.S. thesis, University of Illinois at Urbana-Champaign, Urbana, IL, 2015.

[27] A. Ozkan, T. Dufour, G. Arnoult, P. De Keyzer, A. Bogaerts, and F. Reniers, "CO2-CH4 conversion and syngas formation at atmospheric pressure using a multi-electrode dielectric barrier discharge," *Journal of CO_2 Utilization*, vol. 9, pp. 74, 2015.

[28] J. G. Eden, S.-j Park, J. H. Cho, M. H. Kim, T. J. Houlahan, B. Li, E. S. Kim, T. L. Kim, S. K. Lee, K. S. Kim, J. K. Yoon, S. H. Sung, and P. Sun, "Plasma science and technology in the

limit of the small: Microcavity plasmas and emerging applications," *IEEE Transactions on Plasma Science*, vol. 41, pp. 661, 2013.

[29] G. E. Thompson, Y. Xu, P. Skeldon, K. Shimizu, S. H. Han, and G. C. Wood, "Anodic oxidation of aluminum," *Philosophical Magazine B*, vol. 55, no. 6, pp. 651, 1987.

[30] G. C. Wood, P. Skeldon, G. E. Thompson, and K. Shimizu, "A model for the incorporation of electrolyte species into anodic alumina," *Journal of Electrochemical Society*, vol. 143, no. 1, pp. 74, 1996.

[31] K. Shimizu, K. Kobayashi, G. E. Thompson, and G. C. Wood, "A novel marker for the determination of transport numbers during anodic barrier oxide growth on aluminum," *Philosophical Magazine B*, vol. 64, no. 3, pp. 345, 1991.

[32] G. Thompson and G. C. Wood, "Anodic films on aluminum," in *Treatise on Materials Science and Technology*, vol. 23. New York, NY: Academic Press, pp. 205, 1983.

[33] J. R. Dickey, J. L. Davidson, and Y. Tzeng, "Improved dielectric properties for anodic aluminum oxide films by soft/hard two-step electrolytic anodization," *Journal of Electrochemical Society*, vol. 136, no. 6, pp. 1772, 1989.

[34] S.-j. Park, K. S. Kim and J. G. Eden, "Nanoporous alumina as a dielectric for microcavity plasma devices: Multilayer Al/Al_2O_3 structures," *Applied Physics Letters*, vol. 86, pp. 221501, 2005.

[35] S. J. Davis, K. Caldeira, and H. D. Matthews, "Future CO_2 emissions and climate change from existing energy infrastructure," *Science*, vol. 329, pp. 1330, 2010.

[36] E. E. Benson, C. P. Kubiak, A. J. Sathrum, and J. M. Smieja, "Electrocatalytic and homogeneous approaches to conversion of CO_2 to liquid fuels," *Chemical Society Review*, vol. 38, pp. 89, 2009.

[37]D. T. Whipple and P. J. A. Kenis, "Prospects of CO_2 utilization via direct heterogeneous electrochemical reduction," *Journal of Physical Chemistry Letters*, vol. 1, pp. 3451, 2010.

[38] C. W. Li and M. W. Kanan, "CO_2 reduction at low overpotential on Cu electrodes resulting from the reduction of thick Cu_2O films," *Journal of American Chemical Society*, vol. 134, pp.7231, 2012.

[39] Y. Hori, A. Murata, K. Kikuchi, and S. Suzuki, "Electrochemical reduction of carbon dioxides to carbon monoxide at a gold electrode in aqueous potassium hydrogen carbonate," *Journal of Chemical Society, Chemical* Communications, vol. 10, pp. 728, 1987.

[40] N. Hoshi, T. Suzuki, and Y. Hori, "Step density dependence of CO2 reduction rate on Pt(S)-[n(111)x(111)] single crystal electrodes," *Electrochimica Acta, vol.* 41, pp. 1647, 1996.

[41] B. A. Rosen, A. Salehi-Khojin, M. R. Thorson, W. Zhu, D. T. Whipple, P. J. A. Kenis, and R. I. Masel, "Ionic liquid-mediated selective conversion of CO_2 to CO at low overpotentials," *Science*, vol. 334, pp. 643, 2011.

[42] A. Salehi-Khojin, H.-R. M Jhong, B. A. Rosen, W. Zhu, S. Ma, P. J. A. Kenis, and R. I. Masel, "Nanoparticle silver catalysts that show enhanced activity for carbon dioxide electrolysis," *Journal of Physical Chemistry C*, vol. 117, pp. 1627, 2013.

[43] E. E. Benson, C. P. Kubiak, A. J. Sathrum, and J. M. Smieja, "Electrocatalytic and homogeneous approaches to conversion of CO2 to liquid fuels," *Chemical Society Reviews*, vol. 38, pp. 89, 2009.

[44] G. Seshadri, C. Lin, and A. B. Bocarsly, "A new homogeneous electrocatalyst for the reduction of carbon dioxide to methanol at low overpotential," *Journal of Electroanalytical* Chemistry, vol. 372, pp. 145, 1994.

[45] E. B. Cole, P. S. Lakkaraju, D. M. Rampulla, A. J. Morris, E. Abelev, and A. B. Bocarsly, "Using a one-electron shuttle for the multielectron reduction of CO_2 to methanol: kinetic, mechanistic, and structural insights," *Journal of the American Chemical Society*, vol. 132, pp. 11539, 2010.

[46] S. N. Riduan, Y. Zhang and J. Y. Ying, "Conversion of carbon dioxide into methanol with silanes over N-heterocyclic carbene catalysts," *Angewandte Chemie International Edition*, vol. 48, pp. 3322, 2009.

[47] W. Wang, S. Wang, X. Ma, and J. Gong, "Recent advances in catalytic hydrogenation of carbon dioxide," *Chemical Society Reviews*, vol. 40, pp. 3703, 2011.

[48] B. Kumar, M. Asadi, D. Pisasale, S. Sinha-Ray, B. A. Rosen, R. Haasch, J. Abiade, A. L. Yarin, and A. Salehi-Khojin, "Renewable and metal-free carbon nanofiber catalysts for carbon dioxide reduction," *Nature Communications*, vol. 4, 2819, 2013.

[49] S. Paulussen, B. Verheyde, X. Tu, C. De Bie, T. Martens, D. Petrovic, A. Bogaerts, and B. Sels, "Conversion of carbon dioxide to value-added chemicals in atmospheric pressure dielectric barrier discharges," *Plasma Sources Science and Technology* ¸vol. 19, 034015, 2010.

[50] B. Eliasson, U. Kogelschatz, B. Xue, L.-M. Zhou, "Hydrogenation of carbon dioxide to methanol with a discharge-activated catalyst," *Industrial and Engineering Chemistry Research*, vol. 37, 8, pp. 3350, 1998.

[51] G. Zheng, J. Jiang, Y. Wu, R. Zhang, H. Hou, "The mutual conversion of CO_2 and CO in dielectric barrier dischatge (DBD)," *Plasma Chemistry and Plasma* Processing, vol. 34, 1, pp.59, 2003.

[52] Y. Li, G.-H. Xu, C.-J. Liu, B. Eliasson, B.-Z. Xue, "CO-generation of syngas and higher hydrocarbons from CO_2 and CH_4 using dielectric-barrier discharge: effect of electrode materials," *Energy and Fuels*, vol. 15, pp. 299, 2001.

[53] Y. Zhang, Y. Li, Y. Wang, C. Liu, B. Eliasson, "Plasma methane conversion in the presence of carbon dioxide using dielectric-barrier discharges," *Fuel Processing Technology*, vol. 83, pp. 101, 2003.

[54] J.-Y. Wang, G.-G. Xia, A. Huang, S.L. Suib, Y. Hayashi, H. Matsumoto, "CO_2 decomposition using glow discharge plasmas," *Journal of catalysis*, vol. 185, pp. 152, 1999.

[55] H.K. Song, H. Lee, J.-W. Choi, B.-K. Na, "Effect of electrical pulse forms on the CO_2 reforming of methane using atmospheric dielectric barrier discharge," *Plasma Chemistry and Plasma Processing*, vol. 24, 2004.

[56] A.-J. Zhang, A.-M. Zhu, J. Guo, Y. Xu, C. Shi, "Conversion of greenhouse gases into syngas via combined effects of discharge activation and catalysis," *Chemical Engineering Journal*, vol. 156, 3, pp. 601, 2010.

[57] Y. Wen and X. Jiang, "Decomposition of CO_2 using pulsed corona discharges combined with catalyst," *Plasma Chemistry and Plasma Processing*, vol. 21, 4, pp. 665, 2001.

[58] A. Indarto, D.R. Yang, J.W. Choi, H. Lee, and H.K. Song, "Gliding arc plasma processing of CO_2 conversion," *Journal of Hazardous Materials*, vol. 146, pp. 309, 2007.

[59] R. Aerts, T. Martens, and A. Bogaerts, "Influence of vibrational states on CO_2 splitting by dielectric barrier discharges," *Journal of Physical Chemistry C*, vol. 116, pp. 23257, 2012.

[60] A. Fridman, *Plasma Chemistry*, New York: Cambridge University Press, 2008.

[61] M. T. O. de Velásquez, M. N. Rojas-Valencia, and A. Ayala, "Wastewater disinfection using ozone to remove free-living, highly pathogenic bacteria and amoebae," *Ozone: Science and Engineering*, vol. 30, no. 5, pp. 367, 2008.

[62] U. Kogelschatz, B. Eliasson, and M. Hirth, "Ozone generation from oxygen and air: Discharge physics and reaction mechanisms," *Ozone: Sci. Eng.*, vol. 10, no. 4, pp. 367–378, 1988.

[63] C. De Bie, J. van Dijk, and A. Bogaerts, "CO_2 hydrogenation in a dielectric barrier discharge plasma revealed," *The Journal of Physical Chemistry C*, vol. 120, pp. 25210, 2016.

[64] S. H. Sung, I. C. Hwang, S.-j. Park, and J. G. Eden, "Interchannel optical coupling within arrays of linear microplasmas generated in 25-200 μm wide glass channels," *Applied Physics Letters*, vol. 97, 231502, 2010.

[65] C. Shin, T. Oh, T. Houlahan, C-H Fann, S.-j. Park, and J. G. Eden, "Dissociation of carbon dioxide in arrays of microchannel plasmas," *Journal of Physics D: Applied Physics*, 2018, (accepted).

[66] A. Fowler and A. G. Gaydon, "Spectrum of the afterglow of carbon dioxide," *Proceedings of the Royal Society of London. Series A*, vol. 142, no. 847, pp.362, 1933.

[67] C. De Bie, J. van Dijk, and A. Bogaerts, "CO_2 hydrogenation in a dielectric barrier discharge plasma revealed," *The Journal of Physical Chemistry C*, vol. 120, pp. 25210, 2016.

[68] C. Parigger, D. H. Plemmons, and J. W. L. Lewis, "Spatially and temporally resolved electron number density measurements in a decaying laser-induced plasma using hydrogen-alpha line profiles," *Applied Optics*, vol. 34, 18, pp. 3325, 1995.

[69] C. Yubero, M. C. Garcia, and M. D. Calzada, "On the use of the H_a spectral line to determine the electron density in a microwave (2.45 GHz) plasma torch at atmospheric pressure," *Spectrochimica Acta Part B*, vol. 61, pp. 540, 2006.

[70] W. Heidbrink, K. Burrell, Y. Luo, N. Pablant, and E. Ruskov, "Hydrogen fast-ion diagnostic using Balmer-alpha light," *Plasma physics and controlled fusion*, vol. 46, pp. 1855, 2004.

[71] H. R. Grien, A. C. Kolb, and K. Shen, "Stark broadening of hydrogen lines in a plasma," *Physical Review*, vol. 116, pp. 4, 1959.

[72] W. L. Wiese, D. E. Kelleher, and D. R. Paquette, "Detailed study of the Stark broadening of Blamer lines in a high-density plasma," *Physical Review A*, vol. 6, 3, pp. 1132, 1972.

[73] S. Djurovic and N. Konjevic, "On the use of non-hydrogenic spectral lines for low electron density and high pressure plasma diagnostics," *Plasma Sources Science and Technology*, vol. 18, 035011, 2009.

[74] C. S. Lee, D. M. Camm, and G. H. Copley, "Van der Waals broadening of argon absorption lines," *Journal of Quantitative Spectroscopy and Radiative Transfer*, vol. 15, pp.211, 1975.

[75] J. Munoz, M. S. Dimitrijevic, C. Yubero, and M. D. Calzada, "Using the van der Waals broadening of spectral atomic lines to measure the gas temperature of an argon-helium microwave plasma at atmospheric pressure," *Spectrochimica Acta Part B*, vol. 64, pp. 167, 2009.

[76] M. A. Gigosos and V. Cardenoso, "New plasma diagnosis tables of hydrogen Stark broadening including ion dynamics," *Journal of Physics B: Atomic, Molecular and Optical Physics*, vol. 29, pp. 4795, 1996.

[77] A. I. Maksimov, L. S. Polak, A. F. Sergienko, and D. I. Slovetskii, "Mechanism of the formation and decomposition of CO2 molecules in a glow-discharge in carbon-monoxide," *High Energy Chemistry* ,vol. 13, pp. 311, 1979.

[78] L. J. Kieffer, "Low-energy electron-collision cross-section data: part I: ionization, dissociation, vibrational excitation," *Atomic Data and Nuclear Data Tables*, vol.1, pp. 19, 1989.

[79] W. M. Jackson, R. T. Brackmenn, and W. L. Fite, "Temperature dependence of the dissociative ionization of CO_2," *International Journal of Mass Spectrometry and Ion Physics*, vol. 13, 3, pp. 237, 1974.

[80] S. Ono and S. Teii, "Negative ion formations and their effects on the electron temperature in CO2-N2-He mixture gas discharges," *Journal of Physics D: Applied Physics*, vol. 17, pp.1999, 1984.

[81] H. Hokazono and H. Fujimoto, "Theoretical analysis of the CO2 molecule decomposition and contaminants yield in transversely excited atmospheric CO2 laser discharge," *Journal of Applied Physics*, vol. 62, pp. 1585, 1998.

[82] T. G. Beuthe and J.-S. Chang, “Chemical kinetic modelling of non-equilibrium Ar-CO2 thermal plasmas,” *Japanese Journal of Applied Physics*, vol. 36, pp. 4997, 1997.

APPENDIX: LASER ENERGY INPUT CALCULATION

Following is the calculation of how much energy was put into individual molecules. For the calculation, nanoporous alumina, which is exhaustively discussed in this dissertation, is used as an example. Ablated dimensions were 75 μm, 500 μm, and 4 cm for the depth, width, and length, respectively. Alumina density and the molar mass of 3.95 g/cm^3 and 101.96 g/mol were used, respectively, for the calculation.

Total ablated volume:

$$75\ \mu m\ \times 500\ \mu m \times 4\ cm = 1.5\ \times\ 10^{-3}\ cm^3$$

Total mass ablated:

$$1.5 \times 10^{-3}\ cm^3\ \times 3.95\ \frac{g}{cm^3} = 5.9\ \text{mg}$$

Number of mol ablated:

$$5.9\ mg\ \times\ \frac{1}{101.96}\frac{mol}{g} = 5.8 \times 10^{-5}\ mol$$

Number of molecules:

$$5.8 \times 10^{-5}\ mol\ \times 6.02 \times 10^{23}\ \frac{molecules}{mol}$$

$$= 3.5 \times 10^{19}\ molecules \qquad \text{(A.1)}$$

Thus, a total of 3.5 × 10^{19} molecules was ablated. For the total energy input,

Total energy input:

$$26\ \frac{J}{cm^2}\ \times 0.05\ cm\ \times 4\ cm = 5.2\ J$$

Energy in eV:

$$5.2\ J\ \times 6.24 \times 10^{18}\ \frac{eV}{J}$$

$$= 3.2 \times 10^{19}\ eV \qquad \text{(A.2)}$$

Using eqns. (A.1) and (A.2), average energy input per molecule is calculated to be 0.91 eV/mole.

As the photon energy of the infrared laser engraver used in this study is ~0.12 eV/photon (CO_2 laser, 10.6 μm wavelength), it is concluded that individual molecules are absorbing the average energy of ~8 photons.

The same calculation was done for the quartz, with the material density and the molar mass of 2.648 g/cm^3 and 60 g/mol, respectively. One of the points in the linear ablation depth slope (30 J/cm^2 at 75 μm) was used for the calculation. The result for this calculation was similar to that of alumina: ~0.94 eV/mole, which is ~8 photons/molecule.